SPECKLE MECHANISM IN HOLOGRAPHIC OPTICAL COHERENCE IMAGING

A Dissertation
Presented to
The Faculty of the Graduate School
University of Missouri

In Partial Fulfillment
of the Requirements for the Degree
of Doctor of Philosophy

By

HAIBO LIN

Dr. Ping Yu, Dissertation Supervisor

May 2009

The undersigned, appointed by the Dean of the Graduate School, have examined the dissertation entitled:

SPECKLE MECHANISM IN HOLOGRAPHIC OPTICAL COHERENCE IMAGING

presented by Haibo Lin

a candidate for the degree of Doctor of Philosophy

and hereby certify that in their opinion, it is worthy of acceptance.

_____

Dr. Ping Yu

_____

Dr. Liqun (Andrew) Gu

_____

Dr. Meera Chandrasekhar

_____

Dr. Suchismita Guha

_____

Dr. H. R. Chandrasekhar

To my parents:

Aimei He and Zhimin Lin

and my wife:

Huifang Zhai

ACKNOWLEDGEMENTS

I have been fortunate to work with professors who have been encouraging and supportive of my endeavors during my Ph.D. study. I would like to specially thank my thesis advisor, Prof. Ping Yu who has been invaluable in his constant support, continuous motivation and inspiration, and in allowing me to work in an environment with the freedom to explore different avenues of research. In giving me the opportunity to attend conferences, he has contributed immeasurably to my personal and professional growth.

I would like to thank Prof. Lixin Ma and Dr. Sunder Balasubramanian for their help and support since the beginning of my research. Thanks to Prof. David Nolte, Dr. Kwan Jeong and Yihong Liu from Purdue University for generously providing the quantum well device and training for device fabrication. I would like to thank Dr. Leilei Peng from Harvard Medical School for providing helpful discussion and thank Matthew D. Mower for his patient help with language correction of my thesis.

Thanks to my committee (Prof. Yu, Prof. H. R Chandrasekhar, Prof. Meera Chandrasekhar, Prof. Guha, and Prof. Gu) for their patience and insightful questions, the faculties (Prof. Shijie Chen, Prof. Xiaoqin Zou, Prof. Aigeng Li, Prof. Henry White and Prof. Yun Zhang) and staffs of the physics departments (Sherry Long, Lora Baker, Gay Sturguess, Hill, Sarah and Sam Potts) for their continuous support. Thanks to my friends (Xiaohui Wang, Haoyang Liu, Li Ma, Shuo Yang and others), colleagues (Linghui Li, Mike Wood, Kujala Naresh and others) and former group members (Dr. Gang Yu, Dr. Xiaoxuan Xu and Prof. Cunzhou Zhang) for their support and help.

Special thanks to my parents, Zhiming Lin and Aimei He, my brother, Haijun Lin and my wife, Huifang Zhai for their support, encouragement and love. I am deeply in debt.

TABLE OF CONTENTS

LIST OF TABLES

LIST OF FIGURES

FIGURE **PAGE**

LIST OF ABBREVIATIONS

OCI	Optical Coherence Imaging
OCT	Optical Coherence Tomography
PRQW	Photorefractive Quantum Device
LD	Laser Diode (single wavelength light source)
SLD	Superluminescent Diode (broadband light source)
TWM	Two-wave Mixing
FWM	Four-wave Mixing
CCD	Charge Coupled Device
ND Filter	Neutral Density Filter
NA	Numerical Aperture
BS	Beam Splitter
FWHM	Full Width at the Half Maxima
3D	Three Dimensional
2D	Two Dimensional
PDF	Probability Density Function
CW	Continuous Wave
SF	Spatial Filter
MFP	Mean Free Path

ABSTRACT

This thesis provides the first studies on speckle statistics in holographic optical coherence imaging (OCI). The new speckle statistics consider the combination of holographic speckle and photorefractive effects, and is used to optimize the holographic diffraction efficiency and coherent image contrast for biomedical imaging applications.

Speckle mechanisms are understood systematically in a holographic imaging system that consists of low coherence interferometry, dynamic holography and photorefractivity. The holograms are recorded and reconstructed in a photorefractive multiple quantum well device by using non-degenerate four-wave mixing. The newly developed theory provides a comprehensive description of holographic speckle under small and large signal limits. For both conditions, a unit intensity ratio between the writing beam and probe beam is found to be an optimal value for the diffraction efficiency. In the four-wave mixing configuration, the fringe spacing plays an important role in generating holograms. When the speckle exists, the diffraction efficiency highly depends on the comparison between the fringe spacing and speckle size. Speckle contribution to the holographic images can be decreased by employing a fringe spacing larger than the speckle size. However, this will reduce spatial resolution in the imaging system. With a moving grating technique, speckle noises in holographic OCI are successfully suppressed based on a speckle averaging in the CCD camera.

As a practical example, holographic speckle images through turbid media (milk suspensions and polystyrene bead suspensions) are acquired and analyzed. Speckle generated by the turbid medium degrades the lateral and depth resolutions of the hologram due to distortion of the coherence wavefront. The resolution degradation depends on the mean free path (concentration) of the suspensions. Several methods that are proposed in the theoretical analysis are applied to the holographic OCI. The image quality of the test chart is improved. With the combination of signal optimization and noise suppression, holographic OCI becomes a powerful technique for biomedical tissue imaging. Furthermore, holographic optical imaging using two-wave mixing is explored with acceptable image quality due to higher diffraction efficiency than that of conventional four-wave mixing in the photorefractive materials.

Chapter 1

Introduction and Background

1.1 Motivation and research objectives

Biological application of optical imaging technology has a long and distinguished history. The appearance of optical microscope has a huge impact and serves as an indispensable tool to the cellular imaging for biologists. The invention of laser in the early 1960's provided highly bright and coherence light sources for biological imaging applications, such as confocal microscopy, two photon microscopy, and laser spectroscopic imaging, etc. In recent years, several new optical imaging techniques have been developed to provide diagnosis at tissue level. Although lasers have many applications in biomedicine, however, few lasers are used in hospitals today for three dimensional (3D) biological tissue imaging since the coherent light is highly scattered in tissues. When a laser passes through tissue, a phenomenon called laser speckle can be observed due to the coherence of the laser. Speckle reduces the image quality in optical imaging systems.

The mechanism of speckle is due to heterogeneity of cell structures. Interferences between scattered wavefronts generate random speckle patterns. On the other hand, speckle also carries structural information in addition to the contribution of random noise.

Therefore, speckle can be classified into two types: signal-carrying speckle and signal-degrading speckle. The purpose of speckle reduction is to reduce the noise speckle patterns and maintain the signal-carrying information. Speckle is a serious problem especially for those imaging techniques that use spatial and temporal coherence of optical waves, such as coherence domain imaging.

Several coherence domain imaging techniques have been developed for tissue imaging. Based on the low coherence interferometry, the short coherence of a broadband light source can be used to achieve depth-resolved images in biological samples. The axial information (called A scan, like ultrasound imaging) is provided through a rapid-scan delay line, and the interferograms are obtained using heterodyne method to differentiate the coherent component from the scattered background. The lateral information is acquired by using a point-by-point scanning of the detection head. The coherence domain imaging has several modalities based on acquisition formats [1-7]. Among them, optical coherence tomography (OCT) is one of successful techniques.

Just like white light has almost no speckle, an OCT system using low coherence light partly solves the speckle problem. Still coherence domain imaging suffers the degradation of image quality due to speckle when using a low coherence light source with wavelength bandwidth of 10 nm – 100 nm. Several methods have been proposed to overcome the speckle problem in OCT, such as hardware improvements [8-11] or different algorithms in the image reconstruction [12, 13]. However, these methods are

either complicated or expensive. One conventional method to solve the speckle problem is to vibrate the light wave giving an average of images. To apply this method in the coherence domain imaging, a fast imaging acquisition rate is required. However, due to the scanning nature, it is very difficult to achieve high speed imaging in OCT. Holographic optical coherence imaging (OCI) has been demonstrated with a high speed imaging capability. Therefore it can be used to solve the speckle problem using the average method.

Similar to the OCT system, which prominently uses the coherent nature of light source to achieve 3D imaging, holographic OCI using photorefractive quantum wells devices (PRQW) to record dynamic holograms. This technique presents advantages in potential applications of tissue imaging, such as fast image rates [14, 15] and high resolution [16, 17]. Holographic OCI initially employed a bulk photorefractive crystal to generate volume holograms [18]. The drawbacks of using the bulk crystal, such as low response time and refresh rates, limit biological applications of this technique. PRQW device solves most of these problems with its enhanced optical properties based on quantum localization of electrons in very thin layers [19]. These properties make this semiconductor device a promising candidate for holographic and adaptive applications [20-23]. Holographic OCI based on PRQW was first used to capture video-rate images [14, 15] with a speed up to 1000 frames/sec [24, 25]. The fast acquisition rate can be used to manipulate speckle. For example, a vibration mirror has been used in the system for

imaging tumor tissue [26].

The holographic OCI system takes the advantages of low coherence interferometry to generate 3D images. At the same time, it also suffers the speckle problem which is inherent character in the coherent imaging. The speckle in the holographic OCI is due to the multiple scattering from the small particles. The speckle is presented as an insidious form of noise that degrades the quality of the OCI images. On the other hand, if the speckle is entirely removed, image feathers can not be remained. Thus, speckle is also an important and critical component for holographic OCI. However, detailed studies of speckle properties in the holographic OCI have not been performed. Some of important questions should be answered for understanding the speckle mechanisms, for example, the speckle statistics and the system resolution changes due to the speckle.

This thesis gives the first and comprehensive studies on the speckle statistics and properties in holographic OCI. Speckle contribution to the image noise is partly controlled by choosing larger fringe spacing. However, the fringe spacing has to be as small as possible to ensure the observation of detailed structures of the subject. A moving grating technique is studied in detail. Experiments show that the technique can successfully suppress random speckle and improve the image quality and contrast [27].

1.2 Outline of the dissertation

In this dissertation, we investigate the speckle mechanisms in holographic optical coherence imaging. In Chapter 2, nonlinear optical properties of the photorefractive quantum well device are discussed. The detailed information of the nonlinear processes of the quantum well device especially two-wave mixing and four-wave mixing are presented. The new idea of using a two-wave mixing signal to achieve imaging goals is proposed and preliminary data is shown to prove the concept.

In Chapter 3, statistic evaluation of the average speckle size is executed based on the digitized speckle imaging. Speckles with different sizes are generated by changing the roughness of the object and incident beam size. The influence of the speckle size on the diffracted four-wave mixing signal is studied.

In Chapter 4, the theoretic statistical model of holographic speckle is developed based on the statistics of well developed speckle. Experiments are executed to prove this new theoretical model. Probability density functions for the small signal limit, large signal limit and Joule heating limit are studied.

In chapter 5, holographic speckle imaging is studied. The degradation on system resolution by unwanted speckle is investigated. Also, an effective speckle reduction technique, the moving grating technique, is introduced. Simulation study is applied to understand the speckle reduction principle.

In the appendix, all Matlab programs used for this project are presented.

BIBLIOGRAPHY

1. D. Huang, E. A. Swanson, C. P. Lin, J. S. Schuman, W. G. Stinson, W. Chang, M. R. Hee, T. Flotte, K. Gregory, C. A. Puliafito, and J. G. Fujimoto, "Optical Coherence Tomography," Science **254**, 1178-1181 (1991).

2. J. G. Fujimoto, M. E. Brezinski, G. J. Tearney, S. A. Boppart, B. Bouma, M. R. Hee, J. F. Southern, and E. A. Swanson, "Optical Biopsy and Imaging Using Optical Coherence Tomography," Nature Medicine **1**, 970-972 (1995).

3. J. A. Izatt, M. D. Kulkarni, H. W. Wang, K. Kobayashi, and M. V. Sivak, "Optical coherence tomography and microscopy in gastrointestinal tissues," Ieee Journal of Selected Topics in Quantum Electronics **2**, 1017-1028 (1996).

4. J. A. Izatt, M. D. Kulkarni, K. Kobayashi, M. V. Sivak, J. K. Barton, and A. J. Welch, "optical coherence tomography for biodiagnostics," Opt. Photon. News **8**, 41-47 (1997).

5. J. M. Schmitt, and S. H. Xiang, "Cross-polarized backscatter in optical coherence tomography of biological tissue," Optics Letters **23**, 1060-1062 (1998).

6. A. G. Podoleanu, J. A. Rogers, and D. A. Jackson, "OCT en-face images from the retina with adjustable depth resolution in real time," Ieee Journal of Selected Topics in Quantum Electronics **5**, 1176-1184 (1999).

7. W. Drexler, U. Morgner, R. K. Ghanta, F. X. Kartner, J. S. Schuman, and J. G. Fujimoto, "Ultrahigh-resolution ophthalmic optical coherence tomography," Nature Medicine **7**, 502-507 (2001).

8. A. E. Desjardins, B. J. Vakoc, G. J. Tearney, and B. E. Bouma, "Speckle reduction in OCT using massively-parallel detection and frequency-domain ranging," Optics Express **14**, 4736-4745 (2006).

9. J. Kim, D. T. iller, E. Kim, S. Oh, J. Oh, and T. E. Milner, "Optical coherence tomography speckle reduction by a partially spatially coherent source," Journal of Biomedical Optics **10** (2005).

10. Desjardins, Vakoc A. E., Oh B. J., Motaghiannezam W. Y., Tearney S. M. R., and B. E. Bouma, "Angle-resolved Optical Coherence Tomography with sequential angular selectivity for speckle reduction," Optics Express **15**, 6200-6209 (2007).

11. D. L. Marks, T. S. Ralston, and S. A. Boppart, "Speckle reduction by I-divergence regularization in optical coherence tomography," Journal of the Optical Society of America a-Optics Image Science and Vision **22**, 2366-2371 (2005).

12. A. Ozcan, A. Bilenca, A. E. Desjardins, B. E. Bouma, and G. J. Tearney, "Speckle reduction in optical coherence tomography images using digital filtering," Journal of the Optical Society of America a-Optics Image Science and Vision **24**, 1901-1910 (2007).

13. N. Iftimia, B. E. Bouma, and G. J. Tearney, "Speckle reduction in optical coherence tomography by "path length encoded" angular compounding," Journal of Biomedical Optics **8**, 260-263 (2003).

14. R. Jones, Barry, N. P., Hyde, S. C. W., Tziraki, M., Dainty, J. C., French, P. M. W., Nolte, D. D., Kwolek, K. M., and Melloch, M. R., "Real-time 3-D holographic imaging using photorefractive media including multiple-quantum-well devices," IEEE Journal of Selected Topics in Quantum Electronics **4**, 360-369 (1998).

15. R. Jones, Tziraki, M., French, P. M. W., Kwolek, K. M., Nolte, D. D.,and Melloch, M. R., "Direct-to-video holographic 3-D imaging using photorefractive multiple quantum well devices," Optics Express **2**, 439-448 (1998).

16. Z. Ansari, Y. Gu, M. Tziraki, R. Jones, P. M. W. French, D. D. Nolte, and M. R. Melloch, "Elimination of beam walk-off in low-coherence off-axis photorefractive holography," Optics Letters **26**, 334-336 (2001).

17. P. Yu, M. Mustata, W. Headley, D. D. Nolte, J. J. Turek, and P. M. W. French, ""Optical coherence imaging of rat tumor spheroids," in Coherence Domain Optical Methods in Biomedical Science and Clinical Applications VI, V. V. Tuchin, J. A. Izatt, and J. G. Fujomoto," Proc. SPIE **4619**, 210-218 (2002).

18. S. C. W. Hyde, R. Jones, N. P. Barry, J. C. Dainty, P. M. W. French, K. M. Kwolek, D. D. Nolte, and M. R. Melloch, "Depth-resolved holography through turbid media using photorefraction," Ieee Journal of Selected Topics in Quantum Electronics **2**, 965-975 (1996).

19. R. Jones, S. C. W. Hyde, M. J. Lynn, N. P. Barry, J. C. Dainty, P. M. W. French, K. M. Kwolek, D. D. Nolte, and M. R. Melloch, "Holographic storage and high background imaging using photorefractive multiple quantum wells," Applied Physics Letters **69**, 1837-1839 (1996).

20. I. Lahiri, Pyrak-Nolte, L. J., Nolte, D. D., Melloch, M. R., Kruger, R. A., Bacher, G. D., and Klein, M. B., "Laser-based ultrasound detection using photorefractive quantum wells," Applied Physics Letters **73**, 1041-1043 (1998).

21. Y. Ding, D. D. Nolte, M. R. Melloch, and A. M. Weiner, "Time-domain image processing using dynamic holography," Ieee Journal of Selected Topics in Quantum Electronics **4**, 332-341 (1998).

22. Y. Ding, R. M. Brubaker, D. D. Nolte, M. R. Melloch, and A. M. and Weiner, "Femtosecond pulse shaping by dynamic holograms in photorefractive multiple quantum wells," Optics Letters **22**, 718-720 (1997).

23. Y. Ding, Weiner, A. M., Melloch, M. R., and Nolte, D. D., "Adaptive all-order dispersion compensation of ultrafast laser pulses using dynamic spectral holography," Applied Physics Letters **75**, 3255-3257 (1999).

24. L. Peng, P. Yu, M. R. Melloch, and D. D. Nolte, "Adaptive Interferometer for Optical Coherence-Domain Reflectometry," J. Opt. Soc. Am. B **21**, 1953-1963 (2004).

25. L. Peng, P. Yu, M. R. Melloch, and D. D. Nolte, "High speed adaptive interferometer for optical coherence-domain reflectometry through turbid media," Opt. Lett. **28**, 396-398 (2003).

26. P. Yu, M. Mustata, J. J. Turek, P. M. W. French, M. R. Melloch, and D. D. Nolte, "Holographic optical coherence imaging of tumor spheroids," Appl. Phys. Lett. **83**, 575-577 (2003).

27. Lin Haibo, and Yu Ping, "Speckle Imaging Using Photorefractive Multiple Quantum Wells," in *Conference on Lasers and Electro-Optics/Quantum Electronics and Laser Science Conference and Photonic Applications Systems Technologies*(Optical Society of America, 2006), p. CTuW3.

Chapter 2

Holographic OCI System and Photorefractive Multiple Quantum Wells Device

2.1 Introduction

A holographic OCI system consists of a low-coherence light source, an interferometer to generate depth resolved images, a hologram recording medium and a detection system. The holographic record medium is generally placed in front of a conventional CCD camera, and functions as a coherence filter that passes the coherent (structure carrying) light and rejects the incoherent background during the holographic readout. The optical sectioning of OCI is achieved by measuring the path matched interferences using broadband light sources such as superluminescent diodes or light emitting diodes with a broadband spectrum. Holographic OCI has shown several applications in biomedical imaging such as ultrasound detection through turbid media [1] and tumor tissue image [2]. The detailed studies of tumor spheroids are presented by Yu et al. using time-domain holographic OCI [2, 3] and by Jeong et al. using spatial frequency (Fourier) domain holographic OCI [4, 5].

In this chapter, holographic OCI system using photorefractive multiple quantum

wells (PRQW) is presented. The photorefractive property of PRQW that works as the hologram recording medium is studied by measuring its differential transmission spectrum and beam coupling efficiency. Waves coupling geometries such as degenerate/ nondegenerate four-wave mixing (FWM) and two-wave mixing (TWM) are demonstrated. Except for the traditional FWM imaging, the using of TWM signal to image objects is firstly presented in holographic OCI. The diffraction efficiency of TWM is hundred or even thousand time higher than that of FWM. High diffraction efficiency makes this technique a potential candidate for the next generation of holographic OCI based on PRQW.

2.2 Photorefractive quantum well and its properties

The initial holographic OCI is developed based on bulk photorefractive crystals and volume holograms [6]. However, the readout in volume hologram is difficult due to requirements such as Bragg angle and phase match. In addition, the refreshing rate of bulk crystal was comparable low to satisfy the fast imaging acquisition requirement. The application of PRQW to holographic OCI solved those problems and made the holographic OCI system more efficient and fast.

PRQWs are semiconductor optoelectronic devices [7-9] which have enhanced optical properties based on quantum localization of electrons in a very thin film. The importance of this thin film for holography is the use of interference gratings that

operates in Raman-Nath regime, instead of Bragg regime. Due to this property, it is not required to satisfy the Bragg condition for holographic reconstruction from the diffracted beam. Moreover, PRQWs have the advantage of high sensitivity, which requires comparable low light intensity to generate holographic gratings. Except for the highest sensitivity of any photorefractive materials, PRQWs also have 1 MHz compensation bandwidths [10]. Those enhanced optical properties made this device one of ideal candidates for laser-based adaptive interferometry and imaging applications [11-15].

Figure 2.1 presents the growth structure of a typical transverse-field photorefractive AlGaAs-GaAs multiple quantum wells. The active layer of the PRQW devices is grown by using molecular beam epitaxy, which consists of a multiple quantum well layer composed of a 100 period 70-Å GaAs well and a 50-Å $Al_{0.3}Ga_{0.7}As$ barrier on a semi-insulating GaAs substrate. After the growth, the device is epoxied on a glass plate and the GaAs substrate is removed by using a mechanic process and chemical etching. Then gold contacts are deposited and wires are attached on the two sides of the device so that a transverse electric field can be applied cross the PRQW device, as shown in figure 2.2. The whole device is encapsulated in a plastic box to prevent contamination when the device is used in a holographic OCI system. In order to prevent any beam leakage, black insulating tapes on the front window of the plastic box limit the size of beams irradiated on the device and make sure that beam sizes are smaller than the device window.

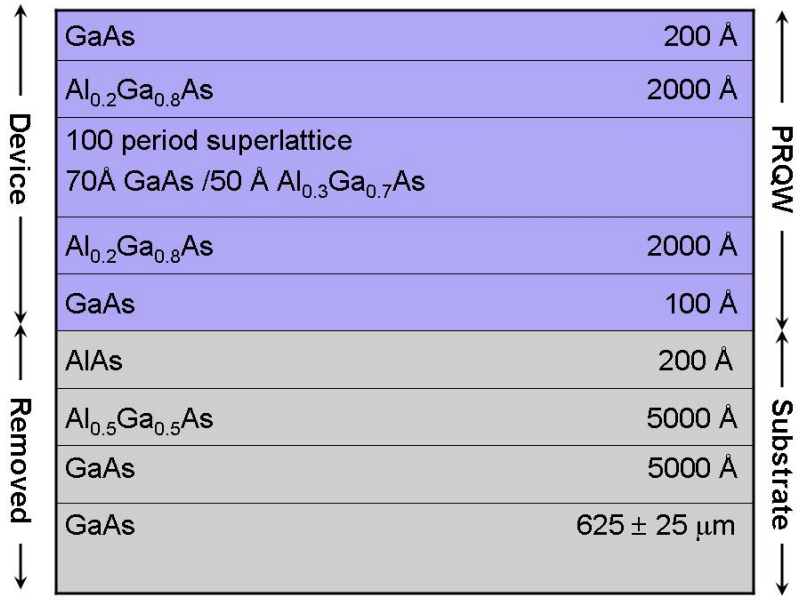

Figure 2.1 Growth structure of a photorefractive multiple quantum wells. Substrate is removed by mechanic and chemical methods. Proton implantation introduces deep levels and defects to trap excitons.

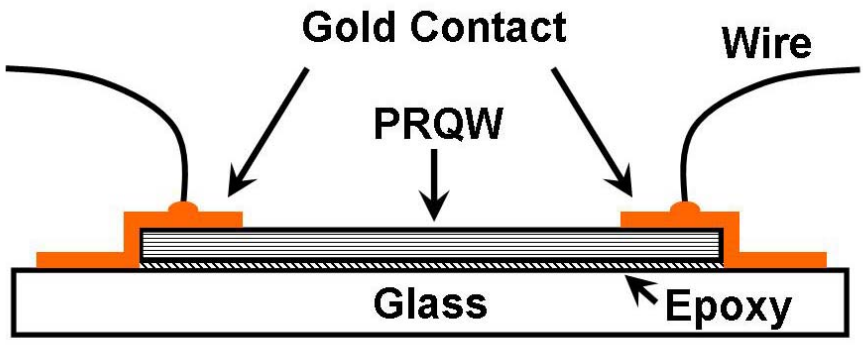

Figure 2.2 Structure of PRQW device in a transverse-field configuration.

When two beams interfere in the PRQW film, the periodic bright and dark interference fringes will be generated with a fringe spacing of

$$\Lambda = \frac{\lambda}{2\sin\theta} \tag{2.1}$$

where θ is the half-angle between the two writing beams and λ is the wavelength of the writing beams. When a high voltage is applied across the film, the photocarriers generated in the bright area will be driven to the dark area by this external electric field. Those photocarriers will be trapped in the dark area by the deep level defects. This effect causes a new distribution of the internal electrical field and this field redistribution results in refractive index changes in the device, which in turn leads to the change of absorption. The device is generally characterized by measuring the differential transmission and wave-mixing efficiency.

The differential transmission is defined as [16]

$$\frac{\Delta T}{T} = \frac{T_{field} - T_0}{T_0} \tag{2.2}$$

where T_{field} is the transmittance of the device with the applied field and T_0 is the transmittance without the applied field. The PRQW was characterized with a differential transmission using the SHIMADZU UV-Visible 2401 PC spectrometer and results are shown in figure 2.3. The electric field induced transmission is above 35%. The spectra reflect the heavy hole exciton and light hole nonlinearity under the external field and the positive and negative bands correspond to the 6π phase changes in the spectrum.

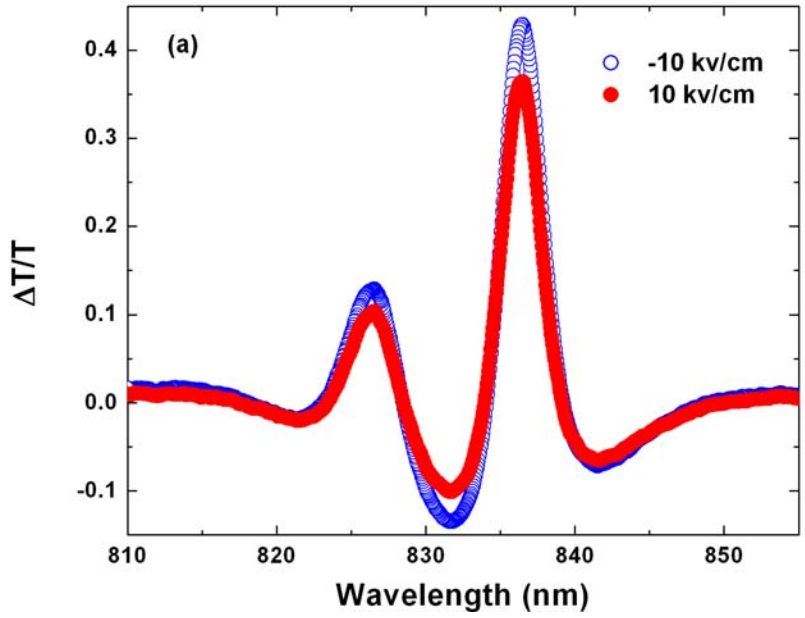

Figure 2.3 Differential transmission spectrum of the PRQW device JK under ±10kV/cm electric field.

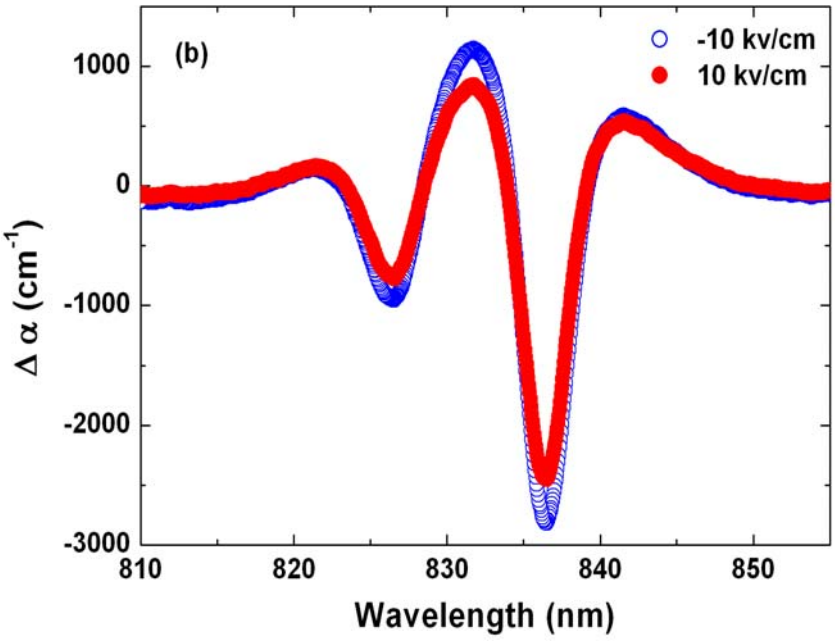

Figure 2.4 Absorption change due to the electro-absorption of quantum confined excitons in the PRQW under electric field.

The differential transmission of the device is due to the electro-absorption of the quantum-confined excitions. The symmetry of electro-absorption can be studied using two oppositely applied electric fields (±10kv/cm). The results indicate that the differential transmission is not very sensitive to the electric filed direction. The differential transmission as a function of wavelength gives the optimum wavelength of the exciton resonance absorption for the best performance in multiple wave-mixing experiments. The change in absorption is calculated from the differential transmission based on the relationship [10]

$$\Delta\alpha = -\frac{1}{L}\ln(1+\frac{\Delta T}{T}) \tag{2.3}$$

where L is the thickness of the active electro-optical layer, and the differential absorption is plotted as a function of wavelength in figure 2.4. The change in refractive index can be calculated from the differential absorption using the Kramers-Kronig relations described in the references [17, 18].

Our PRQW device operates in the transverse field geometry, also known as the Franz-Keldysh geometry. The detailed information about the operation of this kind of PRQW has been described by Wang et al [16]. The Franz-Keldysh geometry defines a transverse electric field of several hundreds to a thousand volts applied across the PRQW through the gold contacts to induce the photorefractive effect. Except for the function of electrodes, the gold contacts also define a window which lets the PRQW work in several wave coupling modes, such as two-wave mixing, degenerate four-wave mixing and

nondegenerate four-wave mixing.

2.3 Two-Wave Mixing of the PRQW

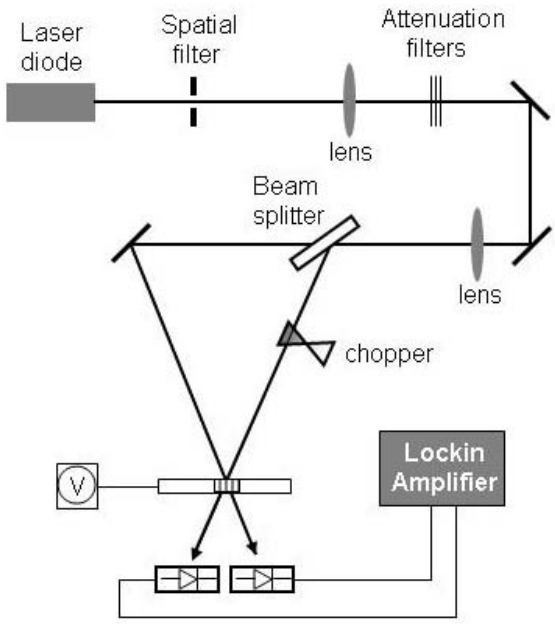

Figure 2.5 Two-wave mixing system using PRQW. A spatial filter and two lenses are used to collimate the beam.

During the hologram writing process, if the wavelength of the writing beams is in the exciton absorption regime, the writing beams will be self-diffracted by the holographic grating. This is called a degenerated four-wave mixing due to the same wavelengths for both the writing beams and the probe beam. Since all wavelengths involved in this four-wave mixing process are the same, one of the diffracted signals of a writing beam will be superimposed with the transmission of the other writing beam. The diffracted signal generally shows a phase different with the transmitted beam, which leads to the

interference between those two beams. This interference between transmitted and diffracted waves is called two-wave mixing.

Figure 2.5 presents a typical TWM system [19] which we used to study the TWM efficiency of the PRQW. A continue wave (CW) laser from a laser diode with variable wavelength by tuning the temperature is employed as the light source. The temperature is adjusted to tune the wavelength to the maximum excition absorption of the PRQW. The wavelength in our experiment is 834 nm. A spatial filter between two lenses is placed in the beam path to collimate and shape the incident beam. Neutral density (ND) filters are used to attenuate the beam intensity and change the intensity ratio of the writing beam. An external electric field of 9kV/cm is applied across the PRQW device during the experiment. A chopper, a lock-in amplifier and two silicon detectors work as the detection system. In order to pick up the TWM signal, one of the writing beams is chopped. The energy transferred from this chopped beam to the other writing beam is collected using a lock-in amplifier system by measuring the modulated signal in the transmitted non-chopped beam.

When the reference and signal paths match within the coherence length the intensity is modulated by the interference fringes with a fringe spacing, Λ given by equation 2.1. The average intensity distribution in the PRQW window is given by

$$I(x) = \bar{I}[1 + m(x,\tau)\cos(\frac{2\pi x}{\Lambda} + \Phi)] \tag{2.4}$$

where $\bar{I}$ is the average intensity, x is the distance across the window, Φ is an arbitrary

phase, and $m(x,\tau)$ is the modulation-index function. The modulation index function is the most important factor since it provides information concerning coherence properties. Later we will see that it is the key factor in the TWM efficiency of the PRQW.

In photorefractive materials, photon absorption and charged carrier generation is the first step in the photorefractive process. Those photo-carriers (generated in bright fringes) will diffuse to and be trapped in the deep level defects (in dark fringes) which generate an internal spatially modulated electric field. The redistribution of carriers changes the local absorption of the defects' area and generates an absorption grating. Also, the internal modulated field induces a refractive index grating. Thus, the coupling effects present in both gratings. Based on the quadratic electro-optical description, the absorption and refractive index changes, $\Delta\alpha$ and Δn, are given by [16, 20]

$$\Delta n = -n^3 s_1 E_0^2 m(x,\tau)\,, \qquad \Delta\alpha = -\frac{4\pi}{\lambda} n^3 s_2 E_0^2 m(x,\tau) \tag{2.5}$$

where s_1 and s_2 are the quadratic electro-optic coefficients, respectively. E_0 is the externally applied electrical filed, $m(x,\tau)$ is the modulation-index function and λ is the wavelength of the writing beams.

The photorefractive gain is defined as the ratio of the mixed intensity to the unmixed intensity and can be expressed in term of the intensities of the writing beams I_1, I_2, the sample thickness L and the absorption of the device α as [9]

$$\gamma = \frac{I_1(L)}{I_1(0)e^{-\alpha_0 L}} = 1 + \sqrt{\frac{I_2(0)}{I_1(0)}}\left[\frac{2\pi\ n_1 L}{\lambda\cos\theta'}\sin\phi + \frac{\alpha_1 L}{2\cos\theta'}\cos\phi\right] \tag{2.6}$$

where $\sin\theta' = (1/n)\sin\theta_i$, with θ_i being the half angle between the writing beams, and n_1

is the complex part of the refractive index. The TWM efficiency is defined as a ratio of the intensity differences, between the transmitted signal in presence of mixing and the transmitted signal in absence of mixing, to the intensity of transmitted signal with zero mixing,

$$\frac{\Delta I}{I} = \frac{I_S(I_R, E_0, L) - I_S(0, E_0, L)}{I_S(0, E_0, L)} \tag{2.7}$$

I_S is the transmitted signal intensity; I_R indicates the presence of wave mixing; E_0 is the external electric field; L is the quantum well window size. The TWM efficiency is generally about 10% and can be as high as 30%.

2.4 Four-Wave Mixing of the PRQW

The multi-wave mixing in the PRQW device involved four waves is called four-wave mixing (FWM). Depending on the selected wavelength in the writing and probe beams, FWM is divided into two categories: degenerate FWM and nondegenerate FWM. In degenerate FWM, writing beams also work as the probe beam to read out the hologram. Therefore, the probe beam has the same wavelength as the writing beams, which corresponds to the maxima exciton absorption of the PRQW device. In this case, the read-out process is considered to be a self-diffraction process. However, in the nondegenerate FWM, the probe beam and writing beams are generally from different light sources.

The basic requirement for the writing beams is that the wavelength should be above

the bandgap of absorption of the PRQW. In order to achieve the depth resolution, a broadband low coherence light source (superluminescent diode, LEDs or femtosecond laser) should be used. As for the probe beam, the wavelength should be specified by the maximum exciton absorption of the PRQW. It can be a single wavelength source, such as a laser diode. Both configurations detect the first-order diffraction of the probe. Either a silicon diode (generally used in a lock-in amplify system) or a CCD camera is used to detect the diffracted signal (FWM), depending on the needs of the experiment.

2.4.1 Nondegenerate FWM

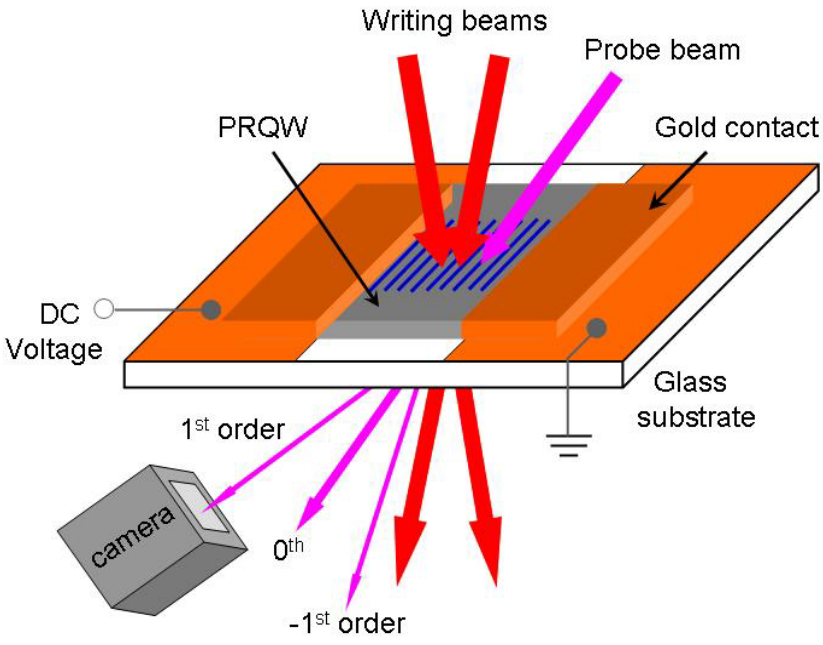

Figure 2.6 Schematic of the PRQW in a nondegenerate FWM geometry.

Figure 2.6 presents a typical nondegenerate FWM configuration using the PRQW. Two light sources with different wavelengths are used as the writing beams and the probe beam. The wavelength of the writing beam is above the bandgap of the quantum well device to induce high absorption in the PRQW. In principle, the writing beam can be monochromatic (no depth resolving ability) or broadband depending on the system design. In practice, a low coherent light source, such as femtosecond laser or super-luminescence diodes, is employed to achieve the depth resolution.

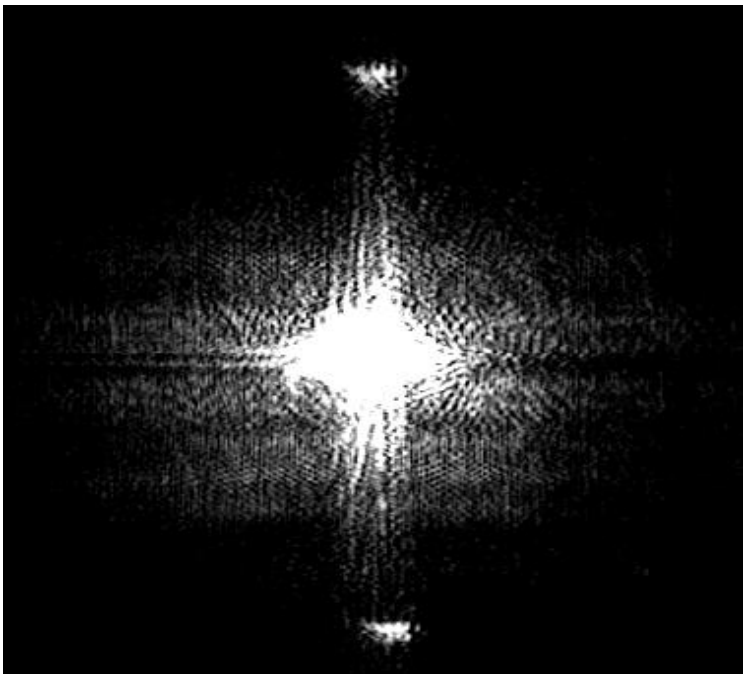

Figure 2.7 Image of the zeroth and two first order diffractions in nondegenerate FWM using PRQW.

A holographic image is generated by imaging the first order diffraction of the probe beam. As shown in figure 2.7, two first-order diffraction beams are symmetrically

distributed on the two sides of the zeroth order (transmission) beam. The intensity of the first-order beams is much weaker than that of the transmission beam. Thus a spatial filter is required to block the strong transmission and cut one of the diffracted beams out for imaging. Generally, the diffraction signal that is angularly separated from the transmitted writing and probe beams is selected to image the object. The noise from the leakage of the transmission beam and scattering of the writing beams should be suppressed. The intensity of the diffracted signal (FWM) is generally very small and is related to both the absorption and refractive index gratings in the PRQW. The diffraction efficiency for a nondegenerated FWM configuration is proportional to

$$\eta \propto (\frac{\pi \Delta n L}{\lambda \cos\theta'})^2 + (\frac{\Delta \alpha L}{4\cos\theta'})^2 \tag{2.7}$$

for a thin grating with the thickness of L. Here θ' is the incident angle of the probe beam. Based on equation (2.5), the absorption and refractive index changes $\Delta\alpha$ and Δn linearly depend on the modulation index function $m(x,\tau)$. This leads to a direct dependence of the diffraction efficiency on the square of the modulation. Thus, the total diffraction efficiency is proportional to

$$\eta \propto \frac{1}{W}\int_{-W/2}^{W/2} m(x,\tau)dx \tag{2.8}$$

where W is the width of the PRQW window defined by the gold contacts.

The nondegenerate FWM configuration using a separate probe beam gives this method more advantages. First, due to the wavelength difference between the writing and read beams, it is possible to use a long-pass filter or a band-pass filter to reject

background as well as incoherently scattered light from the writing beams, which can improve the image quality and signal to noise ratio. Secondly, with an independent probe beam tuned to the resonant wavelength of the PRWQ, any photon energy above the bandgap of the semiconductor device can be used as the writing beams to write the hologram. So the spectroscopic information can be extracted from the sample by choosing different wavelengths of the writing beams in the near-infrared and visible spectrum. In this project, a nondegenerate FWM configuration is used to generate holographic imaging.

2.4.2 Degenerate FWM

As shown in figure 2.8, a degenerate FWM configuration employs only one light source for both writing and probe beams, which makes the imaging system simple. The holographic image is generated by the self-diffraction of the reference beam. As mentioned above, one of the first order diffractions of the reference beam is superimposed with the transmission of the signal beam. Thus only one of the diffraction signals can be used to image objects. The degenerate FWM signal relies on self-diffraction of the writing beams from the photorefractive grating. The diffraction efficiency for a degenerate FWM configuration is proportional to

$$\eta \propto (\frac{\pi \Delta n L}{\lambda})^2 + (\frac{\Delta \alpha L}{4})^2 \tag{2.9}$$

for a thin grating with the thickness of L.

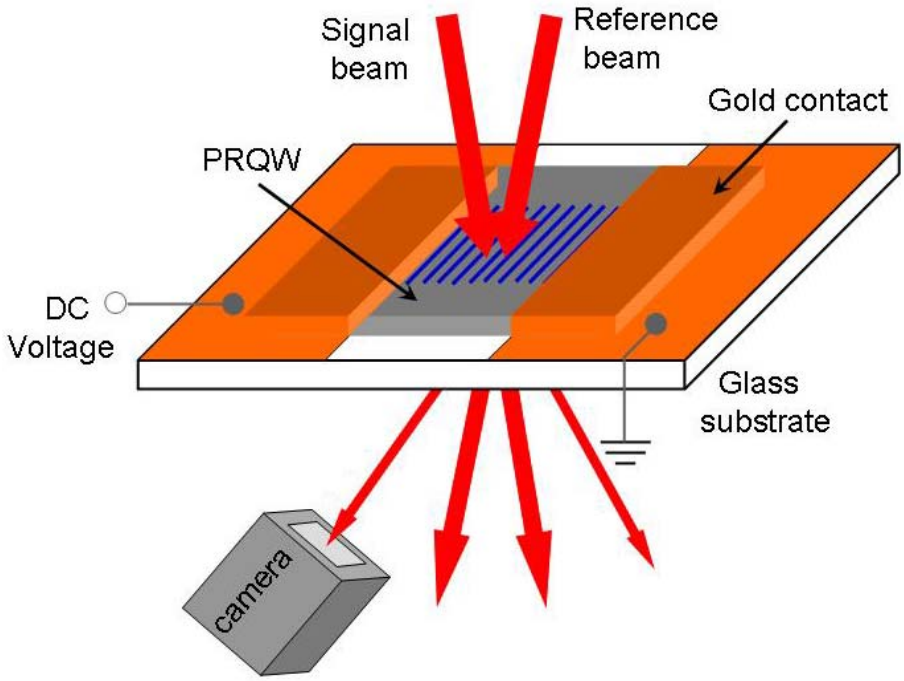

Figure 2.8 Schematic of the PRQWs in a degenerate FWM geometry.

The PRQW devices operate under strong electric fields and the beam intensities generate high photoconductivity, so the devices experience Joule heating. The Joule heating must be kept below a critical value, or thermal run-away occurs and the device may be destroyed. The degenerate FWM configuration combines the probe beam with the reference beam, decreasing the total intensity irradiated on the PRQW device. This insures that the quantum device works under a low Joule heating condition, prolonging the lifetime of the quantum device. Moreover, the combination of the reference beam and probe beam can prevent additional hologram erasure. This erasure cannot be avoided in nondegenerate FWM configurations due to the independent probe beam. In addition,

higher reference intensities generate brighter holographic reconstructions, whereas in the nondegenerate configuration the reference intensity must be matched to the signal intensity to prevent hologram erasure.

Table 2.1 Wave coupling efficiency of the PRQW device labeled as JK

Type of measurement	Efficiency
Two-wave mixing	28 %
Degenerate four-wave mixing	0.019%
Non-degenerate four-wave mixing	0.054%

Table 2.1 presents a comparison of the wave coupling efficiencies of the PRQW device (labeled as JK) measured by the holographic OCI system. The TWM efficiency is measured using an 834 nm wavelength laser diode. The efficiency is around 28%. The degenerate FWM efficiency is measured using an 830 nm broadband superluminescent diode with a coherent length of 20 microns. For non-degenerate FWM, this superluminescent diode is still used as writing beam and an 834 nm laser diode is used as the probe beam. The TWM efficiency is around 1000 times of the degenerate FWM efficiency. The nondegenerate FWM efficiency is higher than the degenerate case, but much lower than the TWM efficiency. In most current system, a FWM signal is used as the signal for the holographic imaging. With much high efficiency, TWM can improve the imaging quality and signal to noise ratio if it can be used for imaging purpose.

2.5 Holographic Optical Coherence Imaging System

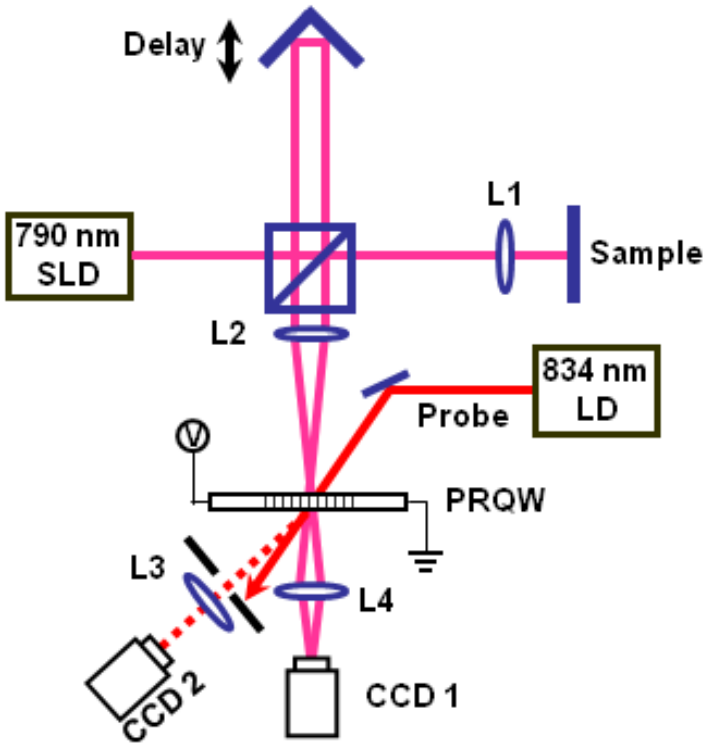

Figure 2.9 Holographic OCI system with low coherence light source.

As shown in figure 2.9, the holographic OCI includes the following four parts: 1) two light sources, 2) an interferometer, 3) PRQW, 4) two CCD cameras. The holographic OCI shares the same principle with other coherence domain imaging systems such as optical coherence tomography (OCT). By employing a low coherence interferometry, both techniques use short-coherence light sources to achieve the depth resolution. OCT uses temporal heterodyne detection at a single point followed by the signal demodulation by electronics. In OCI, the interferometric detection is based on the spatial heterodyne in a full field of view with holographic readout.

The PRQW converts spatial intensity modulations, which include structure information and non-uniform background, such as speckles, into diffraction gratings. Spatial intensity modulation is critical because PRQW respond to the intensity gradient rather than to the intensity itself. As shown in figure 2.9, a 790 nm broadband laser diode (~10 mW) with 30 nm bandwidth is used in the holographic OCI system to generate holograms using a non-degenerate FWM geometry. The beam intensity ratio between the reference and signal beam is around 1:1 to achieve a high modulation contrast. The intensities of the writing beams and probe beam are set to be close to each other. A DC voltage of 1000 V is applied across the 1mm PRQW window and the Joule heating monitor indicates 0.6 V (below 1 V is safe) across a 1MΩ resistance. A variable ND filter is used in the reference beam to balance the intensity between the two arms of the writing beams. A fringe spacing of ~30 microns is used for the holographic diffracting grating.

A laser diode (10 mW, 834 nm) works as the probe beam. The wavelength of the probe beam can be tuned in small ranges by controlling the temperature of diode mount. In order to read the hologram with a high efficiency, the wavelength of the probe beam is set exactly at the exciton absorption peak of the PRQW, which is achieved by a calibration in advance. Total intensity of the writing beams, as well as the intensity ratio of the reference and signal beams, are tuned to optimize the diffraction signal and to keep the Joule heating as low as possible. For example, due to the stronger reflection of test chart bars, a set of ND filters are used in the main input beam to reduce the intensity of both writing beams. With

a diffuser on the object plane, ND filters have to be set in the reference arm to balance the highly scattered signal beam. A USAF 1951 Test Chart with a serial of known length and width bars is used as a standard sample to calibrate the system resolution. The detailed information of the test chart is listed in appendix I. Figure 2.10 presents our first holographic images of the number and horizontal bars of the test chart using a low coherence light source.

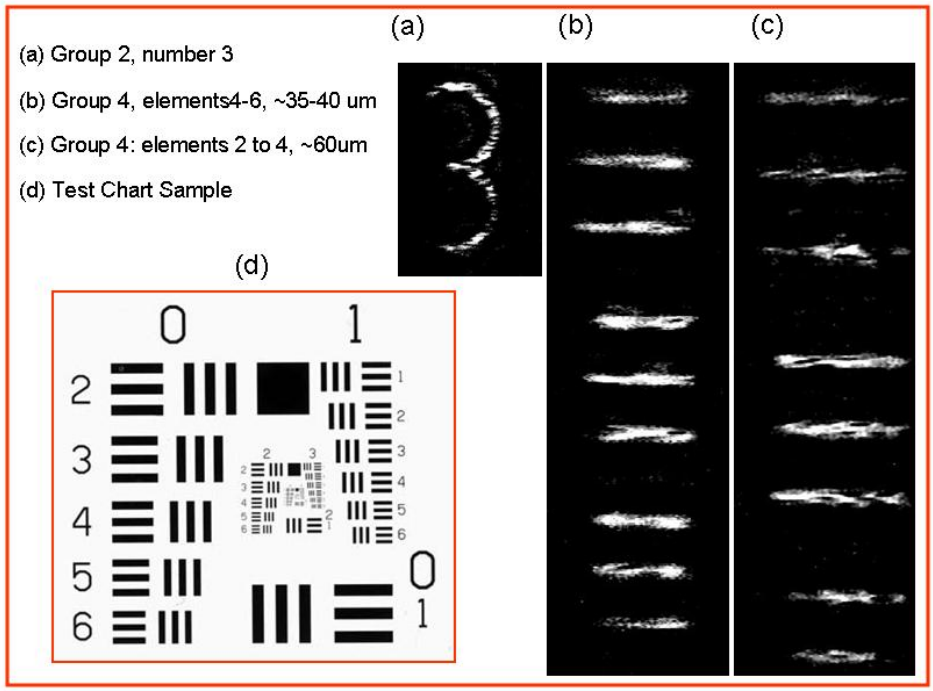

Figure 2.10 Holographic images of the test chart. (a)The number of 3 in group 2; (b) horizontal bars on group 4, elements 4-6 (~35-40 microns); (c) horizontal bars on group 4, elements 2-4 (~ 60 microns); (d) direct image of test chart.

Figure 2.11 presents several speckle images of a 10 degree diffuser including a direct speckle image by blocking the reference beam, the image of speckle modulated by interference fringes, and the corresponding holographic speckle image. It is interesting to

notice that the holographic speckle image distribution is not uniform in the PRQW window in figure (c), although the speckle patterns almost fill the whole window in figure (a). In figure (c), speckle patterns are mostly distributed in the right side of the window and are very weak in the left side of the window. This phenomenon is caused by the property of the photorefractive quantum well itself.

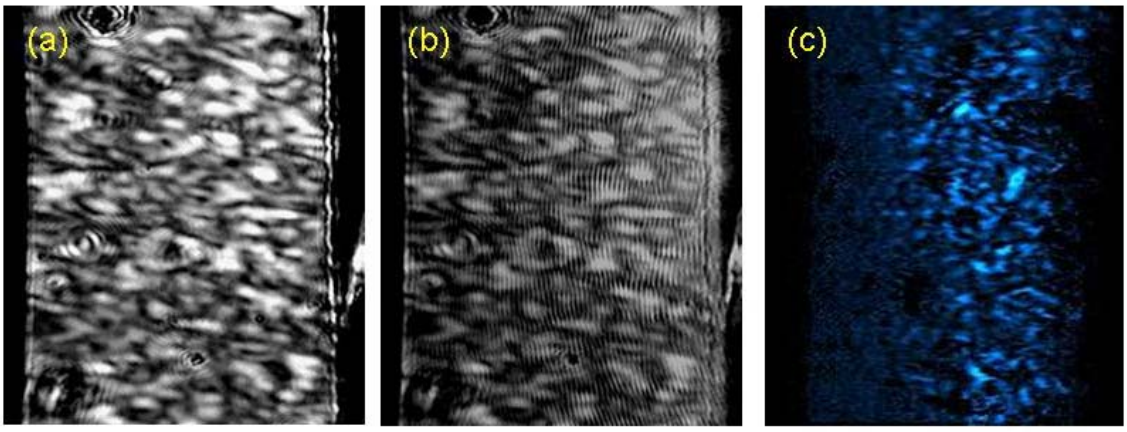

Figure 2.11 Speckle images. (a) Direct speckle image; (b) speckle image with interference modulation; (c) holographic speckle image.

As discussed above, the PRQW film responds only to the gradient in intensity instead of to the intensity itself. Thus, these speckle patterns modulated by fringes in figure (b) contribute to the holographic images in figure (c). Due to the intended non-uniform distribution of the reference beam in figure (b), the interference fringes mainly locate on the right side of the window, which results in the speckle non-uniform distribution in figure (c). In practice, the speckles shown in figure (a) have spatial

intensity gradients that can write holograms and diffract light too. However, the spatial bandwidth of this intensity gradient disperses the diffracted beam and limits the intensity of the beam captured by the reconstruction. This kind of speckle is known as the background speckle, which can be effectively removed by using a vibrating mirror with a frequency slower than the holographic film, but faster than the frame rate of the camera. The detailed discussion of the background speckle reduction will be given in Chapter 5.

2.6 Two Wave Mixing Imaging

In addition to four-wave mixing, two-wave mixing (TWM) is another nonlinear beam coupling process for photorefractive materials that attracts lots of interests. Although the TWM process of a PRQW has been studied in detail [21, 22], optical imaging systems using the TWM process of PRQW has not yet been reported. The two-wave coupling process is not considered as a good way to do imaging since it is difficult to quickly extract depth resolved information from strong transmission of the signal beam. However, as shown in table 2.1, the higher energy transfer efficiency makes this method a promising candidate for high quality imaging.

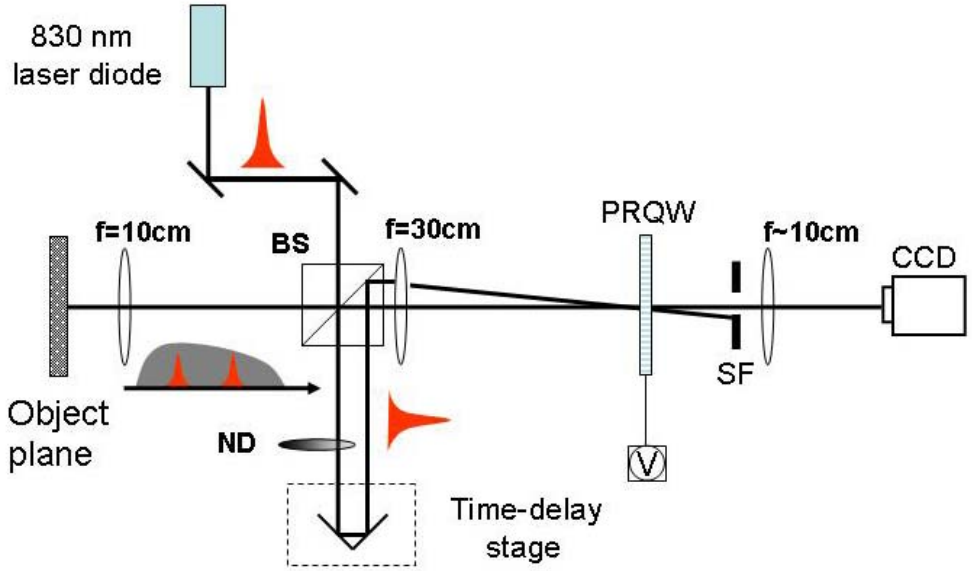

Figure 2.12 Two-wave mixing image system using an 830 nm broadband super-luminescent diode. BS: Beam splitter; SF: spatial filter; ND: Variable neutral density filter.

Here we use a PRQW to generate a two-wave mixing image by employing an 830 nm broadband (30 nm) superluminescent diode. The TWM imaging system is actually a revised OCI system using a FWM signal, as shown in figure 2.12. A variable ND filter is placed in the reference arm to change the intensity ratio of the writing beams. An intensity ratio of 1:15 between signal and reference beams is selected to optimize the wave coupling efficiency. The reference beam is blocked by a spatial filter after the PRQW. A conventional CCD camera is used to capture the images.

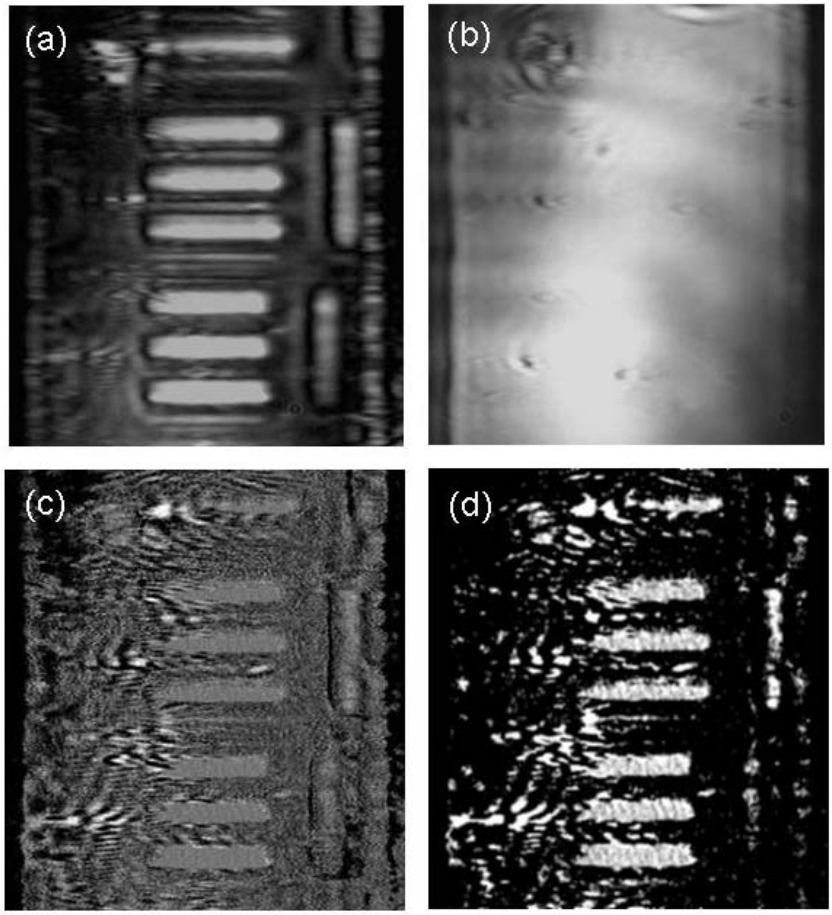

Figure 2.13 Two-wave mixing images of USAF 1951 Test Chart group 4, element 6. (a) Direct image of the test chart bar with reference beam blocked; (b) image of test chart bar with reference beam; (c) two-wave mixing image with background subtraction; (d) two-wave mixing image after further processing.

A USAF 1951 test chart is placed on the object plane to generate TWM images. An area with many of 35-micron bars (group 4, element 6) is selected. A 1kV DC voltage is applied across the PRQW to induce the photorefractive effect. Two sets of images of the test chart are collected by the CCD camera with and without path match. The auto-exposure property of CCD should be turned off. The difference between those two sets of images gives the TWM image since the energy transferred from the reference

beam to the signal beam survives in this subtraction and this energy transfer is the result of two-wave coupling. The measured results are shown in figure 2.13.

In figure 2.13 (a), a direct image of two sets of horizontal bars is presented. Also, some defects in the PRQW are clearly shown as brighter spots due to the leakage of the signal beam. With the strong reference beam shown in figure (b), the direct image of the bars in figure (a) is erased. No structure information of the object can be extracted in the direct image with the presence of both writing beams. However, the subtraction of the holographic images with and without path matching shows the structure of the sample, as shown in figure (c). This raw image is further processed by changing the image contrast and intensity threshold. The processed image is illustrated in figure (d). Compared with figure (a), most of the horizontal bars are clearly presented. The vertical bars are not intense enough to survive and give clear profile of the object after the process using the intensity threshold. This is because the width of the bar is not wide enough to be effectively modulated by the interference fringes. This effect will be discussed in Chapter 3. Furthermore, the non-uniform diffraction efficiency across the PRQW window, especially for the low efficiency on the edge of the window, is another reason for the blurred vertical bars.

The TWM imaging has more noise than that of the FWM imaging. Noises mainly come from three areas: (1) scattered light by the PRQW edges, (2) leakage from those defects on the PRQW, and (3) the intensity fluctuation cause by the delay change. Based

on figure 2.13(d), we can see that the second kind of noise may be the most serious, which is not only present with high a intensity background, but also shows an irregular spread distribution. Thus, high quality quantum well devices are necessary to effectively remove this kind of noise. The first kind of noise contributes to the background with high intensity too, but is limited in small area along the edge of the window. The third kind of noise generally gives a comparably uniform background that can be removed by changing the intensity threshold.

For the TWM signal, the phase is a complicated problem. In order to achieve good images using the TWM system, phases need to be understood. The phase can change from 0 to 6π for a TWM signal. When a CCD is used in a TWM imaging system, the TWM signal with different phases will be added together. A signal with positive phases will cancel a signal with negative phases. Thus, the characteristic structures of the sample can be either bright or dark. In order to achieve better image quality, this problem should be resolved using the pulse shaping method.

BIBLIOGRAPHY

1. P. Yu, L. Peng, D. D. Nolte, and M. R. Melloch, "Ultrasound detection through turbid media," Opt. Lett. **28**, 819-821 (2003).

2. M. Mustata P. Yu, J. J. Turek, P. M. W. French, M. R. Melloch, and D. D. Nolte, "Holographic optical coherence imaging of tumor spheroids," Appl. Phys. Lett. **83**, 575-577 (2003).

3. M. Mustata P. Yu, L. Peng, J. J. Turek, M. R. Melloch, P. M. W. French, and D. D. Nolte, "Holographic optical coherence imaging of rat osteogenic sarcoma tumor spheroids," Appl. Opt. **43**, 4862-4873 (2004).

4. Leilei Peng Kwan Jeong, John J. Turek, Michael R. Melloch, and David D. Nolte, "Fourier-domain holographic optical coherence imaging of tumor spheroids and mouse eye," Appl. Opt. **44**, 1798-1805 (2005).

5. John J. Truek Kwan Jeong, and David D. Nolte, "Fourier-domain digital holographic optical coherence imaging of living tissue," Appl. Opt. **46**, 4999-5008 (2007).

6. S. C. W. Hyde, R. Jones, N. P. Barry, J. C. Dainty, P. M. W. French, K. M. Kwolek, D. D. Nolte, and M. R. Melloch, "Depth-resolved holography through turbid media using photorefraction," Ieee Journal of Selected Topics in Quantum Electronics **2**, 965-975 (1996).

7. D. D. Nolte, D. H. Olson, G. E. Doran, W. H. Knox, and A. M. Glass, "Resonant photodiffractive effect in semi-insulating multiple quantum wells," J. Opt. Soc. Am. B **7**, 2217–2225 (1990).

8. D. D. Nolte, T. Cubel, L. J. Pyrak-Nolte, and M. R. Melloch, "Adaptive beam combining and interferometry with photorefractive quantum wells,," J. Opt. Soc. Am. B. **18**, 195–205 (2001).

9. D. D. Nolte, "Semi-insulating semiconductor heterostructures: Optoelectronic properties and applications," J. Appl. Phys. **1999**, 6259-6289 (1999).

10. S. Balasubramanian, Y. Ding I. Lahiri, M.R. Melloch, and D. D. Nolte, "Two-wave-mixing dynamics and nonlinear hot-electron transport in transverse-geometry photorefractive quantum wells studied by moving gratings," Appl. Phys. B **68**, 863-869 (1999).

11. R. Jones, S. C. W. Hyde, M. J. Lynn, N. P. Barry, J. C. Dainty, P. M. W. French, K. M.

Kwolek, D. D. Nolte, and M. R. Melloch, "Holographic storage and high background imaging using photorefractive multiple quantum wells," Appl. Phys. Lett. **69**, 1837–1839 (1996).

12. R. M. Brubaker Y. Ding, D. D. Nolte, M. R. Melloch, and A. M. Weiner, "Femtosecond pulse shaping by dynamic holograms in photorefractive multiple quantum wells,," Opt. Lett. **22**, 718–720 (1997).

13. D. D. Nolte Y. Ding, M. R. Melloch, and A. M. Weiner, "Timedomain image processing using dynamic holography," IEEE J. Sel. Top. Quantum Electron. **4**, 332–341 (1998).

14. A. M. Weiner Y. Ding, M. R. Melloch, and D. D. Nolte, "Adaptiveall-order dispersion compensation of ultrafast laser pulses using dynamic spectral holography," Appl. Phys. Lett. **75**, 3255–3257 (1999).

15. L. Pyrak-Nolte I. Lahiri, D. D. Nolte, M. Melloch, R. Kruger, G. Bacher, and M. Klein, "Laser-based ultrasound detection using photorefractive quantum wells," Appl. Phys. Lett. **73**, 1041-1043 (1998).

16. R. M. Brubaker Q. N. Wang, D. D. Nolte, and M. R. Melloch, "Photorefractive quantum wells: transverse Franz-Keldysh geometry," J. Opt. Soc. Am. B **9**, 1626 (1992).

17. D. C. Hutchings, M. Sheik-Bahae, D. J. Hagan, and E.W. Van Stryland, "Kramers-Krönig relations in nonlinear optics," OPt. Quantum Electronics **24**, 1-30 (1992).

18. B. O. Seraphin and N. Bottka, "Franz-Keldysh effect of the refractive index in semiconductors," Physical Review **139**, 560 (1965).

19. Sunder Balasubramanian Michael Gramlich, and Ping Yu "Angle dependence of two-wave mixing efficiency in photorefractive multiple quantum wells " Appl. Phys. Lett. **89**, 222106 (2006).

20. Q. Wang and M. R. Melloch D. D. Nolte, "Robust infrared gratings in photorefractive quantum wells generated by an above-bandgap laser," Appl. Phys. Lett. **58**, 2067 (1991).

21. I. Lahiri S. Balasubramanian, Y. Ding, M.R. Melloch, D. D. Nolte, "Two-wave-mixing dynamics and nonlinear hot-electron transport in transverse-geometry photorefractive quantum wells studied by moving gratings," Appl. Phys. B **68**, 863-869 (1999).

22. M.R. Melloch and D. D. Nolte Q. N. Wang, "Two-wave mixing in photorefractive AlGaAs/GaAs quantum wells," Appl. Phys. Lett. **59**, 256-258 (1991).

Chapter 3

Speckle Mechanism in OCI

3.1 Introduction

Holographic optical imaging technique using PRQW has shown great potential in biomedical imaging applications, such as laser based ultrasound detection [1-4], adaptive optical coherence domain reflectometry (OCDR) [5,6] and holographic optical coherence imaging (OCI) [7-11]. In all of these applications, speckle images are strongly influenced by holographic fringes as well as photorefractive effect. The PRQW has been used to reject unwanted speckle in some applications, such as laser based ultrasound detection. On the other hand, it has been used to acquire useful speckle images in other applications. For example, dynamic speckle in holographic coherence domain imaging has been applied to analyze the cellular movement and healthy state of a tumor tissue. The speckle plays an important role in holographic optical imaging, but the mechanism underlying the speckle imaging is still not clear.

In holographic optical imaging using a PRQW, numerical aperture (NA) of the detection is large compared to other coherence domain imaging technique, such as optical coherence tomography. The large NA is required by the field of view in the imaging

system, which is related to the device window size. Photons from a large angle scattering are collected so that the size of speckle pattern is comparable to the fringe spacing of the interference. Therefore, the holographic grating formed in a PRQW can be used to select and manipulate speckle patterns. In this chapter, we provide the first study [12] for the contrast mechanism of speckle imaging in the holographic optical imaging using AlGaAs/GaAs photorefractive quantum well. A CW laser and diffusers are used to provide well controlled speckle patterns.

3.2 Statistics of Speckle Patterns

It is well known that speckle is generated whenever coherent radiation is scattered from a surface or subject whose roughness or size is comparable to or greater than the wavelength of the radiation. The scattered wavelets from different depths and positions of the rough surface interact with one another to generate an interference pattern. Due to the random direction and random phase of these wavelets, the interference pattern will be an array of bright and dark spots with irregular shape, instead of interference fringes we saw in the Young's double slits experiment. Speckle is an important topic for optically imaging of biomedical objects with irregular shapes or surface such as tumor tissue and human skin.

3.2.1 Imaging system for direct speckle image

As shown in figure 3.1, we use a 4-F system to relay the image from the object plane to image plane. Two lenses with focal lengths of 10cm and 30cm respectively are used in the imaging system to generate an enlarged image in PRQW. This is a typical imaging system that has been used in optical coherence imaging [12]. The speckle patterns are acquired by a CCD camera at the image plane (x, y) of the imaging system.

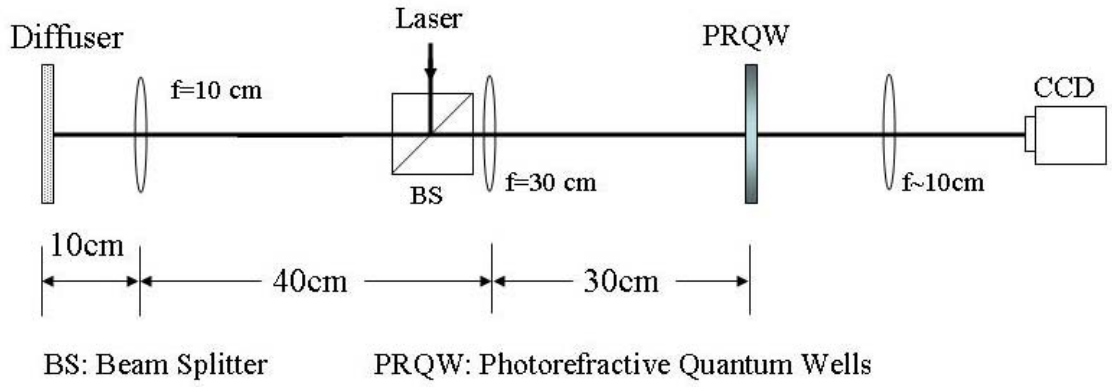

Figure 3.1 Imaging system to acquire the direct image of the objects.

In order to generate well controlled speckles, speckle patterns are generated by light shape diffusers (Newport Cooperation) placed at the object plane of an imaging system under illumination of a He-Ne Laser. The light shape diffusers are primarily used to smooth and homogenize uneven distribution of various light sources. Light can be shaped into a specific cone angle by using these diffusers. The light shape diffusers we

used have the cone angle of 10°, 15°, 20°, and 25°. The surface of diffusers is holographically replicated on polycarbonate from a holographic master, which has completely random, non-periodic structures that can be thought of as randomized micro lens lets. When placing the diffusers in optical path, they diverge light resembling a negative lens. They are wavelength independent and will work in white, monochromatic, coherent, or incoherent light [13].

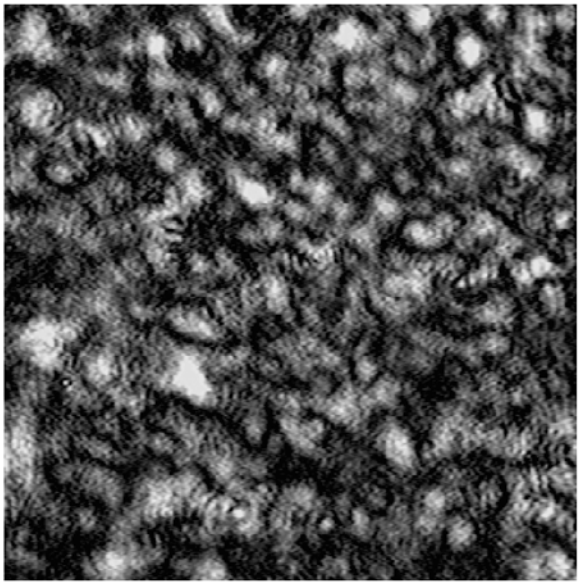

Figure 3.2 Direct image of speckle generated by 15° diffuser and He-Ne laser.

The speckle pattern generated by a 15° diffuser and acquired by the CCD camera is displayed in figure 3.2. To maintain a good contrast, the CCD camera has been set to an auto-exposure mode. In the experimental procedure, a movie mode is used at the

beginning. When desired speckle pattern was observed, the movie was stopped and then the frame image was saved. A 5mW He-Ne laser is used in the experiments. ND filters are used to change the incident intensity to avoid the saturation on CCD.

3.2.2 Autocorrelation algorithm for speckle size evaluation

The average speckle size of a speckle image can be estimated by calculating the autocovariance function of the digitized intensity speckle pattern. The autocovariance function corresponds to the normalized autocorrelation function of the intensity; which has a zero base and its full width at half maximum (FWHM) provides a reasonable measurement of the "average width" of a speckle [14, 15]. In order to use autocorrelation function method to calculate the average speckle size, it requires sufficient sampling speckles in an image to give a reasonable statistical evaluation. If $I(x_1,y_1)$ and $I(x_2,y_2)$ represent the intensities of two points in the imaging plane (x,y), the intensity autocorrelation function is defended by equation

$$R_I(\delta x,\delta y) = < I(x_1,y_1)I(x_2,y_2) > \tag{3.1}$$

where $\delta x = x_1 - x_2$ and $\delta y = y_1 - y_2$. <> corresponds to a spatial average. If we set (x_2,y_2) as the origin of the coordinate and $x_1 = x$, $y_1 = y$, the equation (3.1) gives

$$R_I(\delta x,\delta y) = R_I(x,y) \tag{3.2}$$

The normalized autocovariance function of the intensity $C_I(x,y)$ is given by equation

$$C_I(x,y) = \frac{R_I(x,y) - < I(x,y) >^2}{< I(x,y)^2 > - < I(x,y) >^2} \tag{3.3}$$

A Matlab program is used to calculate the autocovariance function of the image shown in figure 3.2. The programs are listed in the Appendix II. In figure 3.3, the calculated autocovariance functions are shown. And the FWHM of the calculated function gives the average speckle size of the speckle pattern shown in figure 3.2.

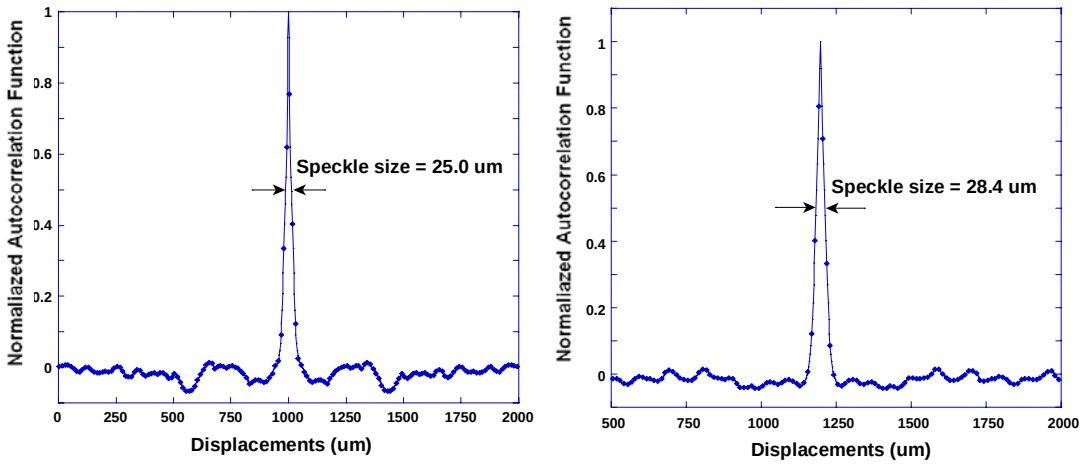

Figure 3.3 Averaged speckle size calculated by autocorrelation method along horizontal direction (left) and vertical direction (vertical) of the digitized speckles pattern given in figure 3.2.

3.3 Intensity Threshold of Speckles

So far, the average speckle size evaluation using the normalized autocorrelation function of the speckle image has been studied. However, some applications require the description of speckle size as the function of intensity threshold of the speckle image. Figure 3.4 presents 3-dimentional speckle image with intensity along vertical direction. It

is obvious that the average speckle area is variable for different intensity thresholds. With the increase of intensity threshold, the average area for a specific speckle will decrease or even disappear from the 2-dimentional speckle pattern.

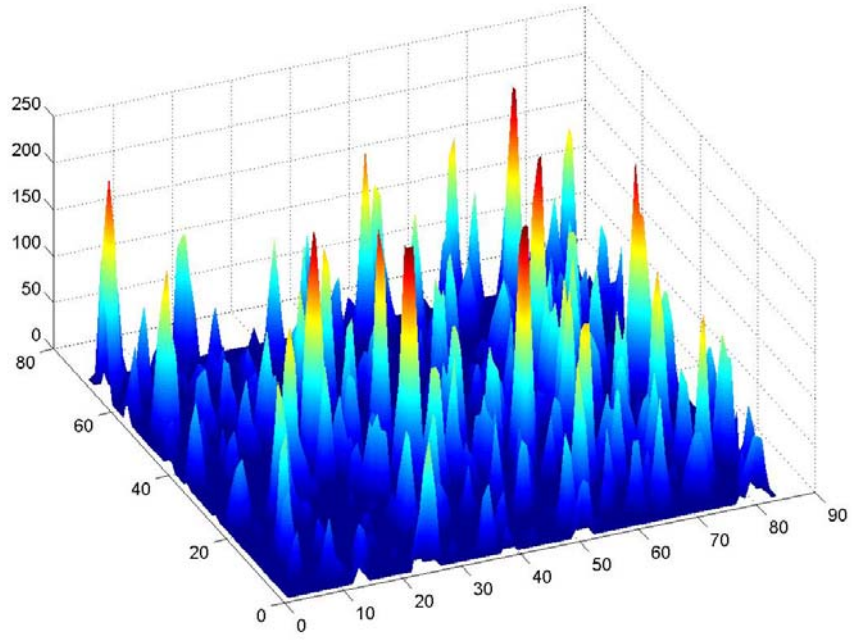

Figure 3.4 Three dimensional intensity image of speckles.

Speckle patterns depending on different threshold can be obtained by setting several thresholds. Kragh [16] proposes a way to define the average area of a single speckle excursion as

$$\overline{A} = \frac{Speckle\ \ area\ \ above\ \ threshold}{Total\ \ number\ \ of\ \ speckle} = \frac{A_{total}}{\overline{N}} \tag{3.4}$$

Apparently, the total excursion area above the threshold should drop with the increase of the intensity threshold. But the total number of the speckle will decrease at the similar

rate with the increase of threshold only at high threshold. Thus, it is interesting to note that the average speckle area should decrease faster at low threshold value than that at high threshold.

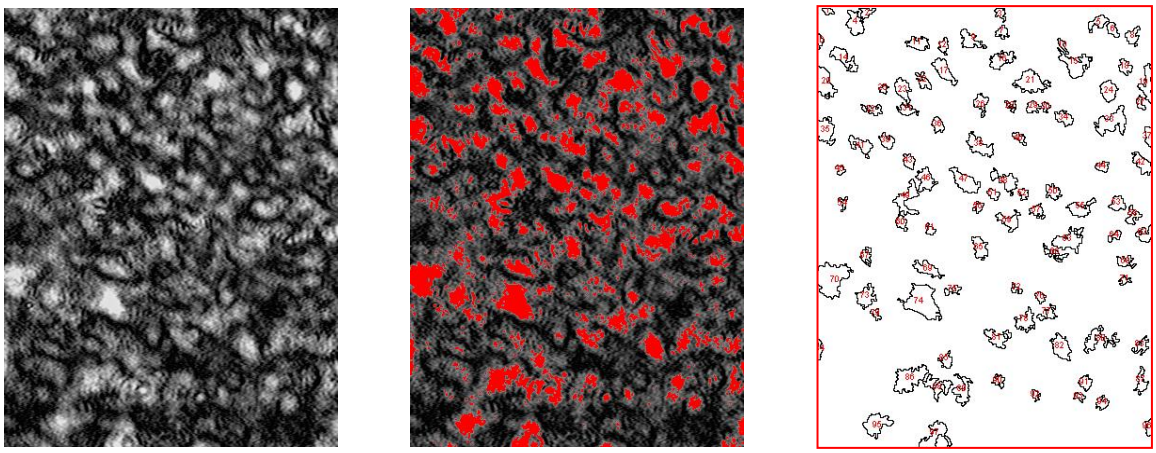

(a) **(b)** **(c)**

Figure 3.5 (a) Speckle direct image; (b) speckle image with intensity threshold of 136 (red area); (c) outline of the speckles with intensity above intensity threshold.

Figure 3.5 gives a demonstration on how the threshold affects the size of speckle pattern with specific threshold intensity 136 out of the maximum intensity of 255. As shown in figure (b), the total speckle areas with the intensity above threshold are singled out and highlighted by specific color (red) from a gray scale image in (a). Thus, the total speckle area above threshold can be counted by pixels. In order to count the total number of effective speckle, size range has to be set so that the bright spots with their size out of the size range are not counted. Here, all the speckles whose sizes are larger than 55 pixels square are counted and their patterns are shown in figure (c). Thus, the total effective

speckles are counted in this method. Then average speckle area can be calculated based on equation (3.4). Since the pixel size has been calibrated by 1mm quantum well window as 2.5 micron/pixel, the average speckle area can be calculated in millimeter.

Also, based on the theoretical prediction by Alexander [17], the average speckle area can be calculated by

$$\overline{A} = \frac{\pi \exp[M(I_t/\overline{I})]\Gamma[M, M(I_t/\overline{I})]}{l[M(I_t/\overline{I})]^{M-1}[2M(I_t/\overline{I}) - 2M + 1]} \tag{3.5}$$

where $\Gamma(M, MI_t/\overline{I}) = \int_{MI_t/\overline{I}}^{\infty} \exp(-t)t^{M-1}dt$ is the incomplete gamma function. Here M is the shaping constant which can be calculated by the mean ($\overline{I}$) and the variance (σ_I^2) of the intensity variation as

$$M = (\overline{I})^2/\sigma_I^2 \qquad \text{and} \qquad \sigma_I^2 = \overline{(I^2)} - (\overline{I})^2 \tag{3.6}$$

And l can be represented by the second moments of the normalized power spectral density of the field, l_{xx} and l_{yy}, by $l=(l_{xx}l_{yy})^{1/2}$, Where l_{xx} and l_{yy} correspond to the curvature of the normalized autocorrelation function alone horizontal and vertical directions.

Shaping constant M is an important factor for speckle intensity statistics of a speckle image. If the object surface is random and the roughness is on the scale of the radiation wavelength, the phase of the scattered signal should be almost uniformly distributed between $-\pi$ to π due to the randomness of the signal. Then there are a lot of independent phase and individual polarization in the scattered wavelets whose intensity distribution should follow the circular complex Gaussian statistics [18]. And each individual polarization follows a negative exponential statistics in its intensity

distribution and contribute 1 on the shaping constant. As we known, the unpolarized condition can always be treated as a case of two independent polarizations. Thus, the unpolarized condition will yield to independent negative exponential distribution, which leads to a total shaping constant of 2. This is the typical case for the direct speckle image by OCI. But for the holographic speckle image, the PRQW works as coherence filter, blocking the incoherent background, therefore only one polarization which is in the direction parallel with the polarization of reference beam survives. The shaping constant for this case should be 1.

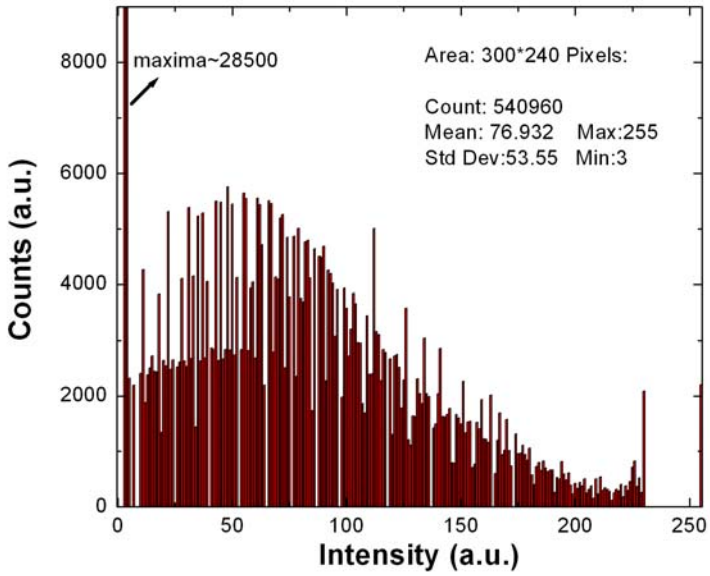

Figure 3.6 The histogram of direct speckle image.

In order to calculate the shaping constant of the speckle image shown in figure 3.5(a), the histogram of the image is calculated and the result is shown in figure 3.6. As presented by the histogram, the average intensity of the image is 76.932 and the standard

deviation to the average is 53.55. Based on equation 6, the shaping constant of direct speckle image is calculated by $(76.932/53.55)^2 = 2.064$.

Furthermore, based on the normalized autocorrelation functions shown in figure 3.3, the second moments of the normalized power spectral density l_{xx} and l_{yy} can be calculated by using parabolic fits of the autocorrelation function shown in figure 3.7. The peak curvature of the autocorrelation curve is approximately equal to twice of the fitting parameter of the quadratic term. The accuracy of this method really depends on the sampling density. A sampling density of 10 samples/speckle results in an error of less than 2% in this project.

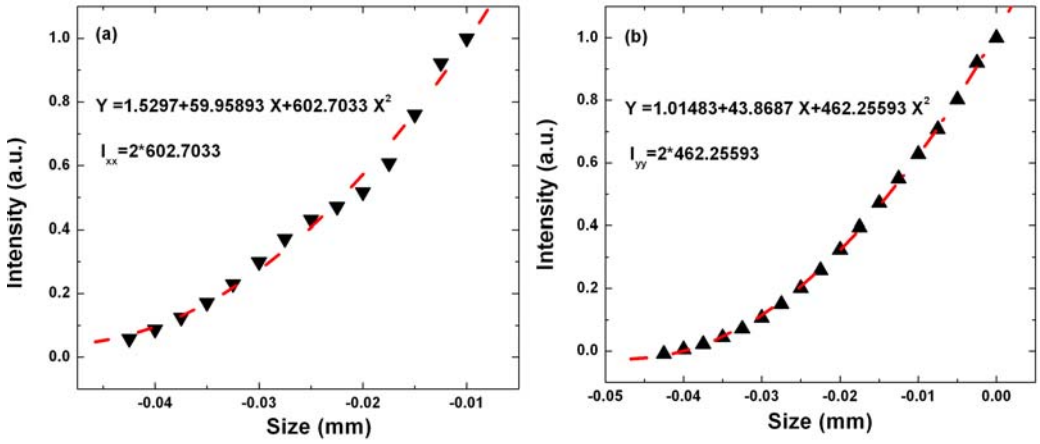

Figure 3.7 Parabolic fitting of the normalized autocorrelation functions for (a) horizontal and (b) vertical directions.

To systematically investigate speckle imaging we recorded two kinds of speckle patterns at the device location: direct speckle images and holographic speckle images.

Direct speckle images are acquired by blocking the reference beam in the interferometer, as shown in Figure 3.2. The sharp edge of the speckle image originates from the 1 mm window of the PRQW device. Average speckle sizes along horizontal direction and vertical direction of the image are calculated according to the autocovariance function, as shown in figure 3.3.

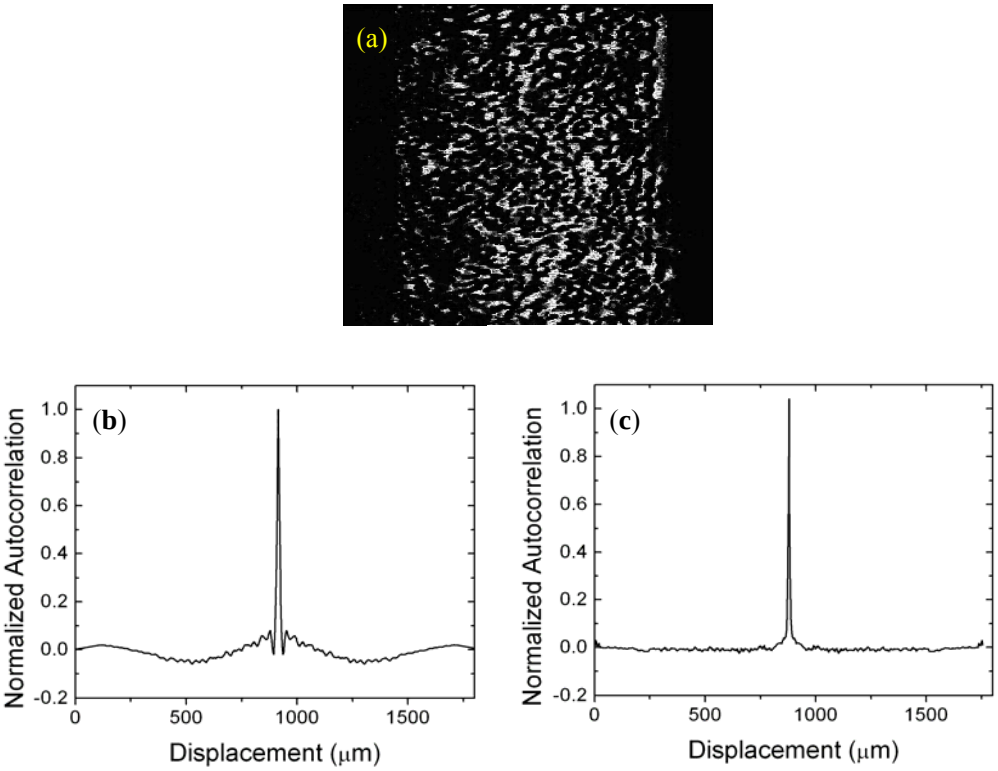

Figure 3.8 (a) Holographic speckles image, (b) average speckle size along horizontal direction, (c) average speckle size along vertical direction.

Holographic speckle images (figure 3.8(a)) are reconstructed by using a probe beam in a non-degenerate four-wave mixing. The baseline variation in figure 3.8(b) is due to the autocorrelation of the device window. The baseline variation is small in figure 3.8(b) since the device window is larger than the beam size in the vertical direction. As shown in figure 3.8, the holographic speckle has a difference size and intensity distribution compared to the direct speckle image.

Since the speckle is modified by the holographic process in the PRQW, the statistics of the speckle is related to the intensity level of the probe beam and the intensity ratio between the signal and the reference. To avoid the intensity issue we use a threshold or clipped method to analyze the intensity statistics of the speckle [17, 19, 20]. The histogram of the speckle image gives the intensity range of the image. Within this intensity range, a series of specific threshold values are selected. The total bright pixels with their intensity above the threshold are counted. The average speckle area of the clipped speckle is calculated by dividing the pixel number of the speckle above the threshold level to the total pixel number. The result indicates that the average speckle area is decreased with the increase of the intensity threshold, as shown in figure 3.9(a) and (b).

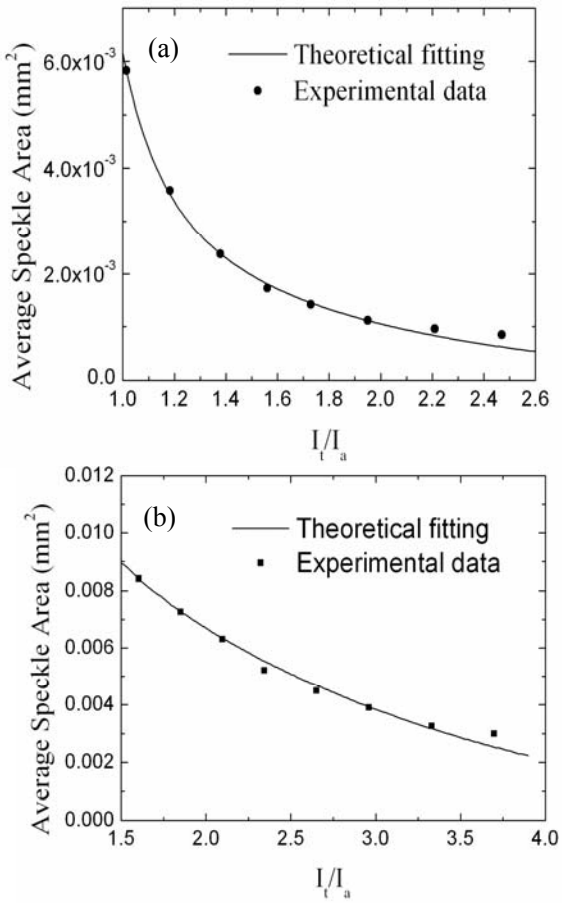

Figure 3.9 Comparison of the average speckle areas by theoretical and experimental values for (a) direct speckle image, and (b) holographic speckle image.

Based on the speckle theory [21], the statistics of the speckle can be understood by examining the gamma probability density function (PDF). The average speckle area that can be predicted theoretically is a function of three parameters [17, 19, 20]: (1) I_t/I_a where I_t is the preset threshold intensity and I_a is the mean intensity of the image, (2) the shaping constant of the gamma PDF, M, which is equal to $(I_a/\sigma_I)^2$ where σ_I is the variance of the intensity, and (3) the second moment of the normalized power spectral

density of the field, *l*, which is resulted from the peak curvature of the normalized autocovariance function. The histogram of the direct speckle image gives a mean intensity of 76.93 and a variance of the intensity variations of 53.55. The shaping constant of the direct speckle image is calculated to be 2.064. In our case, the surface roughness of the 15° diffuser is on the scale of the wavelength.

The intensity distribution of the direct speckle image comes from the sum of two unpolarized intensity distributions so that the shaping constant of the gamma PDF should be 2. This value is very close to the experimental result. Using experimental parameters of the holographic speckle the shaping constant is calculated to be 0.74. In general, a fully developed speckle gives a shaping constant of 1 in a negatively exponential gamma PDF. In holographic optical imaging, the speckle is modified by the reference that is coherent to the signal. Further contrast modification of the speckle comes from the nonlinear response of the holographic grating to the interference fringes, the intensity level of the probe beam, and the dynamic range of the photorefractive effect. Based on experimental parameters from both speckle images, theoretical calculations based on the gamma PDF give a good consistency to the experimental results, as shown in figure 3.9(a) and (b). A matlab program (appendix III) is used for this fitting.

3.4 Well-controlled Speckles

In order to study the speckle effect on holographic OCI, speckle generation should be well controlled so that proper parameters of the speckle can be selected. Speckle size is one of the important properties of speckle and we find two ways to effectively change the average speckle size of the speckles. Diffusers with different diffuse angles will generate speckles with variable sizes. Also, speckle size is varied in a small range when the diameter of the incident signal beam is changed. Both methods are used or combined to generate speckle with its size varying in a small range.

3.4.1 Control with diffuse angle

As shown in figure 3.10, speckle patterns were generated by four light shape diffusers (10°, 15°, 20°, and 25°) placed at the sample plane of the imaging system using the He-Ne laser. Images were collected by the CCD camera while the reference beam was blocked. It is apparent that the sizes of the speckle in these four images are different. The average size decreases when increasing the diffuse angle. In order to prove the estimation, average speckle sizes along horizontal direction of the speckle images, which were generated by various diffusers, were calculated after the imaging acquisition. The average speckle size of each image is calculated by using its autocovariance function. As shown in figure 3.11, the results indicate that the average speckle sizes decrease with the increasing of the diffuse angle for different diffusers.

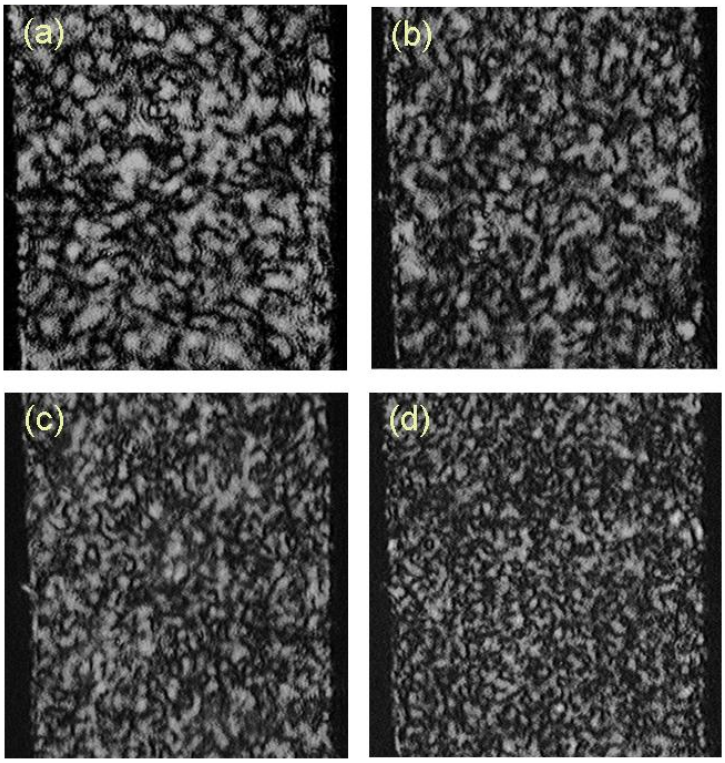

Figure 3.10 Speckle images for different diffusers: (a) 10 degree; (b) 15 degree; (c) 20 degree; (d) 25 degree.

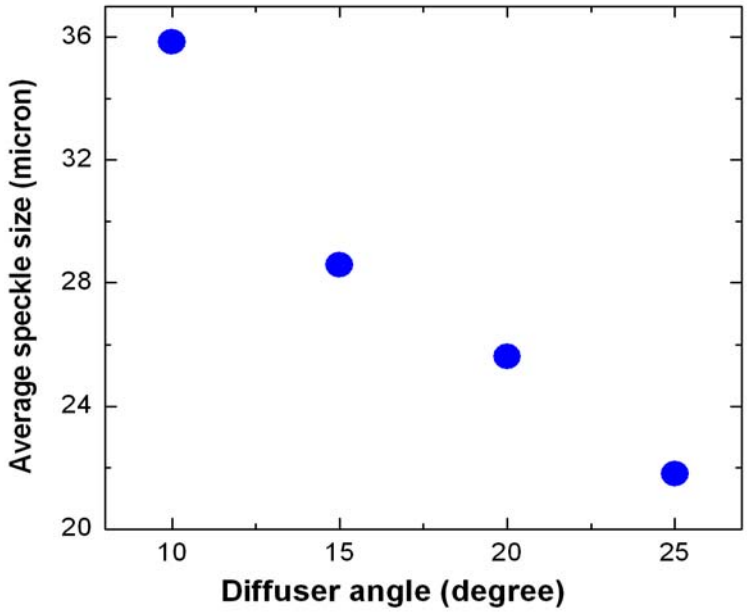

Figure 3.11 Speckle sizes versus the diffuser angles.

3.4.2 Control with the diameter of the signal beam

In order to generate speckle with different sizes by playing with the incident diameter of the signal beam, the system need to be revised. Two main changes had been made based on the typical OCI image system. Firstly, the main beam was expanded up to around 1 cm in diameter so that the aperture placed in signal arm can change the incident beam size in a small range. Secondly, the signal arm was changed from reflection geometry to transmission geometry. Although the diffuser can work under both geometries, the aperture will change the diameter of the incident beam as well as collecting angle of the scattered beam in the reflection geometry. The change in collecting cone angle affects the speckle size of the image too, which make the analysis complicated. Thus, transmission geometry was employed in our revised system.

Figure 3.12 presents the revised image system. A circular iris with changeable aperture sits before the diffuser to control the diameter of the incident beam in signal arm. 4F system is used to image the speckle into the PRQW. Diffuser works as the rough surface to generate speckles by transmission geometry. Photo refractive quantum well (PRQW) with 1mm window is used to calibrate the calculated average speckle size. Conventional monochromatic CCD camera is used to collect the images of speckles.

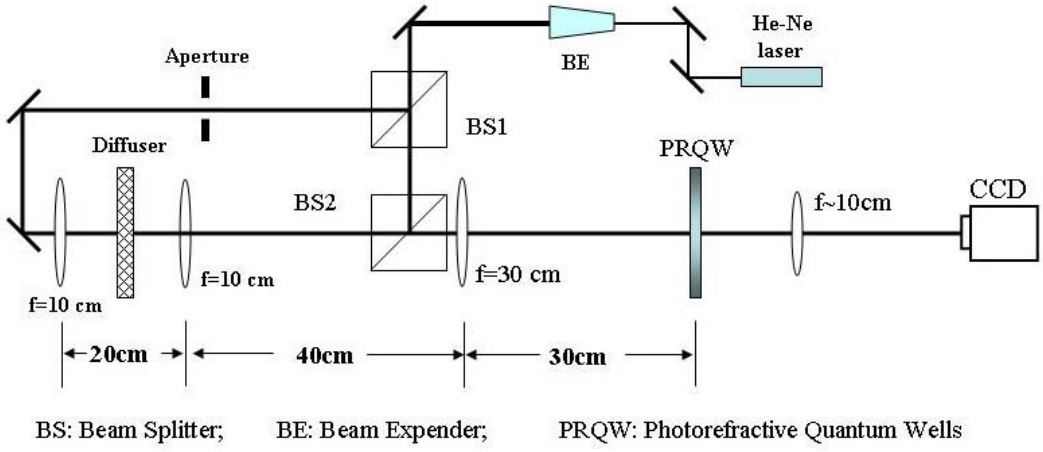

Figure 3.12 Image system used to generate speckle with different sizes by changing signal beam diameter.

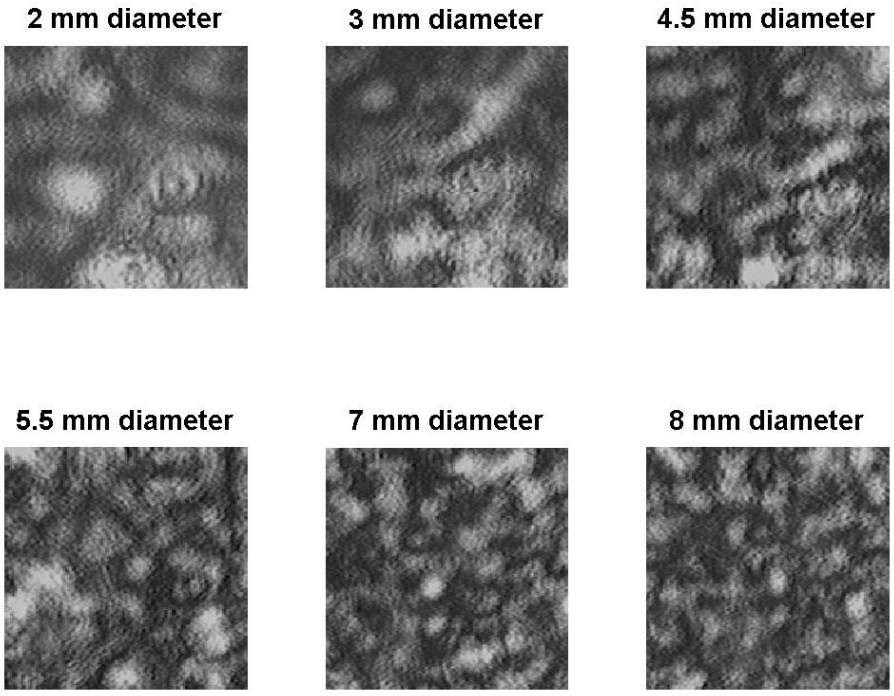

Figure 3.13 Speckle images for different diameters of the aperture.

The collected speckle images correspond to different aperture diameters are shown in figure 3.13. By using Matlab program, average speckle sizes along horizontal direction and vertical direction of the image are calculated. As shown in figure 3.14, the results indicate that the average speckle size decrease with the increase of aperture diameter.

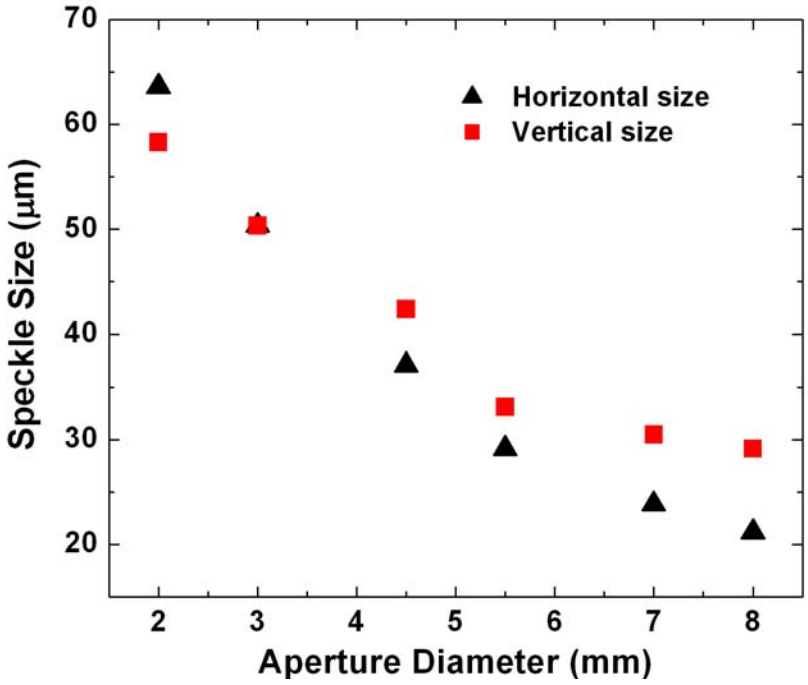

Figure 3.14 Speckle size versus diameter of the aperture.

3.5 Speckle Mechanism in Holographic OCI

Holographic OCI has emerged as a powerful tool to noninvasively image inside of the tumor spheroid at high speed [7, 10]. Speckles, which are the inherent results of coherence property of the coherent light, degrade the effective spatial resolution of the system and conceal subtle structure information of the objects in OCI. Thus, speckle

reduction becomes an important topic to improve the image quality and signal to noise ratio, especially for coherent domain image system such as OCT [22, 23]. Several techniques [24-26] applied to the image system to reduce the speckle effect.

In a holographic optical imaging system the FWM signal is used for imaging the object, and FWM efficiency is a function of the fringe spacing. Since interference fringes are involved in the formation of the holographic speckle, the FWM efficiency is also a function of the speckle size. On the other hand, FWM can determine how the speckle is imaged through the photorefractive effect. Here we demonstrate this influence by examining the FWM efficiency as a function of the fringe spacing and the speckle size.

The speckle size of the direct speckle image is calculated according to the autocovariance function as discussed at the beginning of this chapter. The fringe spacing can be calculated with the crossing angle between the signal and the reference and the wavelength. In PRQW the third-order optical nonlinearity is based on the Franz-Keldysh excitonic electroabsorption when an electric field is applied to the PRQW device in transverse-field geometry. The periodic intensity modulation introduces two gratings, absorption grating and refractive index grating with photorefractive phase shifts in the PRQW. The diffraction efficiency can be described by using these two gratings. The photorefractive gratings diffract the probe beam and the holograms are reconstructed by using the non-degenerate FWM in the PRQW. Thus, it must be pointed out that the gratings or fringes in the PRQW plays an important role, which not only decides the

direction of the diffracted signal, but also affects the signal intensity and transverse resolution of the OCI system.

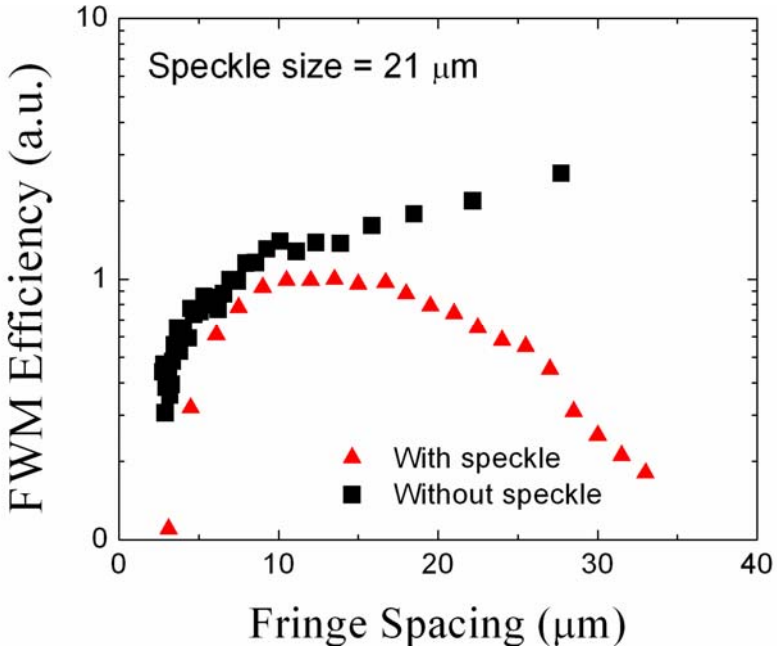

Figure 3.15 FWM signal as a function of fringe spacing.

FWM signals are collected by using a lock-in amplifier while the probe beam is chopped. The first-order diffraction of the probe beam is recorded by a photodiode and the zeroth-order is blocked by a rectangular aperture. The FWM efficiency as a function of the fringe spacing is shown in figure 3.15. Under a uniform illumination, the FWM efficiency decreases with the decrease of the fringe spacing, and then drops off rapidly at the fringe spacing below 5 μm. For the speckle imaging, the maximum FWM efficiency occurs at the fringe spacing about half size of the speckle.

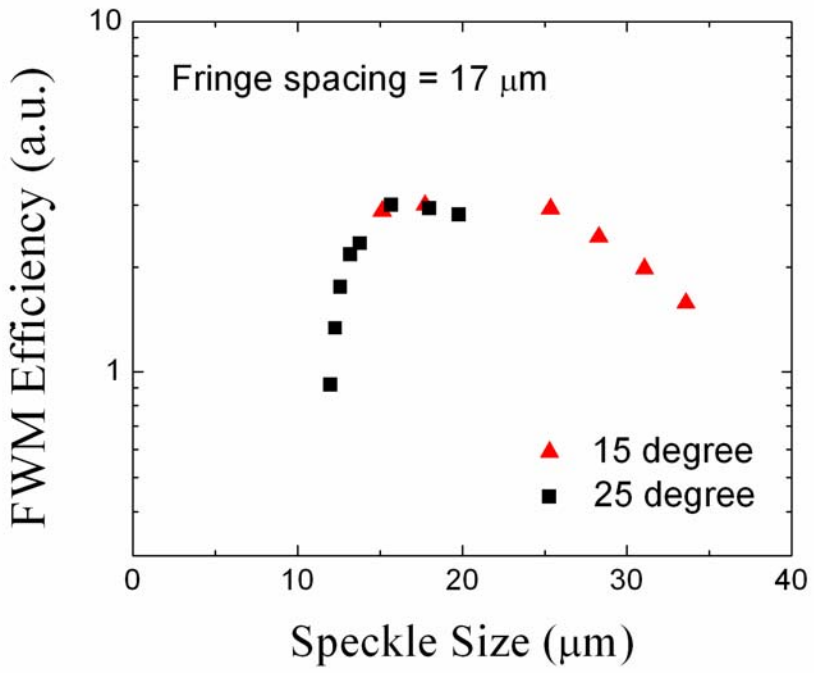

Figure 3.16 FWM signal as a function of speckle size.

Relationship between the FWM efficiency and the speckle size is shown in figure 3.16 at a fringe spacing of 17 μm. Variable speckle sizes are achieved by changing the aperture size of the 15° and 25° diffusers. In figure 3.16, the FWM efficiency decreases sharply when the speckle size is smaller than the fringe spacing. For the 15° diffuser, the FWM efficiency shows flat dependence as a function of speckle size near the fringe spacing, and then decreases slowly when the speckle size is above 25 μm.

The dependence of FWM efficiency as a function of the fringe spacing has been described by the transport effect of the photocarriers in the PRQW [27]. Additional FWM efficiency decrease in the speckle field when the speckle size is smaller than the fringe

spacing can be understood by the phase characteristics of the speckle and the coherence of holography. In this case, no interference fringe can be formed in the holographic medium due to the random phase of the speckle. If the size of speckle is much larger than the fringe spacing, the effect of the speckle on the fringes will cause shifting and bending by a random length due to the random phase of the speckle. Therefore the FWM efficiency decreases as the speckle size increases.

Based on the relationship among FWM signal, fringe spacing and speckle size, the speckles can be selectively rejected by choosing proper fringe spacing. Fringe spacing can be easily changed by tuning the angle between writing beams. Small fringe spacing may emphasis more on these speckles with size in the size range of fringe. But speckles with size smaller than fringe spacing will be effectively degraded. Therefore, to some extent, speckle may be reduced by playing with fringe spacing.

3.6 Conclusions

In Conclusion, we have described two statistical ways to evaluate the average speckle size of a speckle image. These two methods may have different application for the study of speckle property. Average speckle size in one dimension can be easily calculated by autocorrelation method. And two dimension statistical information of the average area of speckle can be measured by setting an intensity threshold. The relationship between the average speckle areas and corresponding intensity thresholds is

studied for both direct speckle image and holographic speckle image by optical coherence imaging. Although the decay constants for these two cases are different, both experimental results give a good consistence with the theoretic prediction. In practice, autocorrelation method is more popular since one dimension statistics is sometimes gives enough information to evaluate these grainy-texture patterns.

Besides, by employing diffusers with different diffuse angle and changing the incident beam size in signal arm, we generate speckles with different speckle sizes. These well controlled speckles are used in optical coherence imaging to study the speckle effect on the diffraction efficiency. The relationship among the speckle size, the fringe spacing and the four-wave mixing efficiency are systematically studied. Our study indicates that four-wave mixing efficiency drops sharply when the speckle size become smaller than the fringe spacing and decreases slowly when the speckle size is larger than the fringe spacing. Thus, the contribution of speckle to the diffraction signal or holographic image degrades sharply when the speckle size becomes smaller than the fringe spacing. This result can be used to selectively filter some speckle effects in holographic optical coherence imaging by choosing proper fringe spacing.

BIBLIOGRAPHY

1. I. Lahiri, L. Pyrak-Nolte, D. D. Nolte, M. Melloch, R. Kruger, G. Bacher, and M. Klein, "Laser-based ultrasound detection using photorefractive quantum wells," Appl. Phys. Lett. **73**, 1041-1043 (1998).

2. T. Shimura, F. Grappin, P. Delaye, S. Iwamoto, Y. Arakawa, K. Kuroda, and G. Roosen, "Simultaneous determination of the index and absorption gratings in multiple quantum well photorefractive devices designed for laser ultrasonic sensor," Opt. Commun. **242**, 7-12 (2004).

3. P. Yu, L. Peng, D. D. Nolte, and M. R. Melloch, "Ultrasound detection through turbid media," Opt. Lett. **28**, 819-821 (2003).

4. M. Gross, F. Ramaz, B. Forget, M. Atlan, A. Boccara, P. Delaye, and G. Roosen, "Theoretical description of the photorefractive detection of the ultrasound modulated photons in scattering media," Opt. Express **13**, 7097-7112 (2005).

5. L. Peng, P. Yu, M. R. Melloch, and D. D. Nolte, "High speed adaptive interferometer for optical coherence-domain reflectometry through turbid media," Opt. Lett. **28**, 396-398 (2003).

6. L. Peng, P. Yu, M. R. Melloch, and D. D. Nolte, "Adaptive Interferometer for Optical Coherence-Domain Reflectometry," J. Opt. Soc. Am. B **21**, 1953-1963 (2004).

7. P. Yu, M. Mustata, J. J. Turek, P. M. W. French, M. R. Melloch, and D. D. Nolte, "Holographic optical coherence imaging of tumor spheroids," Appl. Phys. Lett. **83**, 575-577 (2003).

8. R. Jones, N. P. Barry, S. C. W. Hyde, P. M. W. French, K. M. Kwolek, D. D. Nolte, and M. R. Melloch, "Direct-to-Video holographic readout in quantum wells for 3-D imaging through turbid media," Opt. Lett. **23**, 103-105 (1998).

9. M. Tziraki, R. Jones, P. French, D. Nolte, and M. Melloch, "Short-coherence photorefractive holography in multiple-quantum-well devices using light-emitting diodes," Appl. Phys. Lett. **75**, 363-365 (1999).

10. P. Yu, M. Mustata, L. Peng, J. J. Turek, M. R. Melloch, P. M. W. French, and D. D. Nolte, "Holographic optical coherence imaging of rat osteogenic sarcoma tumor spheroids," Appl. Opt. **43**, 4862-4873 (2004).

11. P. Yu, L. Peng, M. Mustata, J. J. Turek, M. R. Melloch, and D. D. Nolte, "Time-dependent speckle in holographic optical coherence imaging and the state of health of tumor tissue," Opt. Lett. **29**, 68-70 (2004).

12. Haibo Lin, and Ping Yu, "Speckle Mechanism in Holographic Optical Imaging," Opt. Express **15**, 16322-16327 (2007).

13. Newport Diffuser, http://www.newport.com/Optics/Filters%20and%20Attenuators/1/3561/product.aspx .

14. J.W.Goodman, *Statistical Properties of Laser Speckle Patterns, in Laser speckle and related phenomena* (Springer-Verlag, New York, 1984).

15. Y. Piederrière, J. Le Meur, J. Cariou, J. Abgrall, and M. Blouch, "Particle aggregation monitoring by speckle size measurement; application to blood platelets aggregation," **12**, 4596-4601 (2004).

16. F. E. Kragh, "Excursion areas of intensity due to random optical waves," (University of Central Florida, Orlando, Fla.,, 1990).

17. Terri L. Alexander, "Average speckle size as a function of intensity threshold level: comparison of experimental measurements with theory," Appl. Opt. **33**, 8240-8250 (1994).

18. J.W. Goodman, *Statistical optics* (Wiley, New York, 1985).

19. A. D. Ducharme, G. D. Boreman, and D. R. Snyder, "Effects of intensity thresholding on the power spectrum of laser speckle," Appl. Opt. **33**, 2715 (1994).

20. A. D. Ducharme, G. D. Boreman, and S. S. Yang, "Elimination of threshold-induced distortion in the power spectrum of narrow-band laser speckle," Appl. Opt. **34**, 6538 (1995).

21. J. W. Goodman, *Speckle Phenomena in Optics, Theory and Applications* (Ben Roberts & Company, 2007).

22. Bashkansky, and Reintjes M., J., "Statistics and reduction of speckle in optical coherence tomography," Optics Letters **25**, 545-547 (2000).

23. D. L. Marks, T. S. Ralston, and S. A. Boppart, "Speckle reduction by I-divergence regularization in optical coherence tomography," Journal of the Optical Society of America a-Optics Image Science and Vision **22**, 2366-2371 (2005).

24. Desjardins, Vakoc A. E., Oh B. J., Motaghiannezam W. Y., Tearney S. M. R., and B. E. Bouma, "Angle-resolved Optical Coherence Tomography with sequential angular selectivity for speckle reduction," Optics Express **15**, 6200-6209 (2007).

25. A. E. Desjardins, B. J. Vakoc, G. J. Tearney, and B. E. Bouma, "Speckle reduction in OCT using massively-parallel detection and frequency-domain ranging," Optics Express **14**, 4736-4745 (2006).

26. J. Kim, D. T. iller, E. Kim, S. Oh, J. Oh, and T. E. Milner, "Optical coherence tomography speckle reduction by a partially spatially coherent source," Journal of Biomedical Optics **10** (2005).

27. D. D. Nolte, "Semi-insulating semiconductor heterostructures: Optoelectronic properties and applications," J. Appl. Phys. **1999**, 6259-6289 (1999).

Chapter 4

Statistics of Holographic Speckle in OCI

4.1 Introduction

Speckle is a common phenomenon for holographic OCI due to the use of a coherent light source. The speckle effect [1-5] and its statistics [6, 7] have been extensively studied in various Optical Coherence Tomography (OCT) techniques. Few works have been done about speckle effects in holographic OCI [8]. The speckle statistics for holographic OCI originates from a different model for OCT, since in OCI dynamic holograms are recorded and reconstructed in the holographic media through the photorefractive effects. As a consequence, the speckle statistics are altered by photorefractive effects. Thus, the speckle theory for OCT cannot be directly applied in an OCI system.

In general, speckle from biological tissue consists of random patterns caused by the interference of single scattering and multiple scattering from small scatters such as the nucleus, mitochondria, and membranes with sizes and distances comparable to the source wavelength. Speckle provides useful information of optical scattering and concentration of these small scatters inside the tissue. Meanwhile, speckle also causes random noises to reduce the image quality of extended features of the tissue. To study the speckle

mechanism in holographic OCI, we have explored the relationship between the speckle size and fringe spacing, and its effect on the diffraction efficiency of four-wave mixing in a holographic system [9]. The selection of fringe spacing can be used to suppress the speckle in a specific size range. A moving grating was adapted in combination with a CCD camera to further average the random speckle. Although the statistical method was applied to determine the size of speckle in this work [9], detailed analysis of speckle statistics in holographic OCI have not yet been explored. It is not clear how the speckle statistics are modified by the photorefractive holography and how the speckle influences the image interpretation.

In this chapter, we present a new speckle statistics theory for holographic OCI. This theory provides a comprehensive and reasonable description of intensity feature of holographic speckle under both the small signal limit and large signal limit conditions. For both conditions, a unit intensity ratio between the stronger writing beam and probe beam can be used to optimize the diffraction intensity under the Joule heating limit.

4.2 Model for Speckle Imaging in Holographic OCI

The principle of holographic OCI is based on interferometric detection by using a holographic device to detect coherent waves. Similar to other coherence domain techniques, these coherent waves experience backward scattering from the structures inside the turbid medium and maintain coherence with the reference wave in the

interferometer. We will discuss coherence domain holography by using the coherent volume shown in Figure 4.1.

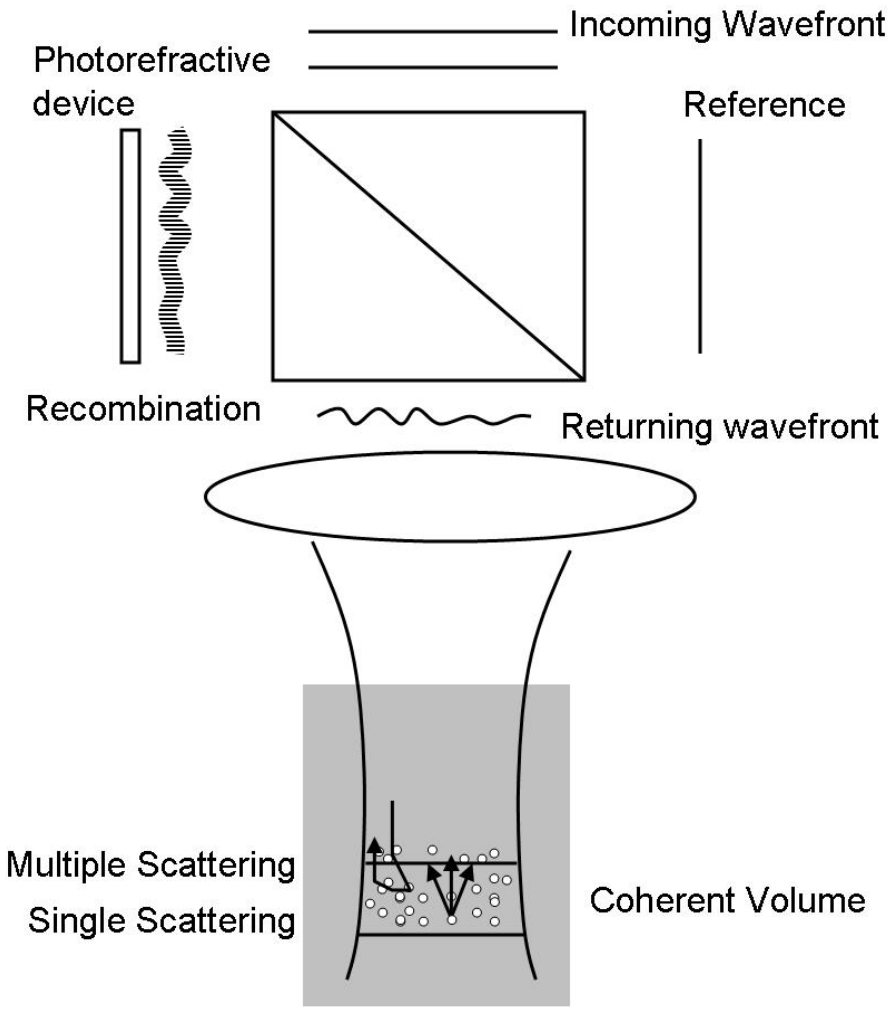

Figure 4.1 Model of coherence volume including single scattering and multiple scattering in holographic optical coherence imaging.

To simplify the process we assume that the scatters distribute uniformly inside the coherent volume. The coherence volume consists of two parts, (1) a single-scattering volume and (2) a multiple-scattering volume. Due to the coherent detection, the multiple-scattering volume should be at a short optical path location in the sample since the multiple scattered photon experiences a longer delay. The thickness of the single scattering volume is approximately equal to the cross-correlation of the signal and reference waves. The thickness of the multiple scattering volume can be estimated by using numerical methods, for example Monte Carlo simulations [10]. We suppose that there are many small scatters (with sizes and distances comparable to the wavelength) inside the coherence volume. Therefore, the speckle is a fully developed speckle [11].

Furthermore, we suppose the amplitude and phase of the speckle are independent of each other. This assumption requires the spatial coherence between the signal and reference. In practice, the hologram has a uniform distribution inside the coherent volume if the angle between the signal and reference is small. This means that the walk-off effect can be neglected and the effect of spatial coherence should not be considered in the holographic speckle.

Holographic OCI has several types, based on different photorefractive media, such as photorefractive multiple quantum wells (PRQW) [12-18], photorefractive crystals [19] and photorefractive polymers [20-22]. Among them, PRQW has shown promise in coherence domain biological imaging due to its high sensitivity and fast response. In

PRQW, dynamic holograms are recorded and reconstructed in an active semiconductor layer through four-wave mixing. The layer thickness is about 1 μm and the fringe spacing of holograms is typically about 20 μm along the active layer. Therefore, the diffraction in four-wave mixing is in the Raman-Nath regime. Historically, photorefractivity has been applied to applications of detecting or removing speckle for many years, for example speckle photography and speckle velocimetry [23-25]. Bulk crystals and CW laser sources are used in these applications. In a low coherence holographic OCI based on PRQW, the full-frame speckle statistics can be analyzed by using the holographic speckle theory in the transverse direction. The speckle statistics perpendicular to the active layer can be approximately considered in a large speckle size limit if the speckle size is comparable to the round trip coherence length (about 10-30 μm) of the light source. As shown in the later section, the effect of speckle is a broadening of the longitudinal resolution, a phenomenon similar to the speckle analysis in OCT.

4.3 General Statistics Theory of Holographic Speckle

In this section we develop the general statistical theory of speckle patterns acquired in holographic OCI. In OCI, the speckle is formed by the interference between the random phase signal and the fixed phase reference. Only coherent components are recorded at the same path length between the signal and reference. Holographic processes modify the speckle statistics through the photorefractive effect in the PRQW. In our research, a

non-degenerate FWM is used to differentiate the coherent component and incoherent background, which is called spatial heterodyne detection. In this section we begin with the statistics of fully developed speckle. After the development of general theory, we examine the speckle statistics in various conditions.

4.3.1 Four wave mixing intensity

The coherent components are recorded using the photorefractive effect based on nonlinear optics of the photorefractive material. The photorefractive process in a PRQW is based on the quadratic electroabsorption effect of excitons [23]. In a transverse geometry of a PRQW, an electric field is applied along the active layer of the device to produce the quantum-confined Stark effect. The diffraction intensity in the non-degenerate FWM can be written as

$$I_d = m^2 \eta(\omega_0) I_P \exp(-\alpha L / \cos\theta') \tag{4.1}$$

where $\eta(\omega_0)$ is the diffraction efficiency at the peak frequency ω_0, α is the absorption constant at the electric field E_0, I_P is the intensity of probe beam, L is the thickness of active layer in the PRQW device, and θ is the angle of probe beam inside the device. The modulation index is a function of the reference intensity I_R, signal intensity I_S, and probe intensity I_P,

$$m = \frac{2\sqrt{I_R I_S}}{I_R + I_S + I_P} \tag{4.2}$$

Using equation (4.2), the non-degenerate FWM diffraction intensity can be re-written as a function of intensities of the writing beams and probe beam,

$$I_d = \frac{A I_R I_S I_P}{(I_R + I_S + I_P)^2} \tag{4.3}$$

A is equal to $4\eta(\omega_0)exp(-\alpha L/cos\theta')$. It is clear from the equation that the three beam intensities I_R, I_S and I_P have the same impact on the diffraction intensity I_d. Therefore, similar analysis is applied to different cases to be given in later discussion.

4.3.2 Statistics of fully developed speckle

In order to analyze the statistical distribution of holographic speckle, it is necessary to convert the statistical variable I_S to I_d since the statistics of holographic speckle is described from the speckle pattern acquired in the hologram. A critical relationship will help us complete this conversion. Suppose that a random variable v is related with another random variable u through a monotonic relation as $v=f(u)$. Then, based on fundamental probability theory [26], the probability density function PDF $p(v)$ can be found from $p(u)$ through

$$p(v) = p(f^{-1}(v))\left|\frac{du}{dv}\right| \tag{4.4}$$

A typical application of this relationship in optical problems is the conversion between intensity and amplitude of the radiation field. If v represents the intensity I and u represent the amplitude of the field A, then the relation between them is

$$I = A^2 = f(A) \tag{4.5}$$

According to conversion (4.4), the intensity PDF can be written as a function of PDF amplitude by [27]

$$P_I(I) = P_A(\sqrt{I})\left|\frac{dA}{dI}\right| = \frac{1}{2\sqrt{I}} P_A(\sqrt{I}) \tag{4.6}$$

In our case, the PDF of the signal beam (I_s) should be converted to the PDF of the diffraction signal (I_d). Then based on conversion (4.4), the formula that can be used for this conversion is presented as [11]

$$P(I_d) = \frac{P[f^{-1}(I_d)]}{\left|df / dI_S\right|} \tag{4.7}$$

Although the speckle pattern comes from a sum of random walks from the signal and a constant phasor from the reference, the constant phasor angle will not change the statistics of the speckle, which means that the phase angle between the signal and reference does not need to be considered as a variable. This is true if the statistics of the amplitude and phase are independent each other. Similar analysis has been done in OCT. For example, Karamata et al. [28] reported that these two conditions are considered in the statistical theory for OCT cases.

When the number of random walks is large enough, the distribution of the sum for those random walks follows the Raleigh distribution and the phase of the result is uniformly distributed over ($-\pi$, π). This kind of speckle distribution can be treated as fully developed speckle. For a finite but large number of speckles, fully developed

speckle is a good approximation to simplify the problem. The PDF of amplitude of fully developed speckles can be written as [27]

$$p_A(A) = \frac{A}{\sigma^2}\exp(-\frac{A^2}{2\sigma^2}) \tag{4.8}$$

for $A \geq 0$. According to equation (4.6), the intensity PDF distribution obeys a negative exponential probability density as

$$P_I(I) = \frac{1}{2\sigma^2}\exp(-\frac{I}{2\sigma^2}) \tag{4.9}$$

The moments of the distribution of fully developed speckle pattern can be calculated by direct integration with a result of

$$\overline{I^q} = (2\sigma^2)^q q! \tag{4.10}$$

Then the second moment, variance and standard deviation of the intensity for the fully developed speckle are then given by

$$\overline{I^2} = 2\bar{I}^2, \quad \sigma_I^2 = \bar{I}^2, \quad \sigma_I = \bar{I} \tag{4.11}$$

respectively. The intensity PDF can be rewritten as:

$$P(I_S) = \frac{1}{\sigma_I}\exp(-\frac{I_S}{\sigma_I}) \tag{4.12}$$

Two factors are important to study speckle: the contrast and the signal-to-noise-ratio. Contrast of the speckle pattern represents the magnitude of the intensity variation in a speckle image compared with the average intensity. Signal-to-noise-ratio (SNR) is the reciprocal of contrast which is the ratio of the average intensity and the fluctuation of the intensity. The contrast and signal to noise ratio of speckle pattern are defined

$$C = \frac{\sigma_I}{\bar{I}}, \quad S/N = 1/C = \bar{I}/\sigma_I \tag{4.13}$$

respectively. For fully developed speckle, equation (4.13) indicates that both the contrast and SNR are equal to 1. Thus, the magnitude of the intensity fluctuations is of the same magnitude of the average, making this kind of speckle very noisy indeed.

4.3.3 General statistics theory for holographic speckle

In order to analyze the general statistical distribution of holographic speckle, it is necessary to convert the statistical variable I_S to I_d since the statistics of holographic speckle is analyzed in the holographic speckle pattern reconstructed in the CCD camera. The formula for this transformation is given by equation (4.7). Here we only use a single intensity variable in the conversion. As we mentioned in previous section, the constant phasor angle will not change the statistics of the speckle. The phase angle between the signal and reference does not need to be considered as a variable. Similar analysis has been done in OCT where the signals in the detector are proportional to the interference term and the speckle statistics is a Ricon PDF. For example, Karamata et al. [10] has reported that the statistics of speckle are the same even when the phase angle is considered as an additional variable.

In order to reach the general PDF expression of speckle intensity in OCI, it is convenient from both mathematical point of view and from the point of physical transparency to introduce two dimensionless parameters

$$x = \frac{I_S}{I_R + I_P} \quad \text{and} \quad y = I_d \frac{4(I_R + I_P)}{A I_R I_P} \tag{4.14}$$

so that the transformation equation (4.3) can be rewritten as

$$y(x) = \frac{4x}{(1+x)^2} \tag{4.15}$$

It is very important to mention several properties of this mapping function that will inform our study below. For a physically relevant range of $0 < x < \infty$, the function leads to $0 < y < 1$; The function $y(x)$ is monotonically increasing for $0 < x < 1$ and it is monotonically decreasing for $1 < x < \infty$; $y(x)$ is, thus, a two valued function; The mapping is singular around $y \sim 1$ because $dy(x)/dx\big|_{x=1} = 0$ and therefore, $dx(y)/dy\big|_{y=1} = \infty$.

For the two-valued function under consideration, one can write the sought PDF in the form

$$P(y) = \left[P[x(y)] \left| \frac{dx(y)}{dy} \right| \right]_{0 \le x(y) < 1} + \left[P[x(y)] \left| \frac{dx(y)}{dy} \right| \right]_{1 \le x(y) < \infty} \tag{4.16}$$

$x(y)$ can be readily found from equation (4.15)

$$x_{\pm}(y) = \left(\frac{2}{y} - 1 \right) \pm \frac{2}{y} \sqrt{1 - y} \tag{4.17}$$

The result is

$$P(y) = \frac{1}{s} e^{-\frac{x_-(y)}{s}} \times x'_-(y) - \frac{1}{s} e^{-\frac{x_+(y)}{s}} \times x'_+(y) \tag{4.18}$$

where $s = \frac{\sigma}{I_R + I_P}$ is the only parameter that determines the shape of the resulting PDF.

The function (4.18) has the following properties:

1. As expected, the function is positively defined and normalized to unity.

2. In the $s = \frac{\sigma}{I_R + I_P} < 1$ regime the function strongly resembles the negative exponential (Rayleigh) distribution. This physically corresponds to a weak signal regime, when $\langle I_S \rangle \equiv \sigma < I_R + I_P$. Here $\langle \ldots \rangle$ denotes a statistical average. Indeed, in this regime the signal dependence in the denominator of equation (4.3) can be neglected and the transformation is equivalent to simple scaling.

3. The opposite regime of strong signal where $s = \frac{\sigma}{I_R + I_P} > 1$ or $\langle I_S \rangle \equiv \sigma > I_R + I_P$, is a nontrivial one. Although it is tempting to omit the $I_R + I_P$ contribution compared to I_S in the denominator of equation (4.3), such treatment would be unjustifiable. This is because the negative exponential PDF equation (4.12) peaks at $I_S = 0$ regardless of $\langle I_S \rangle = \sigma$. Nonetheless, a useful approximation can still be obtained around a physically significant peak at small values of *y*, where we find

$$P(y) \approx \frac{1}{s} e^{-\frac{2}{s}\left(\frac{2}{y} - 1\right)} \frac{4}{y^2}, \tag{4.19}$$

Note that this is an approximation to the function $P(y)$ and, thus, should only be applied in its range of applicability *y<1*. It is not normalized in itself.

Before further discussion on the statistics of holographic speckle, one constraint

should be pointed out for the PRQW device. The combination of applied electric field and illumination creates a photocurrent inside the device. This photocurrent current induces Joule heat that may damage the device if its magnitude is too high. Under a specific applied voltage, this constraint limits the total intensity illuminated on the device to a maximum value, called the Joule heating limit. It will introduce several interesting phenomena which will be presented later.

4.4 Holography Imaging System

We use the same holographic OCI system shown in figure 2.9. A 790 nm super-luminescent light emitting diode with a wavelength bandwidth of 30 nm serves as a light source for an imaging Michelson interferometer. Dynamic holograms are recorded and reconstructed in a PRQW by using a non-degenerate FWM configuration. A CW laser diode acts as the probe beam with a wavelength of 834 nm that corresponds to the peak of the exciton absorption band. Speckle patterns are generated by a random-phase diffuser (Newport Cooperation) placed at the sample plane of the imaging system (single scattering), or by a turbid medium placed in front of a mirror (multiple scattering). In the imaging interferometer, a modified 4-F lens pair relays the image from the sample plane to the device plane with a magnification of 3. The fringe spacing is around 20 μm determined by the angle between the signal beam and reference beam and confirmed by the measurement from the direct image in a CCD (SONY, SPT-M124). After the

reconstruction, the hologram is imaged onto a cooled CCD camera (Photometric Cascade II, 80°C, 512 pixel × 512 pixel, 16 bit, EMCCD) by using a 10-cm lens. The magnification of the 10-cm lens is adjusted so that each speckle is recorded by at least a 3 × 3 pixel grid in the CCD camera.

The holographic speckle is recorded in two steps. First, the holographic image is recorded when the signal and reference are path-matched. Second, the reference delay is moved away from the path-match position so that the fringes disappear. Then, the background image is recorded. In these steps, the total intensity remains constant, so that the absorption of the device is not altered. The holographic speckle image is obtained by subtracting two images. This two-step process is important in holographic OCI since the zeroth-order of the probe beam contributes a background due to a self-diffraction of the probe beam from the device window-edges and macro-defects inside the window. Although this two-step acquisition is used in holographic OCI, the imaging speed is the same since the same background can be used for all images.

4.5 Holographic Speckle Statistics under Small Signal Limit

4.5.1 Small signal limit

In some applications, coherent signals are very weak. This is very common for imaging highly scattered samples, such as human skin. The case I_R and I_P both >> I_S is considered first. Under this condition, the signal beam can be ignored in the denominator of the

modulation function in comparison with the strong reference and probe intensities. The diffraction intensity can be written as

$$I_d = f(I_S) = A\frac{I_R I_S I_p}{(I_R + I_P)^2} \tag{4.20}$$

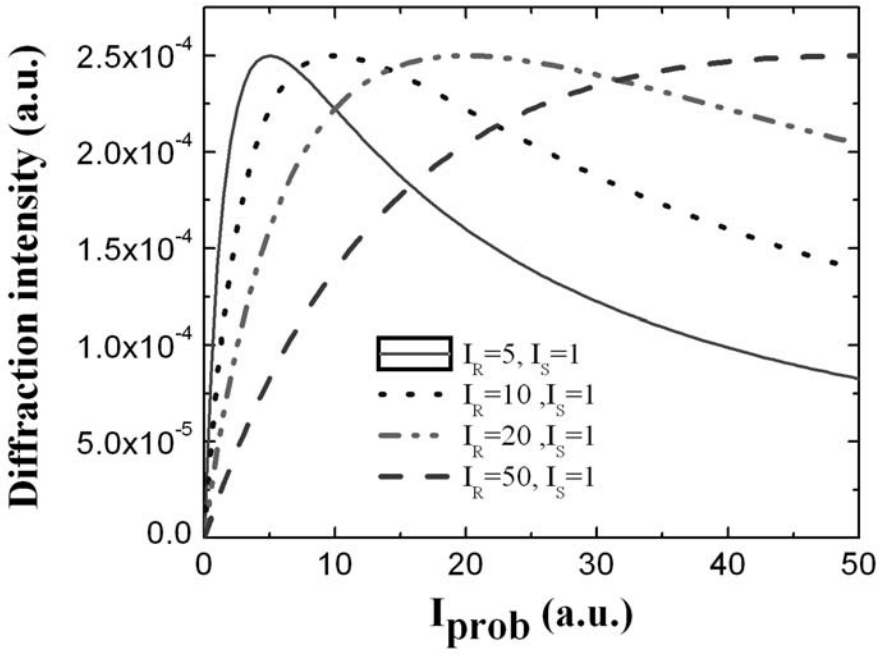

Figure 4.2 Diffraction intensity as a function of probe intensity in the small signal limit.

Figure 4.2 shows the calculated diffraction intensity as a function of I_P and I_R according to equation (4.20). In this calculation we suppose I_S = 1 and A = 10^{-3}. The different curves correspond to various reference intensities (I_R). To optimize the holograms, the reference intensity and probe intensity should be adjusted to allow the maximum intensity of diffraction. The maximum diffraction intensity is located at $I_P = I_R$.

The curve broadens as I_R increases. This means that the diffraction intensity is insensitive to I_P when both I_P and I_R are large enough. This result also indicates that we should let the probe beam intensity be equal to the reference beam intensity in order to achieve strong diffraction. On other hand, I_P should be kept as lower intensified as possible, since large I_P will introduce background noise in the diffraction due to the leakage from the transmitted beam.

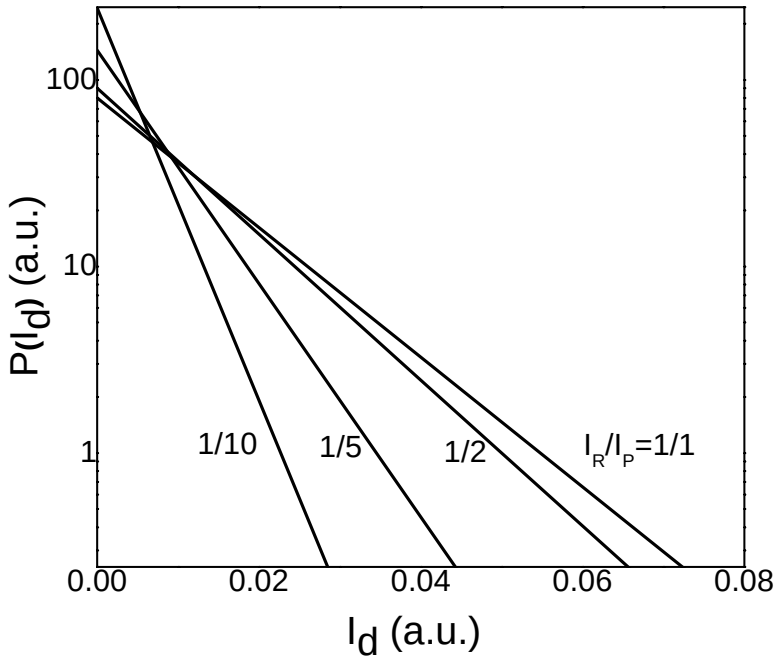

Figure 4.3 PDF simulation in small signal limit.

Under the small signal limit, according to equation (4.7) and (4.20), the speckle statistics of the holographic image can be written as

$$P(I_d) = \frac{1}{A\sigma_I}(2 + \frac{I_R}{I_P} + \frac{I_P}{I_R}) \exp[-(\frac{1}{A\sigma_I}(2 + \frac{I_R}{I_P} + \frac{I_P}{I_R})I_d)] \qquad (4.21)$$

This is a negative exponential function of diffraction intensity, except that the slope is a function of the ratio between the reference and pump intensities in a semi-logarithm plot as shown in figure 4.3. At $I_R = I_P$, where the diffraction intensity is the maximum, the slope is minimum. This corresponds to the best intensity distribution of speckle.

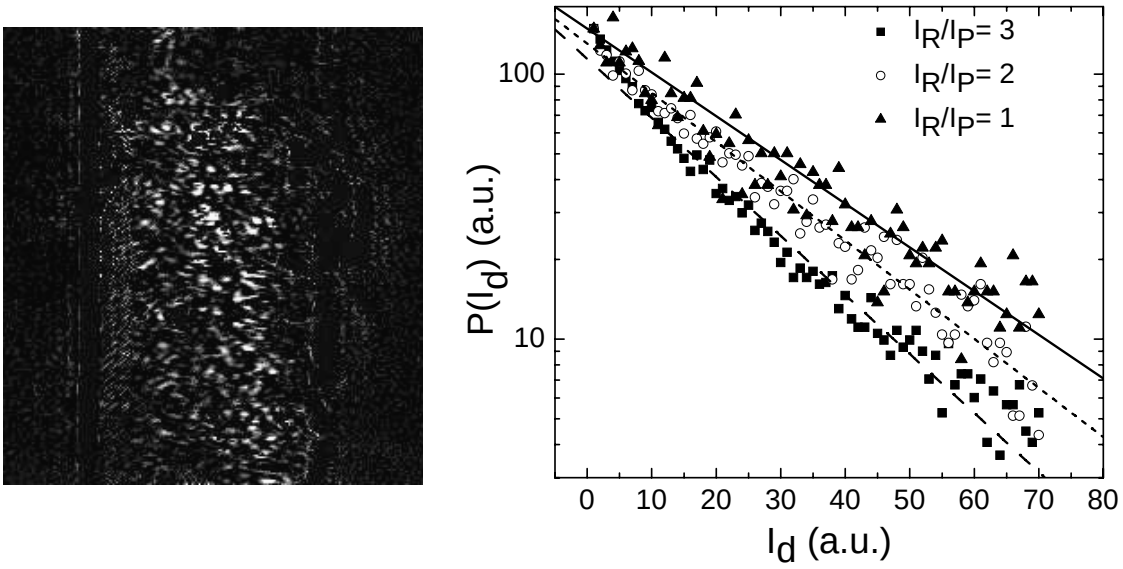

Figure 4.4 (a) Typical holographic speckle using a light shape diffuser. (b) experimental and calculated PDF of I_d for various intensity ratios in the small signal limit.

Figure 4.4(a) presents a typical holographic speckle and figure 4.4(b) shows the experimental data of PDF from holographic speckle for various ratios between the reference and probe intensities. The signal intensity is one tenth of the total intensity. The lines in figure 4.4 (b) are calculated the PDF according to equation (4.21). Here we see that the PDF of holographic speckle is a negative exponential function in the small signal limit.

4.5.2 Joule heating limit for small signal limit

When discussing the speckle statistics in holographic OCI, one constraint should be addressed [29]. For PRQW, the combination of illumination and applied electric field creates a photocurrent inside the device. This photocurrent produces Joule heat that may damage the device. The total intensity illuminated on the device should not exceed a maximum value, which is called the Joule heating intensity limit. If the total intensity is limited by Joule heat, we can assume that the total intensity $I_{Total} \approx I_R + I_P$ is constant. Although the Joule heating intensity is a device related parameter, a typical value is generally used to monitor the safety of the PRQW. For example, at 1 kV for a 1 mm device window, an intensity of 100 mW/cm^2 is a reasonable limit of total intensity. The diffraction intensity as a function of probe intensity is shown in figure 4.5. Similar results of diffraction intensity at the Joule heating limit have been observed in two-wave mixing of the PRQW for ultrasound detection through turbid medium, as it reported in reference [30]. Under the Joule heating limit, the PDF is

$$P(I_d) = \frac{4}{A\sigma_I}\exp(-\frac{4I_d}{A\sigma_I}) \tag{4.22}$$

It is clear that, for maximum diffraction at the Joule heating limit, the PDF is a negative exponential function of I_d without any relation to the total intensity.

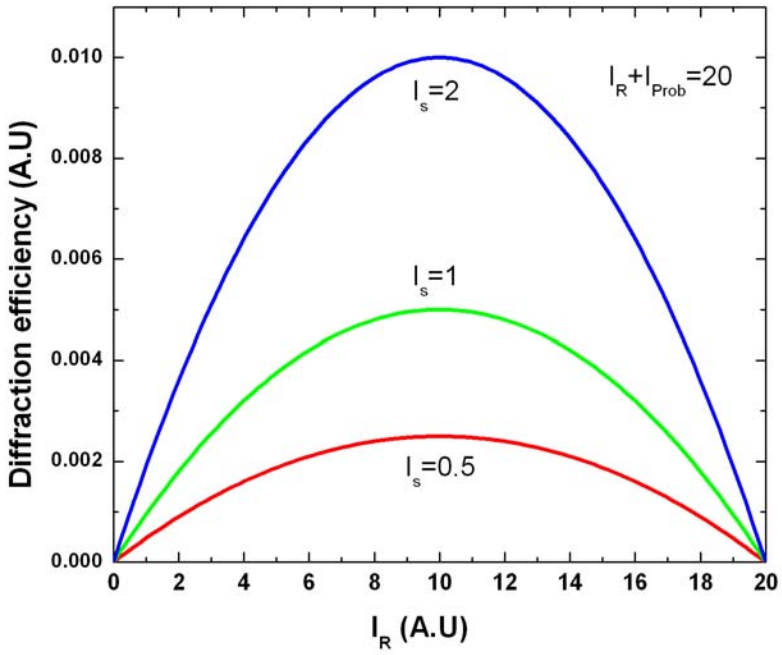

Figure 4.5 Diffraction intensity as a function of reference intensity in the Joule heating limit.

Although the signal intensity is small in this case, the statistics of the holographic speckle is still a negative exponential function of the intensity. However, this exponential function has a fast decay since the constant A is a small number due to low diffraction efficiencies (about 10^{-3} in general).

The holographic speckle image with intensity ratio of $I_R = I_P \sim 5I_S$ is collected by the OCI system. The experimental results as well as the theoretical prediction are plotted in figure 4.6. As the diffracted signal intensity increases, the PDF deviates from the negative exponential function. This phenomenon is confirmed experimentally and theoretically. The physics behind this is that the modulation index is no longer a linear function of the

signal intensity, which causes redistribution of the diffraction intensity. It is interesting to notice that the two parameters in equation (4.22) are the same, both equal to $4/A\sigma_I$. The fitting parameters indicate that those two values are very close to each other.

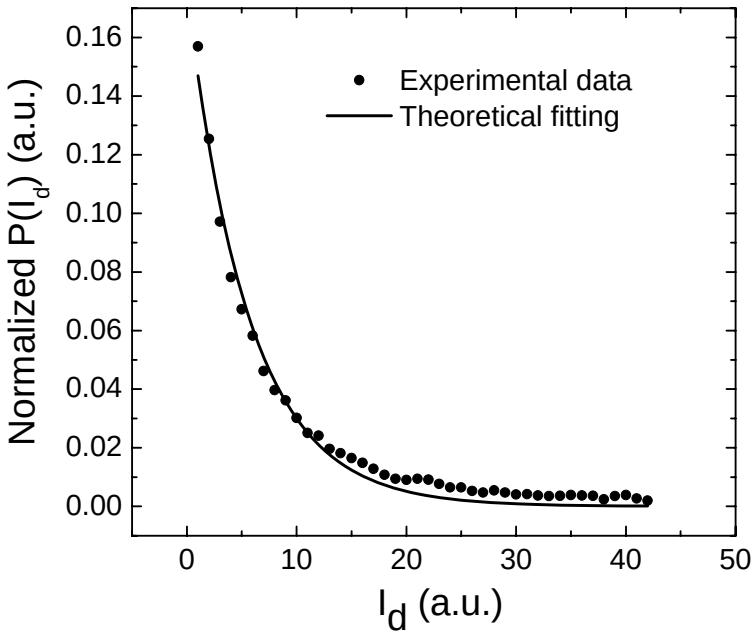

Figure 4.6 Experimental and calculated PDF of holographic speckle when the signal intensity is comparable to the reference and probe intensities.

4.6. Speckle Statistics under Large Signal Limit

4.6.1 Large signal limit

The second case is $I_S >> I_R$. In ophthalmologic applications such as coherence domain imaging of human eyes, the signal intensity may be high enough to omit the intensity of reference and probe in the interferometer. The reference intensity should be comparable to or lower than the signal intensity, which is reasonable in the holographic OCI based on

the PRQW due to the limitation of total intensity. Aside from the reference beam, the probe beam is also comparable to or lower than the signal intensity for the same reason. A more simplified form of I_d is deduced in the large signal limit where the diffraction intensity can be written as

$$I_d = f(I_S) = A\frac{I_P I_R}{I_S} \tag{4.23}$$

The diffraction intensity is inversely proportional to the signal intensity, which means that the inversion of the holographic image in this condition. Similar inversion phenomenon has been observed in other photorefractive materials, for example $Bi_{12}GeO_{20}$ [24].

Once again, the conversions of the variable and the statistics of the variable are given by

$$I_S = A\frac{I_P I_R}{I_d} \tag{4.24}$$

$$\frac{df(I_S)}{dI_S} = A\frac{I_P I_R}{I_S^2} \tag{4.25}$$

By using the conversion of the variable, the PDF of holographic speckle can be written as

$$P(I_d) = \frac{AI_P I_R}{\sigma_I I_d^2}\exp(-\frac{AI_P I_R}{\sigma_I I_d}) \tag{4.26}$$

Different from those cases discussed above, the PDF under a large signal condition is not a simple exponential decay, as shown in figure 4.7. The intensity distribution has a maximum at low intensity and the profile of this distribution spreads and broadens to the

high intensity region when the product of the reference and probe beam intensities increase. At the same time, the peak population decreases.

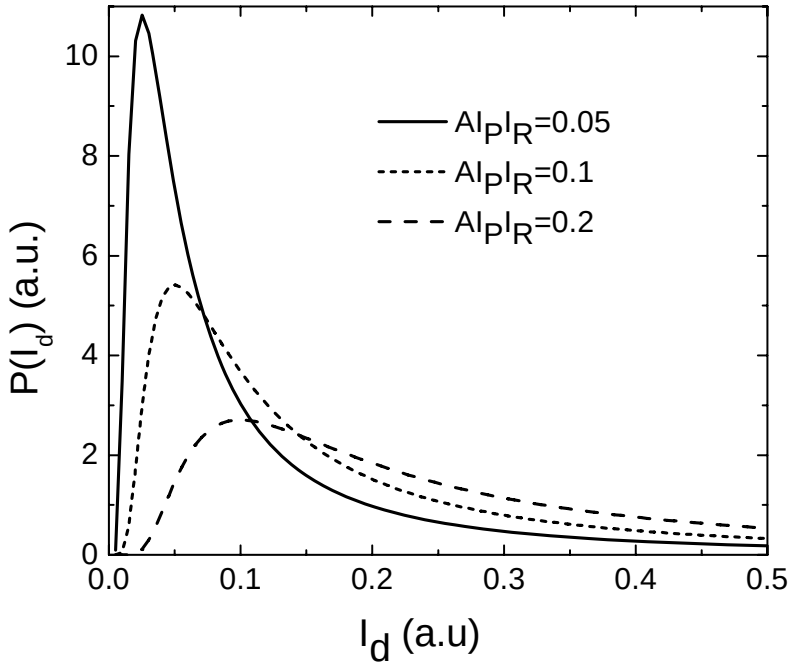

Figure 4.7 PDF simulation in the large signal limit.

The holographic speckle image with intensity ratio of $I_S=5I_R=5I_P$ is collected by the OCI system. Figure 4.8 shows a comparison between the experimental PDF and theoretically prediction by equation (4.26). In the large signal limit, the intensity histogram has a maximum in the low intensity region and the profile of this distribution broadens and spreads to high intensity area when the product of the reference and probe beam intensities increase. The fitting parameters include the diffraction efficiency,

intensity ratio between the signal and reference beams, and the standard deviation of intensity in the signal speckle. The difference between experiment and theory is due to the incoherent background from the sample (for example, the back reflection from the diffuser) that contributes a uniform intensity to the modulation. In the small signal limit, this contribution is neglected in the modulation.

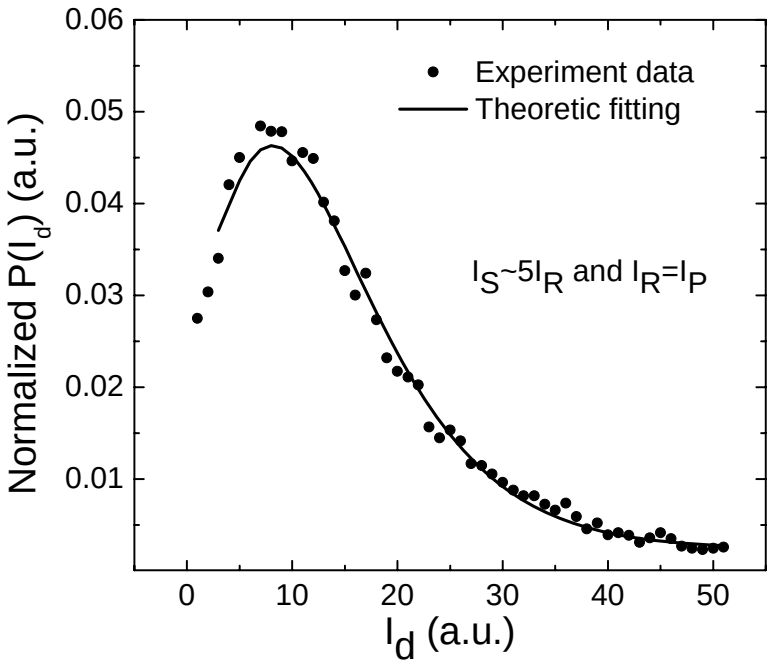

Figure 4.8 Experimental and calculated PDF of I_d in the large signal limit.

4.6.2 Joule heating limit for large signal limit

The constant phasor of the reference is smaller compared with the random phasor of the signal. This effect does not mean the constant phasor will not contribute the speckle statistics. Actually, as indicated in equation (4.27), this results in less impact from the reference intensity on the diffraction intensity.

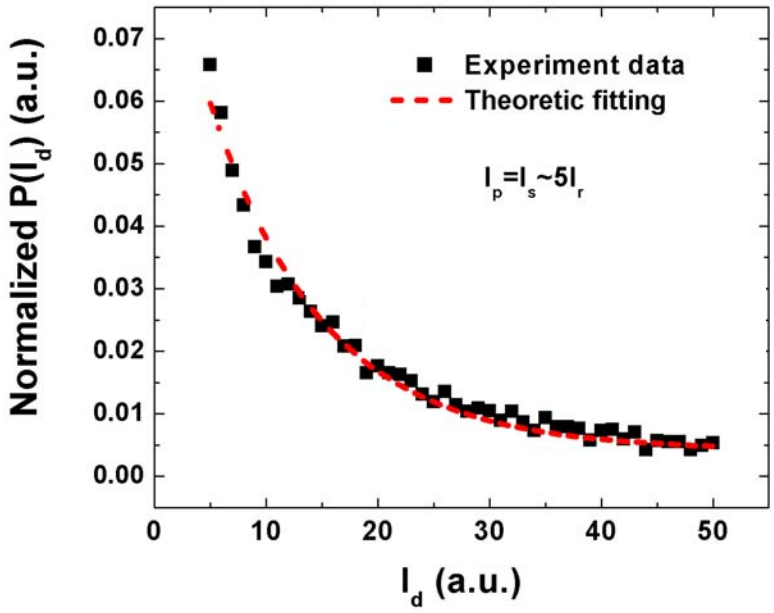

Figure 4.9 Experimental PDF of holographic speckle with maximum diffraction intensity and theoretical fitting in the large signal limit.

Similar to the small signal limit and the Joule heating limit cases, the total intensity irradiated on the device should be a constant for safety. The reference beam is comparatively much weaker, so the total intensity can be considered as the sum of signal and probe beam intensity. The diffraction intensity should reach the peak value when the

probe and signal beam intensities are equal to each other. Then, the speckle statistics in the hologram can be written as

$$P(I_d) = \frac{2C}{A\sigma_I I_R} \exp(-\frac{2CI_d}{A\sigma_I I_R}) \tag{4.27}$$

where $C/2=I_P=I_S >> I_R$. The distribution under this situation is also a negative exponential decay function, shown in figure 4.9. The holographic speckle image is measured with a weak reference beam. The intensity ratios between beams are $I_P = I_S \sim 5I_R$. The experiment data is fitted by an exponential decay function. Also, the two parameters in equation (4.27) are the same. The fitting equation gives two fitting coefficients with closed values too.

4.7 Discussions and Summary

We have simulated and experimentally studied the holographic speckle statistics in various conditions with good consistency between simulation and experiment results. Starting with fully developed speckle whose PDF is a negative exponential function, the PDFs take different forms as the changes of the relative intensity ratio between the signal and the intensities of reference and probe.

In coherence domain imaging, the coherent signal comes from the path-matched single or multiple scattering waves inside the sample. All other back-scattering components in the sample beam serve as an incoherent background that is rejected by

coherence detection. One question that arises from the holographic speckle is how the speckle statistics are altered by the incoherent background. Equation (4.3) tells us that the incoherent background changes the modulation index. In the small signal limit, which is the most common case of coherence domain imaging on highly scattering tissues, the PDF is always a negative exponential function. The incoherent background only modifies the slope of the PDF. When the system is in the Joule heating limit, the PDF has a constant slope on a semi-log plot and does not change with the total intensity. If the signal intensity is comparable or larger than the reference and probe intensities, the statistics of holographic speckle will be modified by the change of incoherence background. We have observed a phenomenon of modified the speckle statistics when there is an additional incoherent background in the experiment, such as environmental light.

In holographic speckle from multiple scattering we have used a turbid medium to simulate real biological tissue. In this case the speckle itself changes continuously due to Brownian motion, as it was observed in the direct image. However, for the PRQW device, the speed of image acquisition and reconstruction is fast enough in comparison with the speed of speckle movement. Therefore, the moving speckle is frozen in the PRQW during hologram acquisition. However, the CCD camera used for reconstruction of the hologram has a limited integration time. In experiments, we have observed a variable slope (as it is plotted in a semi-logarithm scale) by changing the integration time of the

CCD camera. This phenomenon cannot be observed in a static speckle, which gives evidence of dynamic speckle of multiple scattering due to the Brownian motion in the turbid medium. Although we can use the same theoretical results to analyze the static speckle as well as the speckle from multiple scatterings, they are quite different in size range and time dependence. This conclusion is of interest since the single scattering and multiple scattering that suffer different Brownian motions can be separated in the holographic OCI.

4.8 Conclusions

In conclusion, we have developed a theory to describe the speckle statistics in a holographic optical coherence imaging based on a photorefractive quantum wells. For fully developed speckle the speckle statistics are modified by the holographic process in a low coherence interferometry. The simulation of holographic statistics is confirmed by experiments. The probability density function of speckle has been discussed in the small and large signal limits, as well as the Joule heating limit. While the probability density function is a negative exponential function in the small signal limit, its form changes as a function of intensity ratio between the signal beam and the intensities of reference and probe beams. We have also compared the speckle statistics from signal scattering and multiple scatterings, and confirmed that they have similar speckle statistics.

BIBLIOGRAPHY

1. J. Rogowska, and M. E. Brezinski, "Evaluation of the adaptive speckle suppression filter for coronary optical coherence tomography imaging," Ieee Transactions on Medical Imaging **19**, 1261-1266 (2000).

2. J. M. Schmitt, S. H. Xiang, and K. M. Yung, "Speckle in optical coherence tomography," Journal of Biomedical Optics **4**, 95-105 (1999).

3. D. P. Popescu, M. D. Hewko, and M. G. Sowa, "Speckle noise attenuation in optical coherence tomography by compounding images acquired at different positions of the sample," Optics Communications **269**, 247-251 (2007).

4. K. W. Gossage, C. M. Smith, E. M. Kanter, L. P. Hariri, A. L. Stone, J. J. Rodriguez, S. K. Williams, and J. K. Barton, "Texture analysis of speckle in optical coherence tomography images of tissue phantoms," Physics in Medicine and Biology **51**, 1563-1575 (2006).

5. T. R. Hillman, S. G. Adie, V. Seemann, J. J. Armstrong, S. L. Jacques, and D. D. Sampson, "Correlation of static speckle with sample properties in optical coherence tomography," Optics Letters **31**, 190-192 (2006).

6. B. Karamata, K. Hassler, M. Laubscher, and T. Lasser, "Speckle statistics in optical coherence tomography," Journal of the Optical Society of America a-Optics Image Science and Vision **22**, 593-596 (2005).

7. M. Bashkansky, and J. Reintjes, "Statistics and reduction of speckle in optical coherence tomography," Optics Letters **25**, 545-547 (2000).

8. P. Yu, L. Peng, M. Mustata, J. J. Turek, M. R. Melloch, and D. D. Nolte, "Time-dependent speckle in holographic optical coherence imaging and the health of tumor tissue," Optics Letters **29**, 68-70 (2004).

9. H. Lin, and P. Yu, "Speckle Mechanism in Holographic Optical Imaging," Opt. Express **25**, 16322-16327 (2007).

10. B. Karamata, M. Laubscher, M. Leutenegger, S. Bourquin, T. Lasser, and P. Lambelet, "Multiple scattering in optical coherence tomography. I. Investigation and modeling," J. Opt. Soc. Am. A **22**, 1369-1379 (2005).

11. J. W. Goodman, *Speckle phenomena in optics, theory and applications* (Ben Roberts

& Company, 2007).

12. D. Huang, E. A. Swanson, C. P. Lin, J. S. Schuman, W. G. Stinson, W. Chang, M. R. Hee, T. Flotte, K. Gregory, C. A. Puliafto, and J. G. Fujimoto, "Optical coherence tomography," Science **254**, 1178-1181 (1991).

13. J. G. Fujimoto, M. E. Brezinski, G. J. Tearney, S. A. Boppart, B. Bouma, M. R. Hee, J. F. Southern, and E. A. Swanson, "Optical biopsy and imaging using optical coherence tomography," Nature Medicine **1**, 970-972 (1995).

14. R. Jones, N. P. Barry, S. C. W. Hyde, P. M. W. French, K. M. Kwolek, D. D. Nolte, and M. R. Melloch, "Direct-to-video holographic readout in quantum wells for 3-D imaging through turbid media," Opt. Lett. **23**, 103-105 (1998).

15. Y. Gu, Z. Ansari, M. Tzirak, R. Jones, P. M. W. French, D. D. Nolte, and M. R. Melloch, "Elimination of beam walk-off in low-coherence off-axis photorefractive holography," Opt. Lett. **26**, 334-336 (2001).

16. C. Dunsby, Z. A. Y. Gu, P. M. W. French, L. Peng, P. Yu, M. R. Melloch, and D. D. Nolte, "High-speed depth-sectioned wide-field imaging using low-coherence photorefractive holographic microscopy," Opt. Commun. **219**, 87-99 (2003).

17. P. Yu, M. Mustata, J. J. Turek, P. M. W. French, M. R. Melloch, and D. D. Nolte, "Holographic optical coherence imaging of tumor spheroids," Appl. Phys. Lett. **83**, 575-577 (2003).

18. P. Yu, L. Peng, M. Mustata, J. J. Turek, M. R. Melloch, and D. D. Nolte, "Time-dependent speckle in holographic optical coherence imaging and the state of health of tumor tissue," Opt. Lett. **29**, 68-70 (2004).

19. S. C. W. Hyde, R. Jones, N. P. Barry, J. C. Dainty, P. M. W. French, K. M. Kwolek, D. D. Nolte, and M. R. Melloch, "Depth-resolved holography through turbid media using photorefraction," IEEE J. Sel. Top. Quant. Electron. **2**, 965 (1996).

20. B. Kippelen, S. R. Marder, E. Hendrickx, J. L. Maldonado, G. Guillement, B. L. Volodin, D. D. Steele, Y. Enami, Sandalphon, Y. J. Yao, J. F. Wang, H. Rockel, L. Erskine, and N. Peyghambarian, "Infrared photorefractive polymers and their applications for imaging," Science **279**, 54-57 (1998).

21. E. Mecher, F. Gallego-Go´mez, H. Tillmann, H. Horhold, J. Hummelen, and K. Meerholz, "Near-infrared sensitivity enhancement of photorefractive polymer composites by pre-illumination," Nature **418**, 959-964 (2002).

22. P. Dean, M. R. Dickinson, and D. P. West, "Full-field coherence-gated holographic imaging through scattering media using a photorefractive polymer composite device," Appl. Phys. Lett. **85**, 363-365 (2004).

23. H. J. Tiziani, and J. Klenk, "Vibration analysis by speckle techniques in real time," Appl. Opt. **20**, 1467-1470 (1981).

24. E. Ochoa, L. Hesselink, and J. W. Goodman, "Real-time intensity inversion using two-wave and four-wave mixing in photorefractive Bi12GeO20,," Appl. Opt. **24**, 1826-1832 (1985).

25. S. I. Stepanov, *Applications of Photorefractive Crystals* (1994).

26. J.W.Goodman, *Statistical Optics* (John Wiley & Sons, Nwe York, NY, 1985).

27. J.W.Goodman, *Speckle phenomena in optics: theory and applications* (Ben Roberts & Company, Englewood, Colorado, 2007).

28. Boris Karamata, Kai Hassler, Markus Laubscher, and T. Lasser, "Speckle statistics in optical coherence tomography," J. Opt. Soc. Am. A **22** (2005).

29. D. D. Nolte, "Semi-insulating semiconductor heterostructures: optoelectronic properties and applications," J. Appl. Phys. **85**, 6259-6289 (1999).

30. P. Yu, L. Peng, D. D. Nolte, and M. R. Melloch, "Ultrasound detection through turbid media," Opt. Lett. **28**, 819-821 (2003).

Chapter 5

Holographic Speckle Imaging

5.1 Introduction

Holographic OCI, as one of the coherent domain imaging modalities, suffers speckle problem. Reports showed that the image contrast in the holographic OCI comes from the laser speckle due to the heterogeneous inside the cells [1]. However, detail studies of the speckle imaging in turbid medium using holographic OCI system have not been performed. Some of important questions should be answered for understanding the speckle imaging, for example, the system resolution changes due to the turbid medium. Similar to other coherent domain imaging system, speckle reduction techniques are also very important for holographic OCI in order to achieve high-quality image. In this chapter, we report a detailed research on the speckle imaging through turbid media (milk solutions) using low coherent light source in a holographic OCI system [2]. A new technique called moving grating technique is demonstrated to successfully suppress the random speckle noise and improve the image contrast in OCI [3]. Furthermore, the speckle influence on OCI system resolution is studied. System depth resolution as a function of the mean free paths (MFP) of the turbid medium is presented.

5.2 Holographic Speckle Imaging using Superluminescence Diodes

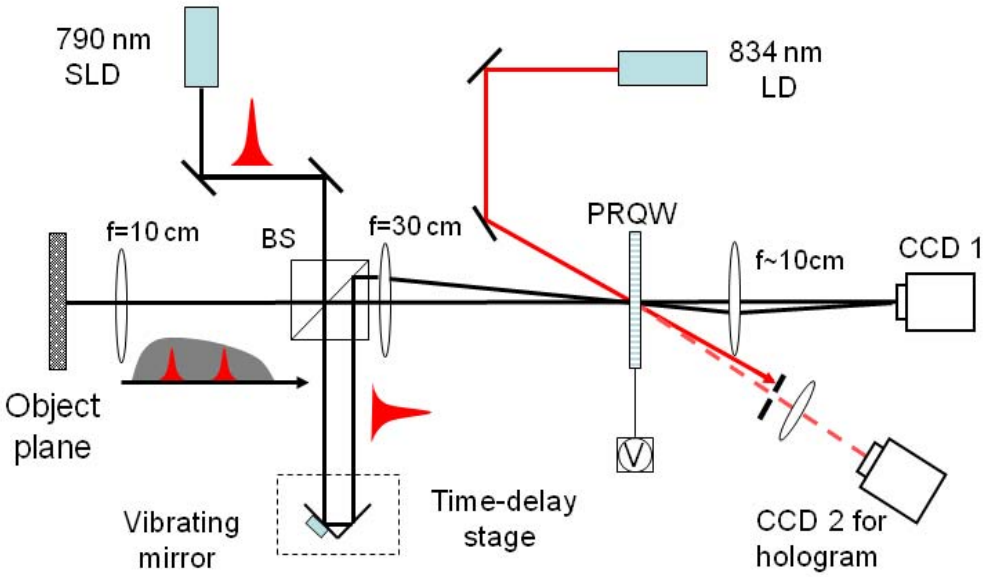

Figure 5.1 Low-coherence hologram OCI system with vibrating mirror.

To investigate the speckle imaging, we build an OCI imaging system that consists of a modified Michelson interferometer, a PRQW device, and two CCD cameras (SONY, SPT-M124) for direct image and holographic image, as demonstrated in figure 5.1. A 4-F lens system is used to relay the image from the object plane (the sample plane) to the image plane (the device plane). A nondegenerate four-wave mixing configuration has been used to write and probe (reconstruct) holograms. A 790 nm superluminescence light emission diode (QPhotonics, QSDM-790-9, 10 mW) with a wavelength bandwidth of about 40 nm serves as the writing beam. A cw laser diode (Hitachi DL5032) acts as the probe beam and its wavelength (834 nm) has been tuned to the exciton absorption peak

by the temperature controlling system.

The signal and the reference beams cross a small angle to generate fringes with a typical fringe spacing of about 20-30 μm inside the PRQW. The fringe spacing was adjusted to a proper value, which is comparable to the average speckle size, so that there are appropriate diffraction signal for image collection. A 10 kV/cm electric filed was applied across the PRQW device to induce the photorefractive effect. The fringe spacing and direct speckle image were monitored by the first CCD camera. An enlarge image was reconstructed onto the second CCD camera by imaging the first order diffraction signal from the non-degenerate four-wave mixing geometry.

A special feature of this system is a vibrating mirror in reference beam. This vibrating is used to generate moving grating in the PRQW. As we know, the two writing beams car combined and interfere to each other in the PRQW device and interference fringes generated in the device. When high voltage is applied across the device window and photorefractive effect is induced, this interference fringes works as a diffraction grating. If one of the mirrors in the reference arm is vibrating with a frequency, the interference fringes vibrate at the same frequency. As a result, the diffraction grating is moving at the same frequency. This technique is called moving grating technique. This technique is an effective way in OCI system to reduce the noise speckles.

5.2.1 Holographic speckle imaging generated by diffusers

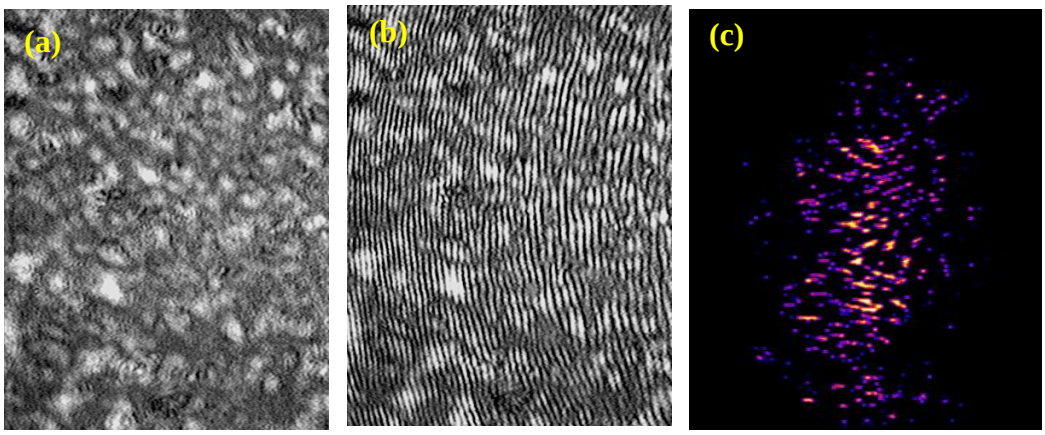

Figure 5.2 Speckle images (a) direct speckle image; (b) direct speckle image with the presence of reference beam; (c) holographic speckle image.

In order to generate well controlled speckles, diffusers are first used for speckle generation. A 10 degree diffuser is placed on the object plane and two CCD cameras are used to capture the direct images and holographic speckle images. As shown in figure 5.2(b), speckle pattern (a) is modulated by the interference fringes when the reference beam is presented. The bending of the fringes is due to the random phase in each single speckle. This bending of fringes changes the orientations of the holographic gratings in the PRQW device and makes the diffracted signal diverging, which in turn degrades the collective intensity of diffraction signals. Figure (c) presents the holographic speckle image after the background removal and intensity rescaling.

5.2.2 Holographic speckle imaging generated by turbid media

Milk solutions are used to simulate turbid media to produce speckles. A glass cuvette with 1 mm thickness is used to load the milk solutions. The solutions in cuvette with different mixing concentrations are placed on the object plane to generate speckle images. Three holograms corresponding to milk solutions with different mixing concentrations with water are collected and compared with the average intensities, intensity variations, intensity ranges and shaping constants.

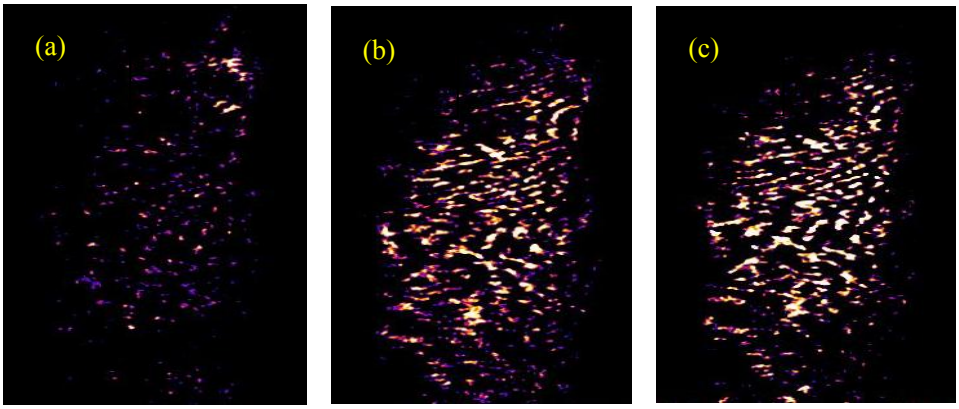

Figure 5.3 Holographic speckle images of milk-water solutions with different mixing ratios (milk: water) of (a) 1:16; (b) 1:32 and 1:64.

As shown in figure 5.3, all of those three holograms with background subtraction are optimized by the identical process of intensity rescaling. The mixing ratio for the first sample is 15:1(W:M). So the milk concentration is around 1/16. The second one is 0.5/16 and the third one is 0.25/16. Since the speckle image only appears in the PRQW window, an effective speckle area which is (311, 145, 88, 225) is cut and analysis by ImageJ. The

mean intensity values and the standard deviations of the intensity are calculated by plotting the histogram of the speckle image. Holograms of speckle imaging under different concentrations are studied for their shaping constants M, which can be calculated using the mean intensity ($\bar{I}$) and the intensity variance (σ) of the intensity by $M = (\bar{I})^2 / \sigma^2$.

The results are listed in table 5.1. The results indicate that the lower the concentration of the turbid media, the higher the average intensity of the holographic image. This is mainly due to the intensity variation and speckle size change caused by multiple scattering with different mixing concentration. Since the signal beam intensity is attenuating in the process of scattering, more multiple scattering occurring in dense solution yields less output intensity for transmitted beam. This explains that the intensity ranges are extended with the decrease of the concentration.

Table 5.1 Intensity statistics of holographic speckle images of milk solutions.

Image	C (M/W)	Mean	Std_Dev	Range	M value
a	1/16	4.377	6.305	0-43	0.48
b	1/32	7.943	10.413	0-60	0.58
c	1/64	8.854	11.51	0-82	0.59

As we mentioned in chapter 2, the main beam is split by 50% beam splitter into signal beam and reference beam. Both beams are combined in PRQW to generate interference. Since the reference beam is a simple reflection from mirror to the quantum device, it is generally stronger than signal beam. Although the high diffraction intensity is maintained

in a limited range when reference beam is stronger than signal beam [4], it is still necessary for the intensity balance between two writing beams to ensure the high contrast of the interference fringes, which work as a diffraction grating in PRQW. The strong attenuation on the signal beam causes intensity misbalance between writing beams, which in turn drop the diffraction intensity by degrading the quality of the diffraction grating.

Furthermore, the average size of the speckle generated by turbid solution depends on the concentration of the solution [2]. Our experimental results show that the higher concentration (low mean free path) of solution will produce smaller speckles. Detailed discussion about this result will be presented in the later sections. According to our discussion in chapter 2, those speckles with their sizes small than fringe spacing will not contribute to the hologram since those speckles can not be effectively modulated by the interference fringes. So the average speckle size and fringe spacing are important factors for diffraction efficiency [5]. As for a specific fringe spacing, speckle sizes decrease causes the decrement of the diffraction intensity. This could be another reason why the mean intensity drops with the increase of the concentration of the solution.

It is also interesting to notice that the shaping constant is increasing with the dropping of the concentration of the mixing solutions. As we already know, shaping constant represents the degree of freedom of the polarization [6, 7]. Although the incident beam is linearly polarized, the polarization of the transmitted beam through turbid media has been

destroyed due to multiple scattering and the polarization is random for the direct speckle images. Since the random polarization can always be treated as the addition of two independent polarizations, the shaping constant for the direct speckle image should be 2. When the signal beam interfere with the reference beam in the holographic medium, only those signals with their polarization parallel with the reference beam survive and contribute to the hologram. There is only one polarization devote to the holographic speckle image. Therefore the shaping constant for the holographic speckle image should be 1. And our experimental data indicate that the shaping constant for holographic speckle image is less than 1.

In practice, degree of the polarization is influenced by degree of the multiple scattering. Experimental results has indicated that degree of polarization decreases with the increase of the thickness of the turbid medium [8, 9] due to increase of the scattering. The increase in the concentration is another way to increase the chance of scattering or in another word, decrease the mean free path (MFP). Then the degree of polarization decrease with the decrease of MFP. Furthermore, from the formula definition of shaping constant, the lower intensity range for high concentration solution leading to small deviation of the intensity is another possible reason for low shaping constant for dense solution.

5.3 Speckle Reduction by Moving Grating Technique

Coherent domain image systems benefit themselves by employing the advantages of coherent properties of the radiation. But they have to suffer the speckle noise at the same time. Although speckle effect cannot be avoid in coherent domain image systems, it can be suppressed or reduced by many different techniques. A lot of research interests have been applied to decrease the speckle effect in OCT systems in recent years [10-14]. Although some of those techniques are successful for speckle reduction in OCT, they may not be transplanted to OCI system due to systems' differences. In this section, we proposed an effective way to suppress the speckle noise in OCI and simulation analysis is presented to understand this speckle reduction process.

Figure 5.4 demonstrates a technique to use moving grating to increase the imaging contrast in the speckle imaging. A reflection mirror in the one arm in the interferometer (usually reference arm) was vibrated in a frequency higher than the recording rate of the second CCD camera. This frequency is still much lower than the value that the PRQW can track. Therefore the reconstructed holograms can follow the vibration while the incoherence background is averaged in the CCD camera. This technique can effectively reduce the unwanted speckles and keep the coherence speckles which contain the structure information of the sample.

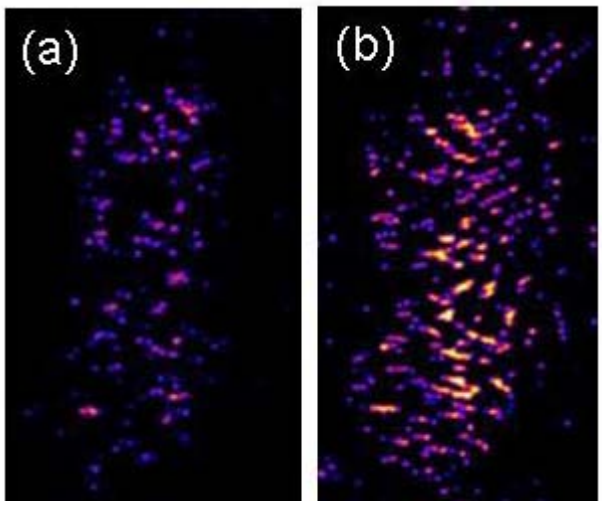

Figure 5.4 Hologram of speckle patterns generated by milk solution with (a) and without (b) vibrating mirror.

Table 5.2 Intensity statistics of speckle holograms with and without moving grating.

Type	Mean	StdDev	Range	M value
Vibrating	4.038	4.61	0-26	0.769
No Vibrating	4.703	6.29	0-37	0.559

Since the speckle image only appears in the PRQW window, an effective speckle area which is (299, 156, 87,216) is cut from a 640×480 image and analysis by ImageJ. The mean intensity value and the standard deviation of the intensity are calculated by studying the histogram of the speckle image. The results are listed in the table 5-2. The mean intensity of the speckle image decrease 14% and standard deviation of the intensity decrease 27% when moving grating is applied. Also the maxima intensity is decrease with moving grating technique. Moreover, the results indicate that the shaping constant

with moving grating effect 38% higher than the one without moving grating effect. The possible reason could be the intensity average on the CCD camera caused by the moving grating, which decrease the intensity range of the image and consequently, decrease intensity variation.

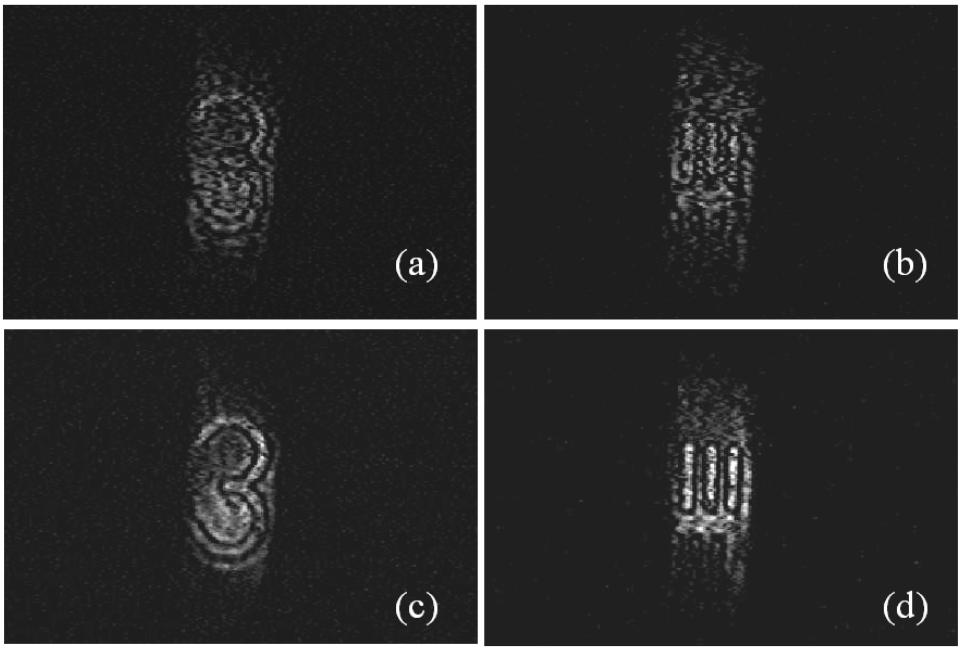

Figure 5.5 Comparison of holographic images of USAF test chart without (a) , (b) and with (c) , (d) moving grating technique using He-Ne laser. Number 3 is from group 4 with size of 250 μm×400μm; vertical bar is from group5 element 1 with size of 31 μm×155μm.

From previous chapter we can see that the FWM efficiency has the highest value when the speckle size is a little bigger than the fringe spacing. The holographic speckle should have the highest contrast at this size range. Since the fringe spacing is roughly equal to the resolution of the holographic imaging system, the presence of the

holographic speckle can strongly degrade the image quality, as demonstrated in figure 5.5(a) and (b). Those holograms are generated using He-Ne laser which has good coherence property. A fringe spacing of 17 micron is used. A moving grating technique is applied to solve noise speckle problem. The number 3 is from group 4 element 3. The width and height of this number are around 250 microns and 400 microns. The vertical bars are from group 5 element 1, which have around 31-micron thickness and 155-micron height.

A mirror in the reference arm of the interferometer is vibrated at a frequency of 800 Hz by using a piezoelectric stack. This results the same-frequency vibration of fringes (grating when high voltage applied) inside the PRQW. The PRQW has a fast response time (about 100 KHz at an intensity of 100 mW/cm^2) so that it can track the moving of the grating. The frequency of the vibration is sufficiently high to allow the CCD camera to take a time average over many cycles. The difference in response times between the holographic record medium and CCD camera allows the system to average the speckle noise while retaining the full spatial coherence and intensity variation arising from the structures in the sample. The phenomenon is similar to the speckle suppression technique of moving screen in projection displays [6].

As shown in figure 5.5(c) and (d), the function of the moving grating technique for reducing the noise speckle is apparent by comparing the holograms of number three and

bars in the group four of a USAF test chart with and without vibration. The strong background is mainly due to the good coherence and long coherence length of the light source. But improvements on the contrast for both images with moving grating technique are apparent. Although the background looks brighter with speckle reduction technique, the increase in background uniformity sharpens the structure of the objects, as shown in figure (c) and (d). This is an exaggerated case of speckle effect by use He-Ne laser as writing beams since in practice low coherent light source is used for hologram writing and speckle phenomenon is not as serious as this case presented.

Figure 5.6 presents the holograms of number 3 and bars in the test chart under low-coherence broadband superluminescence diode. A fringe spacing of 12 μm is used for hologram writing. Compared with figure 5.5 (the same objects, but different light source), the background intensity in figure 5.6 is much less. But the structure information of the objects especially for the boundaries of the objects is still affected by the speckles, as shown in 6(a), (b) and (c). The influence of the speckles is reflected in the discontinuity of the boundaries and holes in the structure areas. Also the speckles make the background very noisy and speckled. Moving grating technique solved most of those problems, as indicated in figure (d), (e) and (f). The background becomes uniform. The sharpness and contrasts of the object structure and boundary in the images are improved. So the moving grating technique makes the OCI system possible for imaging into tumor and tissue.

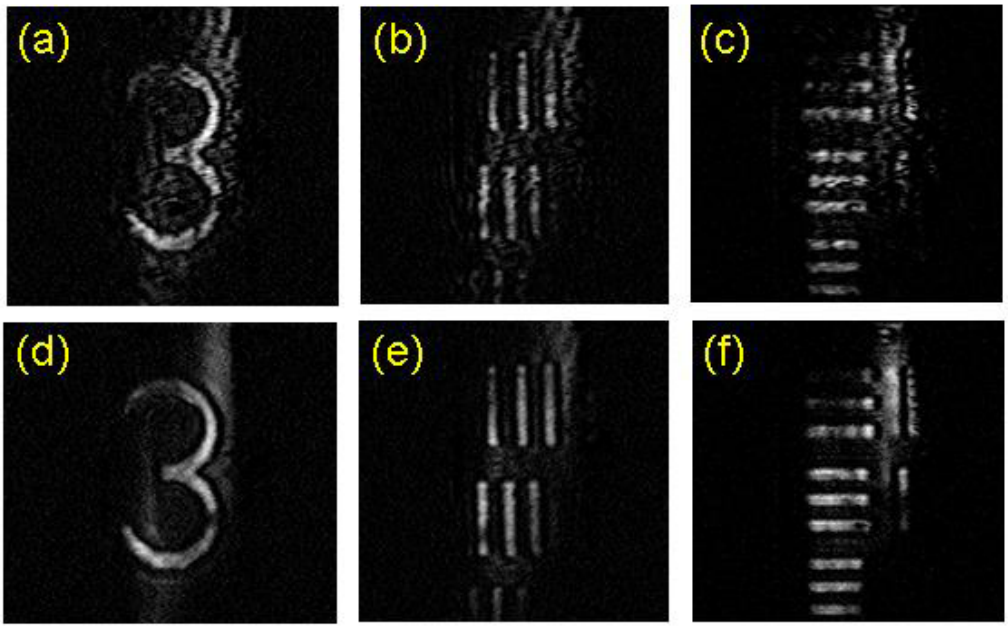

Figure 5.6 Comparison of holographic images of USAF test chart without (a), (b), (c) and with (d), (e), (f) moving grating technique using broadband superluminescent diode. Number 3 is from group 4 with size of 250 μm×400μm; vertical bars are from group 5 elements 1 and 2 with size of 31 μm×155μm and 28 μm×140μm; horizontal bars are from group 5 elements 2,3 and 4 with size of 28 μm×140μm, 25 μm×125μm and 22 μm×110μm .

So far we proved that the moving grating technique can be used for speckle reduction when flat and smooth object (test chart) is directly imaged. However, the situation for imaging into biological sample like tissue is much complicated. In order to dig the structure information under the surface, the light probe has to survive enough intensity from the complicated absorption and scattering process by going through the top layer of the sample. In order to simulate this process, a 1 mm-thick milk solution is placed immediate in front of the test chart to study the speckle reduction by moving grating. First the biggest square of the test chart is used as a mirror to check the

interference fringes, as shown in figure 5.7(a). A fringe spacing of around 12 micron is selected for this experiment. Then horizontal bars of group 5 element 5 (20μm) and 6 (18μm) are used as objects. A DC voltage of 1260 V is applied across the PRQW for hologram writing and reading out.

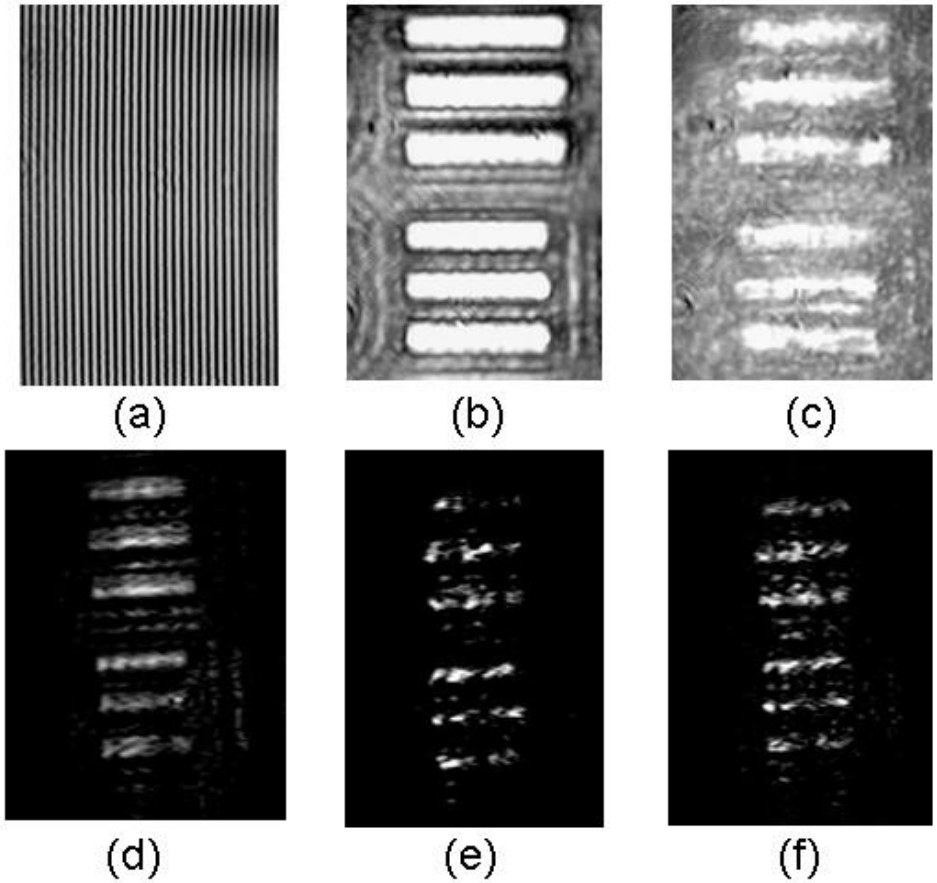

Figure 5.7 (a) interference fringes; (b) direct image of test chart; (c) direct image of test chart through milk; (d) holographic image of test chart; (e) holographic image of test chart through turbid medium without moving grating technique; (f) holographic image of test chart through turbid medium with moving grating technique; horizontal bars are from group 5 elements 5 and 6 with size of 20 μm×100μm and 18 μm×90μm.

As shown in figure 5.7(b) and (d), sharp direct image and clear hologram are captured without milk solutions, although the object size is small. However, the image of the test chart is blurred when turbid solution is placed on the way of the signal beam, as indicated in 5.7(c) and (e). The boundary of the direct image is not sharp and clear and the structures of the bars are distorted and discontinue due to the serious speckle noise, which almost kill the holographic image. When 800 Hz vibrating is applied to the system, the hologram becomes better, as shown in figure 5.7(f). Although it can not reject all the influence of the speckle, it improves the quality of the image.

In order to understand the speckle reduction mechanism of the moving grating technique, a simulation analysis is carried out. Diffuser is used to generate speckles and images of speckle pattern with and without moving grating technique are analyzed. Figure 5.8 presents a simulation analysis on the speckle intensities with and without vibration using a Matlab program (Appendix IV). The vibration frequency of the moving grating is 600 Hz. The integration time of the CCD camera is set to be 30 ms. Based on the simulation, it is apparent that the holographic speckle intensity with 600 Hz vibration decreases to about 1/5 of the holographic speckle intensity without moving grating.

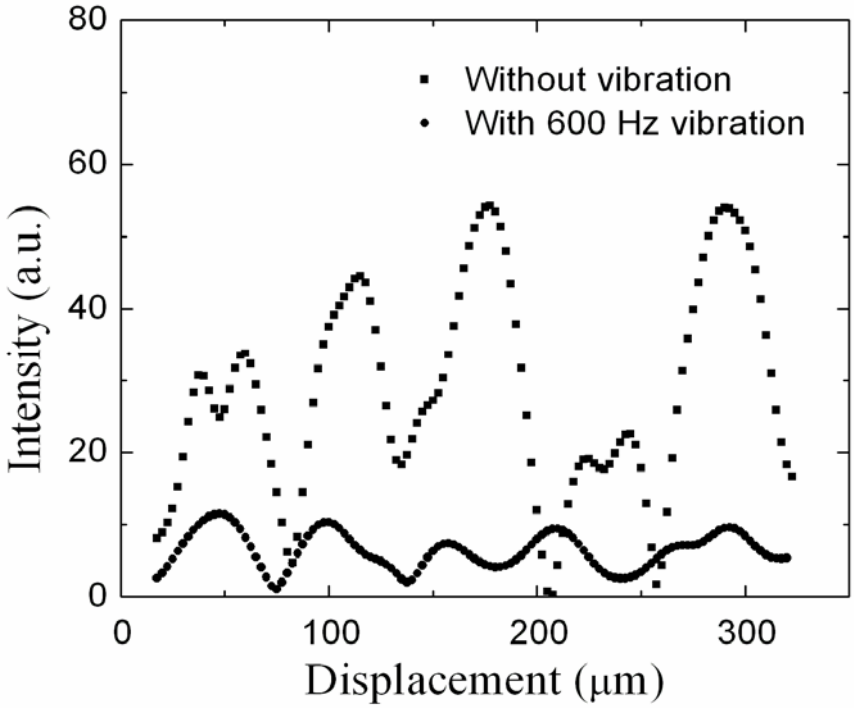

Figure 5.8 Simulation analyses of the speckle intensities with and without moving grating technique.

5.4 OCI System Resolution

In the case of OCI, because the diffraction intensity depends on the squared modulation function, supposing the reference arm is a reflectance delay stage, in which case the reference arm displacement is equivalent to the detecting depth in the sample, it can be shown that for a single reflection, the diffracted intensity as a function of z, the displacement of the reference arm relative to the reflecting surface, varies as

$$I_d(z) \propto erf\left\{(8\ln(2))^{1/2}\frac{[w/2 + x_0(2z/c)]}{\Delta x}\right\} + erf\left\{(8\ln(2))^{1/2}\frac{[w/2 - x_0(2z/c)]}{\Delta x}\right\} \qquad (5.1)$$

$$\Delta x = \frac{L}{\sin(\theta)} \quad \text{and} \quad x_0(z) = \frac{2z}{\sin(\theta)}$$

where c is the constant of light speed. w is the observation window width of the photo-refractive quantum well. θ is the cross angle between the signal arm and reference arm. L is the coherent length of the light source.

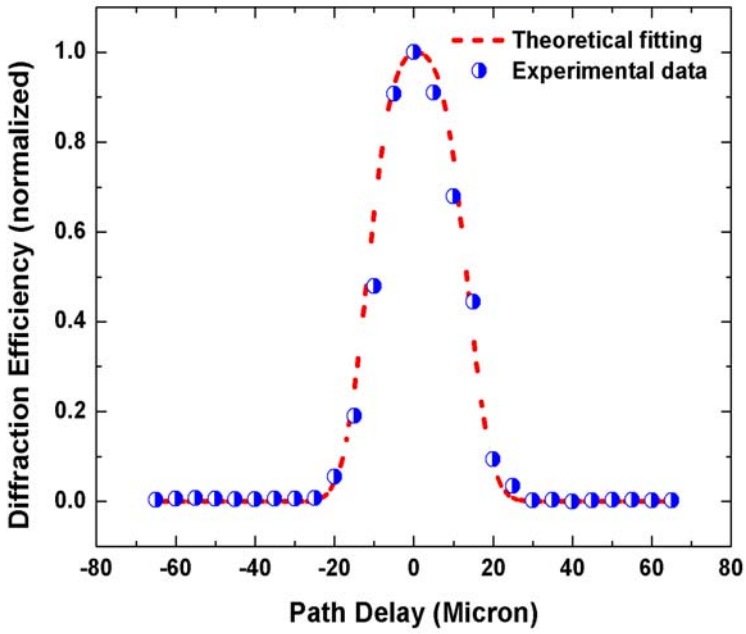

Figure 5.9 Depth resolution of the OCI imaging system using low-coherence broadband superluminescence diode.

In order to experimentally detect the system depth resolution, a mirror is placed on the object plane. Holograms of the mirror with several path-length differences are collected. The depth resolution of the system was calculated by measuring the average diffraction intensity from the holograms as a function of the reference delay. The result gives a good consistent with the theoretical calculation as shown in figure 5.9. A Matlab

program is used for this fitting process (Appendix V). The Full width at half maxima (FWHM) of this fitting profile gives the system depth resolution.

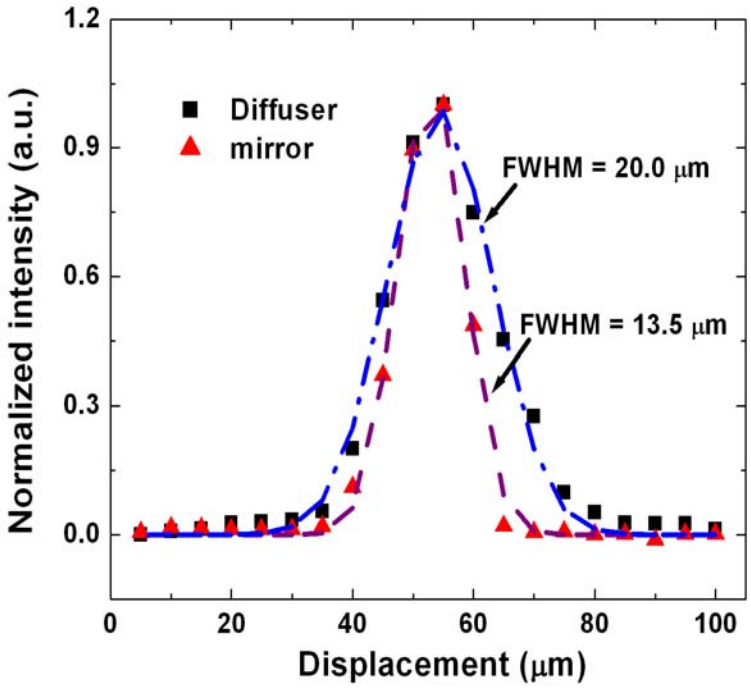

Figure 5.10 Comparison of the depth resolutions in OCI system with and without speckle influence. FWHM increases from 13.5 microns to 20 microns when speckle effect applied.

As we already known, the speckles degrade the image contrast and quality [5]. The depth resolution of the OCI system is degraded by speckle effect in the same process. As shown in figure 5.10, the system resolutions are measured separately by placing mirror and diffuser on the object plane. The intensity profile present an obvious broaden with the diffuser. The system resolution decreases 48% from 13.5 μm to 20 μm. This is mainly

due to the coherence wave-front distortion in the multiple scattering processes [15].

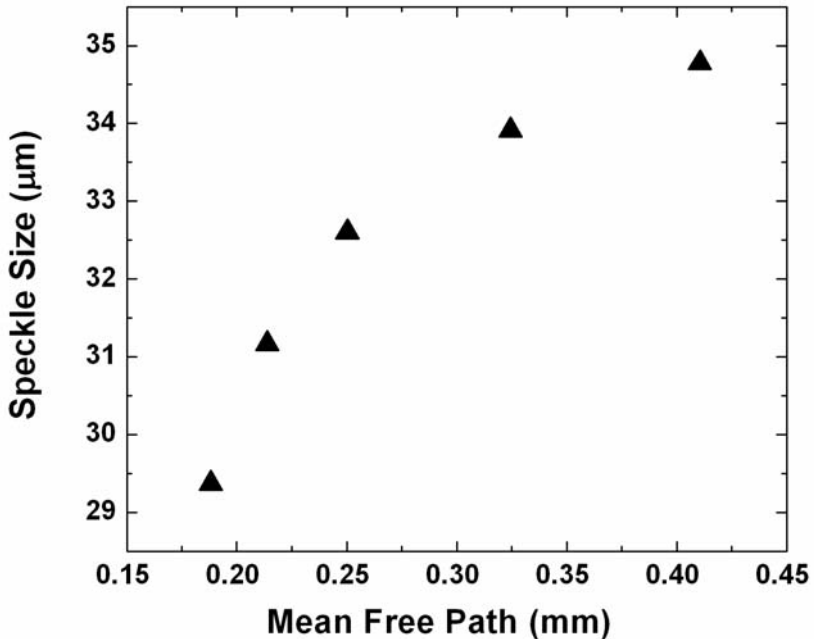

Figure 5.11 Relationship between mean free path of the turbid solution and average size of the speckles generated by the solution.

In order to study the influence of the milk solution concentration on the OCI system resolution, a 1.0 mm sample cell filled with turbid medium (milk and polystyrene beads) is located ~1mm away from the object plane of the image system where a USAF Test Chart is placed. The biggest square on the test chart is selected as imaging point to guarantee enough reflected intensity of the signal branch. To maintain a good contrast, the CCD camera has been set to an auto-exposure mode. Holographic speckle patterns generated by milk suspensions with different concentrations have been collected and their

average sizes are calculated after the data acquisition. As indicated in figure 5.11, the average holographic speckle sizes are increasing with the increase of MFP of the turbid media and the small speckles are generated by low MFP solution (corresponds to high concentration turbid media). Also the system resolutions under difference MFP are measured. The resolution drop fast when the concentration is very high.

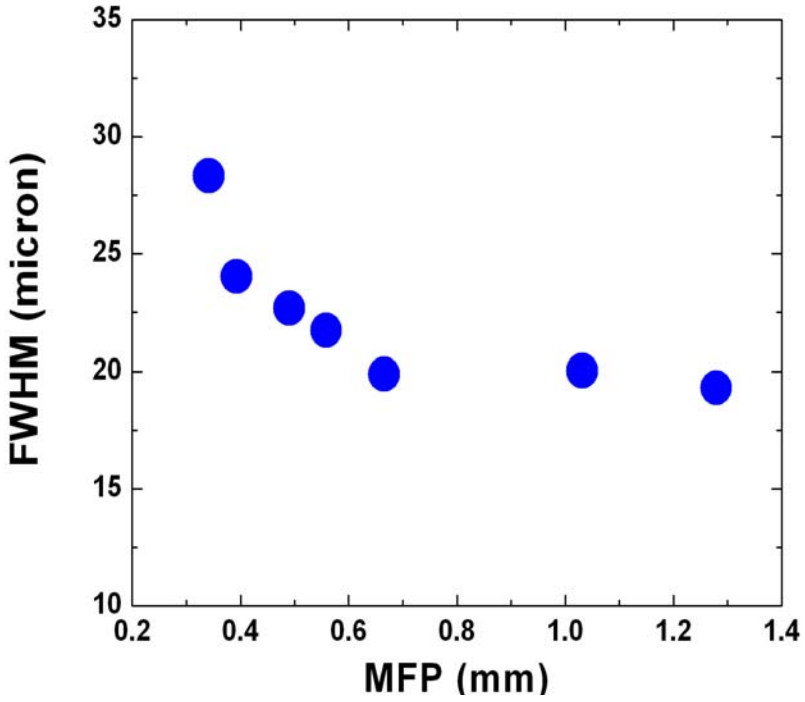

Figure 5.12 Relationship between system resolutions and mean free path of the turbid media. FWHM decreases with the increment of the MFP of the solutions.

Based on the Twersky theory [16] of multiple scattering, the MFP in turbid suspension can be estimated by the intensity ratio of non-scattered light and incident light, which is also linearly related to the concentration of the suspension. We calculate the MFP for the turbid medium in the holographic OCI system according to experimental

data. The depth resolution as a function of MFP is shown in figure 5.12. The depth resolution is improved as the MFP increases at a lower value region. The improvement could be due to the large angle scattering since the OCI system, unlike conventional OCT systems, collect large angle scattering.

5.5 Conclusion

In conclusion, we experimentally achieve speckle imaging through turbid media by using holographic optical imaging. Theoretical prediction of the speckle gamma probability density function shows a good consistency to the experimental results. As for the speckle effect in optical coherence imaging system, we presented an efficient method to suppress the speckle by using a moving grating technique. Furthermore, we found that the speckle sizes of the holographic patterns are related to the mean free path of the turbid media. The depth resolution of the speckle imaging is modified by the concentration of the turbid medium.

5.6 Future works

In this thesis, we systematically studied speckle mechanism in holographic optical coherence imaging. There are still some projects that can be developed based on this thesis.

This thesis already provides experiment to prove the concept of using two wave mixing signal for an imaging system. In order to improve the image acquisition speed, phase modulator can be used to change the polarization of the reference beam. Instead to acquire the images of with and without path match, the images for with and without polarization match between reference and signal beams can be collected. The advantages of using phase modulator to change the polarization of reference beam include high speed and constant intensity on quantum well device.

Multiple scattering of turbid media based on optical coherence imaging system is another topic that can be addressed. Speckle should be a significant issue for this study. The results should be very useful for later study of biological sample such as tissue or tumor. Furthermore, the well developed optical coherence imaging system should be used to image some samples including vegetables, tissue and plants. With moving grating technique, speckle noise should be reduced. High image quality and high contrast should be observed.

BIBLIOGRAPHY

1. P. Yu, L. Peng, M. Mustata, J. J. Turek, M. R. Melloch, and D. D. Nolte, "Time-dependent speckle in holographic optical coherence imaging and the state of health of tumor tissue," Opt. Lett. **29**, 68-70 (2004).

2. Lin Haibo, and Ping, Yu, "Speckle Mechanism in Optical Coherence Imaging," in *Conference on Lasers and Electro-Optics/Quantum Electronics and Laser Science Conference and Photonic Applications Systems Technologies*(Optical Society of America, 2007), p. JTuA42.

3. Lin Haibo, and Yu Ping, "Speckle Imaging Using Photorefractive Multiple Quantum Wells," in *Conference on Lasers and Electro-Optics/Quantum Electronics and Laser Science Conference and Photonic Applications Systems Technologies*(Optical Society of America, 2006), p. CTuW3.

4. D. D. Nolte, "Semi-insulating semiconductor heterostructures: Optoelectronic properties and applications," J. Appl. Phys. **1999**, 6259-6289 (1999).

5. Haibo Lin, and Ping Yu, "Speckle Mechanism in Holographic Optical Imaging," Opt. Express **15**, 16322-16327 (2007).

6. J.W.Goodman, *Speckle phenomena in optics: theory and applications* (Ben Roberts & Company, Englewood, Colorado, 2007).

7. J.W.Goodman, *Statistical Optics* (John Wiley & Sons, Nwe York, NY, 1985).

8. Z. Y. Wang, M. A. Webster, A. M. Weiner, and K. J. Webb, "Polarized temporal impulse response for scattering media from third-order frequency correlations of speckle intensity patterns," Journal of the Optical Society of America a-Optics Image Science and Vision **23**, 3045-3053 (2006).

9. J. Ellis, and A. Dogariu, "Discrimination of globally unpolarized fields through Stokes vector element correlations," Journal of the Optical Society of America a-Optics Image Science and Vision **22**, 491-496 (2005).

10. Bashkansky, and Reintjes M., J., "Statistics and reduction of speckle in optical coherence tomography," Optics Letters **25**, 545-547 (2000).

11. Desjardins, Vakoc A. E., Oh B. J., Motaghiannezam W. Y., Tearney S. M. R., and B.

E. Bouma, "Angle-resolved Optical Coherence Tomography with sequential angular selectivity for speckle reduction," Optics Express **15**, 6200-6209 (2007).

12. A. E. Desjardins, B. J. Vakoc, G. J. Tearney, and B. E. Bouma, "Speckle reduction in OCT using massively-parallel detection and frequency-domain ranging," Optics Express **14**, 4736-4745 (2006).

13. J. Kim, D. T. iller, E. Kim, S. Oh, J. Oh, and T. E. Milner, "Optical coherence tomography speckle reduction by a partially spatially coherent source," Journal of Biomedical Optics **10** (2005).

14. D. L. Marks, T. S. Ralston, and S. A. Boppart, "Speckle reduction by I-divergence regularization in optical coherence tomography," Journal of the Optical Society of America a-Optics Image Science and Vision **22**, 2366-2371 (2005).

15. M. J. Yadlowsky, and R. F. Bonner, "Multiple-Scattering in Optical Coherence Microscopy," Applied Optics **34**, 5699-5707 (1995).

16. A. Ishimaru, "Wave-Propagation and Scattering in Random-Media and Rough Surfaces," Proceedings of the Ieee **79**, 1359-1366 (1991).

APPENDIX

Appendix I. USAF 1951 Test Chart

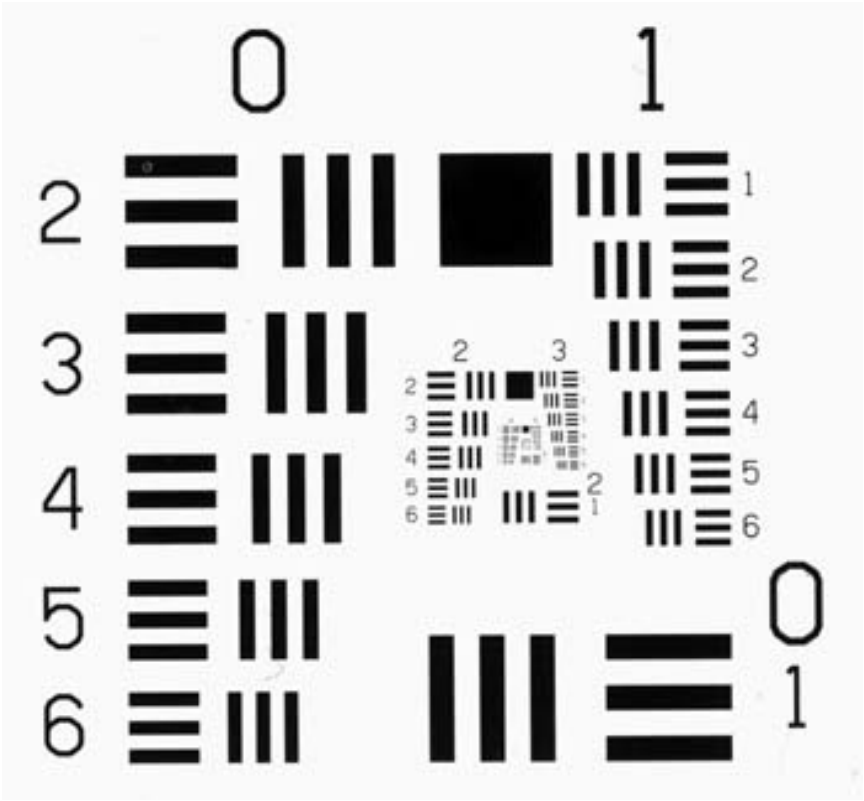

Object size in USAF 1951 Test Chart

Number of mm / Line in USAF Resolving Power Test Target 1951							
Group Number							
Element	**0**	**1**	**2**	**3**	**4**	**5**	**6**
1	1	0.5	0.25	0.125	0.0625	0.03125	0.01563
2	0.89286	0.44643	0.22272	0.11136	0.05571	0.02778	0.01393
3	0.79365	0.39683	0.19841	0.09901	0.0496	0.02481	0.01241
4	0.70922	0.35336	0.17668	0.0885	0.04421	0.02208	0.01105
5	0.62893	0.31546	0.15748	0.07874	0.03939	0.01969	0.0098
6	0.5618	0.2809	0.14025	0.06993	0.03509	0.01754	0.00877

Appendix II. Matlab program for speckle size calculation

```
M=400;                          % determine how many AC of arrays will be averaged
N=400;                          % determine how many AC of columns will be averaged
A=imread('1-speckle.tif');      % read file
B=A(:,158:558);                 %cut a strip of image
figure(1)
imshow(B);                      % show the striped image
B=double(B);                    % change data to double character
E=B(1,:);                       % select one array of data
s=size(xcov(E));                % get the size of AC serial
D=zeros(s);                     % generate a zero serial with the same size with AC serial
D=double(D);                    % set the serial with double character
for i=1:M                       % begin of the cycle; parameter is define at the begining
C=B(i,:);                       % choose one array
D=imadd(D,xcov(C,'coeff'));     % Do AC and add it to the zero serial
end;                            % End of the circle
figure(2)
G=D/M;                          % Normalized the addition
plot(G);                        % Plot the normalized AC
E1=B(:,1);                      % Same process to calculate normalized AC to column
s1=size(xcov(E1));
D1=zeros(s1);
D1=double(D1);
for j=1:N
C1=B(:,j);
D1=imadd(D1,xcov(C1,'coeff'));
end;
figure(3)
G1=D1/M;
plot(G1);
```

Appendix III. Matlab program for fitting the intensity threshold experimental data

```
Y=zeros(160,1);
X=zeros(160,1);
M=2.064;
L=1100;
i=1;
for x=1:0.01:2.6
      T=immultiply(M,x);
      double A;
      double B;
      double Y;
      A=(T.^(M-1))*((2*T)-(2*M)+1)*L;
      B=pi*(exp(T))*(gammainc(M,T));
      Y(i)=imdivide(B,A);
      X(i)=x;
      i=i+1;
end;
double X1;
double Y1;
X1=[1.01388,1.18286,1.37784,1.55982,1.7288,1.94977,2.20974,2.46971];              %
experimental data
Y1=[0.00583,0.00358,0.00238,0.00173,0.00142,0.00112,9.6125E-4,8.49375E-4];        %
experimental data
figure (1);
[AX,H1,H2]=plotyy(X,Y,X1,Y1,'plot');
set(get(AX(1),'Ylabel'),'String','Theoretic fitting');
set(get(AX(2),'Ylabel'),'String','Experimental data');
xlabel('I_t/I_a');
title('Average speckle area (mm^2) VS Ithreshold/Iaverage');
set(H1,'LineStyle','--');
set(H2,'LineStyle','o');
clear all;
```

Appendix IV. Matlab program to calculate speckle intensity with and without moving grating technique

```
L=95;      % begin # of pixel of first order of FFT
M=131;     % end # of pixel of first order of FFT
N=M-L;
K=114;
P=1;
filter=zeros(1,M-L+1);
filter(1:(M-L)/2+1)=0:(2/(M-L+1)):1;
filter=fliplr(filter);
filter(1:(M-L)/2+1)=0:(2/(M-L+1)):1;
A=imread('sf.tif');    % read file
B=A(180:380,180:480); % cut file
figure(7)
imshow(B);           % show image
s=size(fft(B(K,:)));
S=zeros(s);
for i= K:K+P
      T=B(i,:);
      C=fft(T);
      X=abs(fftshift(C));              % do fft and get absolute value
      S=imadd(S,X);
end;
figure(1)
plot(S);
E=S;
E(:)=0;
E(L:M)=S(L:M).*filter;
H=zeros(N);
for k=L-1:M-1
      l=k-93;
      H((l))=E(k);
end;
figure(2)
plot(H);
F=ifft(H);
figure(3)
plot(abs(F));
xlabel('Pixel Number','FontSize',12)
```

```
ylabel('Speckle Intensity','FontSize',12)
title('Intensity distribution of speckle without vibration grating','FontSize',14)
L1=L;
M1=M;
K1=10;
filter1=zeros(1,M1-L1+1);
filter1(1:(M1-L1)/2+1)=0:(2/(M1-L1+1)):1;
filter1=fliplr(filter1);
filter1(1:(M1-L1)/2+1)=0:(2/(M1-L1+1)):1;
A1=imread('600.tif');    % read file
B1=A1(180:380,180:480);
figure(8)
imshow(B1);
s1=size(fft(B1(K1,:)));
S1=zeros(s1);
for j= K1:K1+P
      T1=B1(i,:);
      C1=fft(T1);
      X1=abs(fftshift(C1));
      S1=imadd(S1,X1);
end;
figure(4)
plot(S1);
E1=S1;
E1(:)=0;
E1(L1:M1)=S1(L1:M1).*filter1;
H1=zeros(N1);
for k=L:M
      l=k-94;
      H1((l))=E1(k);
end;
figure(5)
plot(H1);
F1=ifft(H1);
figure(6)
plot(abs(F1));
xlabel('Pixel Number','FontSize',12)
ylabel('Speckle Intensity','FontSize',12)
title('Intensity distribution of speckle without 600 Hz vibration grating','FontSize',14)
```

Appendix V. Matlab program for fitting the experimental system resolution profile

```
G=[0.9,0.97,1.02,0.98,0.93,0.92,0.99,0.98,1.02,2.78,7.84,18.57,34.52,37.94,34.61,26.02,
17.29,4.24,2.03,0.85,0.87,0.76,0.84,0.88,0.89,0.83,0.82,];
H=-65:5:65;
J=min(G);
G1=G-J;
T=max(G1);
G2=G1/T;

A=-65:1:65;
B=zeros(131);
x=48; % x=wsin(a), where w is the effective window of PRQW
y=64; % y=2L, where L is the coherence length of the light source
t1=2.35457;
m=4;
for i=1:131
      B(i)=erf(t1*(m*(i-66.8)+x)/y)+erf(t1*(-m*(i-66.8)+x)/y);
end;
T=max(B);
B1=B/T;
figure(1)
plot(A,B1);
figure(2)
[AX,H1,H2]=plotyy(A,B1,H,G2,'plot');
set(get(AX(1),'Ylabel'),'String','Theoretic fitting');
set(get(AX(2),'Ylabel'),'String','Experimental data');
xlabel('Displacement (Micron)');
title('Average speckle area (mm^2) VS Ithreshold/Iaverage');
set(H1,'LineStyle','--');
set(H2,'LineStyle','o');
clear all;
```

VITA

Haibo Lin was born in Xinjiang, China on August 3rd, 1977, to Zhimin Lin and Aimei He. He spent his carefree childhood years in Xinjiang, China. While attending Third High School of Akesu (Akesu, Xinjiang, China) he developed an avid interest in the sciences. He then joined Xinjiang University, Urumqi, Xinjiang, China, where he pursued his Bachelor of Science degree in Applied Physics. He then moved to pursue his Masters of Science degree in Condensed Matter Physics at Nankai University, Tianjin, China. He then joined Prof. Ping Yu's group in University of Missouri-Columbia, Columbia, Missouri in August 2004. Since then his research career has led to several technical and conference publications.